Interaction between the Andes and the Climate System, and Wave Studies

A Dissertation

submitted to the Department of Earth, Environmental and Planetary Science

at Brown University

in partial fulfillment of the requirements

for the Degree of Doctor of Philosophy

by

Weixuan Xu

PROVIDENCE, RHODE ISLAND

February 2023

This dissertation by Weixuan Xu is accepted in its present form
by the Department of Earth, Environmental and Planetary Sciences as satisfying the
dissertation requirement for the degree of Doctor of Philosophy.

*Date*_____ _____

Jung-Eun Lee, Brown University, Advisor

*Date*_____ _____

Baylor Fox-Kemper, Brown University, Co-Advisor

Recommended to the Graduate Council

*Date*_____ _____

Brad Marston, Brown University, Reader

*Date*_____ _____

Victor Tsai, Brown University, Reader

*Date*_____ _____

Michael J. McPhaden, NOAA/PMEL, Reader

Approved by the Graduate Council

*Date*_____ _____

Thomas A. Lewis, Dean of the Graduate School

Weixuan (Rosa) Xu

Ph.D. Candidate in Earth, Environmental, and Planetary Sciences
weixuan_xu@brown.edu

Office: MacMillan Room 105
Thayer and George Streets.
Providence, RI
02912

tel: 401.651.3388

Mailing: Dept. of Earth, Environmental,
and Planetary (DEEP) Sciences
324 Brook Street, Providence, RI

EDUCATION

2018-	**Brown University** Ph.D. Earth, Environmental and Planetary Sciences Advisors: Jung-Eun Lee and Baylor Fox-Kemper
2014-2018	**Peking University** B.S. Physics Advisor: Yongyun Hu
2016	**Rice University** Exchange Program

RESEARCH EXPERIENCE

2018-	**Graduate Research Fellow** Department of Earth, Environmental, and Planetary Sciences, Brown University Advisors: Jung-Eun Lee and Baylor Fox-Kemper
2016-2018	**Undergraduate Research Assistant** Department of Atmospheric and Oceanic Sciences, School of Physics Advisor: Yongyun Hu

PUBLICATIONS

- Xu, W., Lee, J., Fox-Kemper, B., Planton, Y., & McPhaden, M. J. (2022). The Andes Affect ENSO Statistics, *Journal of Climate*, *35*(21), 3477-3491. Retrieved Nov 15, 2022, from https://journals.ametsoc.org/view/journals/clim/35/21/JCLI-D-21-0866.1.xml

- Weixuan Xu and Jung-Eun Lee. The Andes and the southeast pacific cold tongue simulation. Journal of Climate, pages 1 – 41, 04 Nov. 2020. URL: https://journals.ametsoc.org/view/journals/clim/aop/jcliD190901/jcliD190901.xml, doi:10.1175/JCLI-D-19-0901.1.

- Xia, Y., Xu, W., Hu, Y. et al. Southern-Hemisphere high-latitude stratospheric warming revisit. Clim Dyn 54, 1671–1682 (2020). https://doi.org/10.1007/s00382-019-05083-7

CONFERENCE PRESENTATIONS

2019	**How South American Topography Influences Climate Simulation over the South Pacific Ocean in CESM**, In 2019 AGU Annual Fall Meeting, San Francisco

2019	**Using Satellite Data to Improve Climate Model Simulations Tropical Pacific**, In 2019 NASA Summer School on Satellite Observations and Climate Models, JPL, Pasadena
2020	**How South American Topography Influences Climate Simulation over the South Pacific Ocean in CESM**, In 100th American Meteorological Society Annual Meeting, Boston
2020	**The Andes and ENSO Statistics Correction**, In 14th Annual Graduate Climate Conference, online
2021	**The Andes and the Tropical Pacific Climate.** In Atmosphere, Oceans, Climate Dynamics Seminar, Yale University.
2022	**The Andes and ENSO Statistics Correction**, In 2021 AGU Annual Fall Meeting, New Orleans & 2022 AGU Ocean Science Meeting, online
2022	**Topological Signature of Stratospheric Poincare - Gravity Waves,** in the 23rd Conference on Atmospheric and Oceanic Fluid Dynamics, Breckenridge, Colorado

TEACHING EXPERIENCE

Fall 2019	**Teaching Assistant**: Brown University, Principles of Planetary Climate under J.E Lee.
Fall 2020	**Teaching Assistant**: Brown University, Introduction to Oceanography under S. Clemens.

CERTIFICATE

2018-2019	**Sheridan Teaching Seminar - Reflective Teaching.** Brown University.
2019	**Winter 2019 GIS Institute:** Spatial Structures in the Social Sciences Fellow. Brown University.

OTHER EXPERIENCES

2019	**Coordinator:** Climate and Environment Lunch Seminar, Brown University Department of Earth, Environmental and Planetary Sciences.
2019-2020	**Coordinator**: Department of Earth. Environmental and Planetary Sciences (DEEPS), Science Teaching Education Program (STEP).
2020	**Peer Mentor:** Department of Earth. Environmental and Planetary Sciences (DEEPS) First Years Mentoring Program.
2021	**Graduate Student Representative:** Department of Earth. Environmental and Planetary Sciences (DEEPS) Faculty Representative.

Acknowledgments

Ph.D. is a very long journey. I grew up a lot and learned a lot in the past four years. I would not describe my Ph.D. life as struggling, because I made good progress with a steady pace and my researches are very interesting. I would not say it is easy either, because I did spent a hard and lonely time getting locked down by COVID, being far away from family and friends. But looking back to these experiences, I am full of gratitudes and no regrets.

I am lucky enough to spend a very enjoyable and rewardful Ph.D. at Brown where I met very lovely advisors and friends. I would like to thank my advisors Prof. Jung-Eun Lee and Prof. Baylor Fox-Kemper. Jung-Eun guided me into the area of climate science with a lot of patience. During my first semester, I knew very little about climate science or climate modeling, and she read one chapter of a textbook with me every week to learn the basics of climate science, and taught me hand by hand about how to run climate models. She always encouraged me and told me that I should be very confident that I am the expert of my study area. During the COVID lock down, she always checked in with my mental and physical health. I feel a lot of care from her when I am studying in a foreign country. Baylor is a different style of advisor. Many times a short 10-minute conversation with him can solve my problems that I have been stuck in for days. He always looks very happy and is always laughing. He converts the spirit to me of 'there is no big deal' and 'I can figure it out'. He also taught me to believe in myself and can be skeptical to people's comments. I want to thank Professor Brad Marston, who I also respect as my co-advisor. I collaborated with him in an interdiciplinary project and I learned a lot from him. I was very careless when I made my poster for a presentation, but he spent a whole afternoon correcting the formats and details for me. He told me a very rigorous outline of the

format will let the audience believe that I am serious about my work. I should always hold this careful and serious altitude with my work in the future.

I want to thank my parents, who gave me a lot of support and love during my Ph.D.. They provided me a good environment so that I can pursue academic achievements and jump out of my comfort zone to see the bigger world. Many thanks to my friends in DEEPS, who spared no efforts in helping me getting through my coursework, exams and the difficult times.

My journey with climate science still goes on, and I look forward to discovering more interesting questions after my Ph.D..

Abstract of "Interaction between the Andes and the Climate System, and the Waves Studies" by Weixuan Xu, Ph.D., Brown University, December 2022

We used global climate models to study the interaction between the Andes and the climate system. We found that the errors in the tropical Pacific climate simulation might be related to the incorrect representation of the Andes in the low-resolution global climate models. We adjusted the height of the Andes to the maximum height instead of the average height and ran the Higher Andes versus Default experiments. In a slab ocean model, we found that the Higher Andes experiment can more effectively adjust the mid-latitude westerly wind and form a stronger equatorward circulation. As a result of the evaporative cooling and radiative cooling, the eastern tropical Pacific Sea Surface Temperature (SST) gets lower and precipitation gets inhibited over the South Pacific, leading to a more accurate simulation for the mean state climate. As a follow up, we ran these two experiments in the fully-coupled model to study the ENSO variations. The results show that the Higher Andes setting can reduce the amplitude of ENSO as well as producing a more irregular and asymmetric cycle. The Andes also influences the land precipitations. We used a higher resolution global model and showed that without the Andes, the moisture flux from the Amazon forest can not be directed to the La Plata basin, and the severe storms on La Plata basin no longer exist. Lastly, we carried out a related side project about using topology to study climate waves. Using reanalysis data, we proved the existence of non-trivial topology in Poincaré waves by finding a vortex / antivorex pattern in the wavevector space, which is consistent with the theoretical simulations.

Contents

List of Figures

Chapter 1

Introduction

1.1 How the Andes interact with the climate system

1.1.1 How Mountains interact with climate

Atmospheric circulations are closely related to the topography distribution on earth. Depending on their shape, orientation, size, and location, the mountains may have different effects on the atmospheric circulation and convective systems.

The most simple and general example is when a stable airflow climbs up the mountain, the air will be forced upward following the mountain slope, creating cloud and precipitation on the wind side and strong evaporation on the lee side. But for a lot of other the situations, the interactions are more complicated [Houze Jr., 2012]. For example, if the airflow is unstable or has strong shear, convection will be initiated on a small scale and spread discontinuously along the uphill. When the mountain is much lower than the precipitating clouds, the precipitation can be sustained across the mountain but much weaker at the lee side. On the contrary, if the mountain is large enough, the lower layer air will not be able to cross the mountain; instead, it will pile up at the foothill. The upper air rises on top of this surface layer before it reaches the mountain, causing rainfall ahead of the upslope.

The Andes and the Rocky mountains, oriented in the north-south direction, blocks zonal air flow. The zonal air flows will be forced to move meridionally, resulting in the stretching and squeezing as well as upward or downward motions [Wang and Fu, 2004]. These two mountains create large contrast in the wind and moisture features on their east and west. In the meanwhile, orographic Rossby waves will be generated after the airflow crosses the mountain, resulting in the zonal difference in precipitation and temperature [Wills and Schneider, 2018].

Meanwhile, the Tibetan Plateau, oriented in the east-west direction, has a different dynamic mechanism for regulating the South Asia monsoon. Boos and Kuang [2010]

suggests that the South Asia monsoon is related to the blocking by the narrow and high orography of the Himalayas. Similarly, Park et al. [2012] suggests that the mechanical downstream convection plays a key role in the presence of the East Asian monsoon.

The mountains can influence the climate system in many different ways. In this thesis, I will focus on the influence of the Andes on the tropical Pacific and South American climate.

1.1.2 The Andes and atmosphere circulation

Located on the west coast of South America, the Andes is a north-south oriented mountain with a length of 8900 km that covers the latitude from 10°N to 50°S. It is a narrow and high mountain area, with an average elevation of 4 km and an average width of 500 km [Molina and Little, 1981]. The presence of the Andes is important for the formation of the climate system of the tropical Pacific as well as South America.

The two most important flows that interact with the Andes are the low-latitude easterly wind from the Atlantic Ocean and the mid-latitude westerly wind from the Pacific Ocean. When these two flows encounter the mountain, they will possibly turn equatorward or poleward. With the constraint of the Sverdrup balance:

$$\beta v_g = f\frac{\partial w}{\partial p} \tag{1.1}$$

The equatorward flow will decelerate upward (squeezing) and the poleward flow will accelerate upward (stretching).

For the low-latitude easterly flow, the equatorward motion will not be able to climb up the mountain and gets trapped at the east of the Andes, and this motion can not be sustained when it encounters the equator where Coriolis force disappears. As a result, the low-latitude easterly can only be directed poleward and go up. Part

of it will either climb across the mountain and reach the west side and part of it will move up to the hillside and move southward, forming the South America Low-Level Jet (SALLJ).

For the mid-latitude westerly flow, the equatorward flow will descend before it approaches the mountain and further become an easterly as it approaches the equator, creating an anticyclonic motion and reinforcing the tropical easterly wind at the Pacific Ocean. The poleward flow will ascend and climb across the Andes, initiating the orographic Rossby waves in the mid-latitude region [Rodwell and Hoskins, 2001].

As a result, the low-level jets along the Andes are equatorward-pointing at the west and poleward-pointing at the east. These two jets are part of the high-pressure anticyclonic system at the southeast Pacific and South Atlantic. The location of the high-pressure center will migrate north or south with the seasonal cycle, resulting in the change of the strength of these two jets at a different time of the year [Espinoza et al., 2020].

1.1.3 The Andes and precipitation

The difference in the atmospheric flows results in the difference in the hydroclimate system on different sides of the Andes.

At the west of the Andes, the subsidence motion from the cross-Andes easterly and the equatorward flow induces strong evaporation from the surface of the eastern Pacific, resulting in a low Sea Surface Temperature (SST) over the coastal region [Takahashi and Battisti, 2007b]. This subsidence motion creates capping effects and provides a favorable environment for low-level clouds [Wood, 2012]. The low-level clouds block the shortwave radiation from the sun and further lowers the surface temperature. In the meanwhile, the subsidence motion inhibits convection in the eastern Pacific, resulting in a cold and dry region the west of the Andes.

At the east of the Andes, the Amazon forest provides sufficient moisture that

is transported to the south by SALLJ [van der Ent et al., 2010]. Additionally, the SALLJ is trapped above by the cross-mountain westerly when it approaches the mid-latitude region, and this capping effect accumulates instability in the flow by latent and sensible heating on the surface. When the SALLJ reaches a small mountain range and releases its instability, it results in the most intense storms over the La Plata basin [Houze Jr., 2012].

In conclusion, the different flow directions create a dry region to the west of the Andes and a wet region to the east of the Andes, forming two very different hydrological and ecological environments.

1.2 Tropical Pacific climate and its formation

1.2.1 Tropical Pacific Climate

The atmosphere over the tropical Pacific is dominated by the zonal Walker circulation. The equator is dominated by easterly trade winds. When the moist and warm surface easterly encounters the western boundary, it rises and forms a convection center, with heavy rainfalls near Indonesia. On the contrary, the eastern branch of the Walker circulation is dominated by a downward motion, resulting in a cold and dry surface condition. In the upper atmosphere, the returning branch is from west to east, completing the Walker circulation circle.

Corresponding to the circulation in the atmosphere, the upper tropical Pacific Ocean also has zonally asymmetries features. With the surface easterly wind, the surface ocean water migrates west in absence of the Coriolis force near the equator. The warm surface water piles up in the western Pacific, forming a local warm pool that provides a sufficient supply for atmospheric convection. While in the eastern Pacific, the cold deeper ocean water moves up to compensate for surface water, resulting in a cold tongue. The subsidence motion in the atmosphere and the upwelling from

deeper ocean forms low SST over the eastern Pacific. Consistently, beneath the ocean surface, the thermoclines are tilted, deeper in the west and shallower in the east.

1.2.2 Shape of continents and the WES feedback

The first and initial difference that distinguishes the northern and southern Pacific is the shape of the North and South American continents. Philander et al. [1996] runs a global climate model by simplifying the shape of the American continents into a large triangle, with the western coast tilting from northwest to southeast. In the northern hemisphere, the tropical trade wind is from the northeast, and in the southern hemisphere, the trade wind is from the southwest, which means that the wind is perpendicular to the coastline in North America and parallel to the coastline in South America. Because of Ekman pumping, $F = f\hat{\mathbf{z}}\times\mathbf{u}$, the mixed layer ocean water mass transport is perpendicular to the direction of the surface wind, resulting in a parallel ocean current to the North American coast and a perpendicular ocean current to the South American coast. As a result, the South American coastal upwelling is more efficient than North America, resulting in a colder SST at the initial state.

This initial SST difference is then enlarged by the Wind-Evaporation-SST (WES) feedback suggested by [Xie and Philander, 1994a]. In the southern tropical Pacific, the lower SST results in a high surface pressure center, while in the north tropical Pacific, there is a low surface pressure center. A cross-equator wind from south to north is initiated by this pressure gradient. With the Coriolis effect, the southerly wind will be accelerating the easterly trade wind in the southern hemisphere and decelerating the easterly trade wind in the northern hemisphere. The stronger wind in the southern tropical Pacific then induces more evaporation and further lowers the SST. This is positive feedback that formulates the north-south SST gradient over the Pacific ocean.

1.2.3 The Andes and the cloud effects

In addition to the shape of the continents, another important factor for the southeast Pacific cold tongue is the Andes. When the mid-latitude westerly wind from the Pacific encounters the Andes, the isentropic surfaces of the atmosphere get squeezed. According to the Sverdrup balance (Equation 1.1), with $\frac{\partial w}{\partial z} < 0$ with the squeezed isentropes, and $f < 0$ in the southern hemisphere, the mountain will initiate a positive v_g which means the flow will turn towards the equator [Geerts and Linacre, 1997]. This equatorward turning will enhance the anticyclonic motion over the tropical south Pacific, strengthening the high-pressure center with downward motion and inducing more evaporation over the ocean surface.

The radiation-cloud feedback further lowers the southeast Pacific SST. With the high-pressure center and the low SST, the southeast Pacific provides a favorable environment for low-level clouds. These low-level clouds reflect solar radiation and bring a cooling effect to the ocean surface, developing positive feedback for the cold and dry environment [Wood, 2012].

1.3 El Niño Southern Oscillation

El Niño and La Niña are the positive and negative phases of the climate variation in the tropical Pacific area. During an El Niño event, the Eastern Pacific experiences abnormally high sea surface temperature (SST). The resulting decrease in the east-west SST gradient is accompanied by a flattening of the thermocline in the tropical Pacific and weaker upwelling in the Eastern Pacific coastal area [Guilyardi et al., 2009]. In the atmosphere, the easterly wind is weaker than usual, and the precipitation center migrates to the east, causing much stronger rainfalls in the central Pacific. The La NiNã phase is the opposite situation. El Niño and La Niña are periodic events that occur every 2-7 years. Usually, an El Niño is followed by La Niña after a few months

[Neelin, 2011].

1.3.1 Initiation: Westerly Wind Burst and Bjerknes Feedback

The initiation of ENSO is commonly thought to be the Westerly Wind Bursts (WWBs), which is defined as a strong rush of westerly wind occurs in the equatorial Pacific trade wind region, with a strength of at least 7 m/s and duration of 5–20 days [Harrison and Vecchi, 1997]. The occurrences of WWBs are related to the tropical cyclones [Keen, 1982] or the Madden–Julian Oscillation (MJO) [Kessler, 2001]. The WWBs have 3 major effects on the change in SST. First, they cool the western Pacific warm pool by strong evaporative cooling [McPhaden, 2002], reducing the east-west SST gradient. Secondly, the WWBs cause the surface currents to accelerate to the east [McPhaden et al., 2020]. Third, WWB generate downwelling Kelvin waves that transport subsurface temperature anomalies [Ando and McPhaden, 1997].

However, WWBs occur at the frequency of about 3 times a year [Verbickas, 1998], much higher than the frequency of ENSO. Another important process that develops a WWB event into El Niño is the Bjerknes feedback. This is a positive feedback system between the wind stress, the sea surface temperature (SST), and the upper ocean thermocline. In the onset of an El Niño event, a WWB event weakens the easterly trade wind that dominates the tropical Pacific region. When the surface warm water is not transported to the west warm pool and the upwelling in the east cold tongue is weakened, the east-west SST gradient is weakened and the thermocline is flattened. The smaller SST gradient results in a smaller pressure gradient, which further weakens the strength of the easterly wind. During a La Niña event, the situation is the opposite.

1.3.2 Procession: tropical waves

The procession of an ENSO cycle is closely related to the propagation of the equatorial Kelvin and Rossby waves. The WWB events initiate the downwelling Kelvin waves that carry the warm temperature anomalies eastward. The Kelvin waves take about 2 months to travel across the Pacific, and when they reach the eastern Pacific cold tongue, they depress the thermocline and reduce the upwelling of the thermocline water, resulting in the peak of an ENSO event [Wyrtki, 1975].

When WWBs trigger downwelling Kelvin waves, they also initiate upwelling Rossby waves off the equator at the same longitude. These upwelling Rossby waves propagate westward at 1/3 of the speed of Kelvin waves, and when they encounter the western boundary, they reflect back as upwelling Kelvin waves that carry a warm temperature anomaly. These Kelvin waves with cold anomaly later reach the eastern Pacific after the warm anomaly and result in a following La Niña event [Battisti, 1988].

1.3.3 Simple ENSO models

In order to understand the irregular but periodic features of ENSO cycles, several theoretical models have been suggested to understand the mechanism.

The most simplified model is a two-box model by Jin [1997a,b], and it was calculated on top of Cane and Zebiak [1985] and Wyrtki [1985]. This is a two-boxes model and the dominant equations are:

$$\begin{cases} \frac{dT_w}{dt} = -\varepsilon_T(T_w - T_r) + \frac{M(-u)(Te-Tw)}{L/2} \\ \frac{dT_e}{dt} = -\varepsilon_T(T_e - T_r) + \frac{M(w)(Te-Tse)}{Hm} \end{cases} \tag{1.2}$$

T_w and T_e are the SST in the Western and Eastern Pacific. The first terms in Equations (1) and (2) are the heating from the radiative, sensible and latent heat fluxes on the surface of the ocean. T_r is the equilibrium temperature from the radiative

and convective balance. For the second terms in Equations (1) and (2), the function $M(x)$ represents the upstream difference.

This box model considers the temperature variations in the eastern and western Pacific as results of radiation, temperature difference, and ocean currents. The simulation results it gets to capture the temperature variation in the tropical Pacific over a period of 4 years.

A more complicated model has been suggested by Vaart et al. [2000].In this model, they use a meridionally symmetric coupled system to study the ENSO cycle. The Pacific basin is no longer simply divided into a few boxes and the SST depends on both space and time. The dominant equation is:

$$\partial_t T + \varepsilon_w (T - T_0) + \frac{w_1}{H} \mathcal{H}(w_1)(T - T_{sub}(h)) + u_1 \partial_x T + v_1 \partial_y T = 0 \qquad (1.3)$$

The ocean model has a shallow-water layer of average depth H and an embedded mixed layer of fixed depth H1, the zonal length of the ocean is L and the meridional direction is unbounded. ε_w is the Newtonian cooling coefficient and T_0 is the equilibrium radiative temperature. The first term represents the adjustment towards the radiative equative equilibrium SST. The second, third and fourth term represents the advection of temperature. (u, v, w) is the shallow-water layer velocity field and (u_s, v_s) are the Ekman velocities determined by the wind stress. $u_1 = u_s + u$, $v_1 = v_s + v$ and $w_1 = w_s + w$. $\mathcal{H}$ is the Heaviside function. This model assumes that the tropical Pacific tends to adjust towards a radiative and convective equilibrium, whereas the dynamics are causing the departures from this equilibrium.

This model considers the contribution of each location's temperature in terms of zonal, meridional and vertical velocities as well as radiation. It captures the propagation pattern of Kelvin and Rossby waves, which is essential to the explanation of recharge oscillator theory and the time scale of ENSO. The propagation of the Rossby waves contributes to the recharge and discharge of the equatorial thermocline. When

the wind stress curl changes to an opposite sign, the Rossby wave continues to propagate. The interval in the ocean's dynamic adjustment to changing wind stress is responsible for the phase transition of ENSO.

However, these simplified models fail to reproduce the irregular 2-7 years cycle of ENSO. The irregularity is closely related to the model's complexity and chaotic forcing, both within and outside of the tropical region. These complexities are better captured and represented by Atmosphere-Ocean General Circulation Models (AOGCMs), which can simulate near real-world ENSO cycles.

1.4 Topological waves

Topology has first been suggested to be applied to the study of climate waves by Delplace et al. [2017]. To better understand the similarity between climate waves and the topological insulator, we need to understand the wave property and the topology concepts.

1.4.1 Waves System

Here, we will consider the simplified situation with the β-plane approximation, where the y derivative of the Coriolis frequency is a constant: $\beta = \frac{\partial f}{\partial y}$.

If we consider a simplified version of the shallow water equation, by ignoring the frictions and wind stress:

$$\begin{cases} \frac{\partial u}{\partial t} - \beta y v = -g\frac{\partial h}{\partial x} \\ \frac{\partial v}{\partial t} + \beta y u = -g\frac{\partial h}{\partial y} \\ \frac{\partial h}{\partial t} + H(\frac{\partial u}{\partial x} + \frac{\partial v}{\partial y}) = 0 \end{cases} \tag{1.4}$$

The different types of waves are the solutions of this set of the equation under

different approximations.

The Kelvin waves only exist at the equator, and their existence depends on the boundary condition at the equator that the meridional velocity vanishes. Therefore, for Kelvin waves, these equations can be simplified as:

$$\begin{cases} \frac{\partial u}{\partial t} = -g\frac{\partial h}{\partial x} \\ \beta y u = -g\frac{\partial h}{\partial y} \\ \frac{\partial h}{\partial t} + H\frac{\partial u}{\partial x} = 0 \end{cases} \tag{1.5}$$

And we obtain the dispersion relation for Kelvin waves as $\omega = \sqrt{gh}k$. This dispersion relation tells us that the frequency and wavenumber of Kelvin wave have a linear correlation. The wavenumber can only be positive, indicating an eastward-only propagation direction for Kelvin waves.

For the Rossby, Poincaré, and Yanai waves, by doing a Fourier transform on the shallow water equation, the zonal and vertical equations become linear but the meridional equation is not:

$$\frac{d^2\tilde{v}}{dy^2} + (\frac{\omega^2}{c^2} - k^2 - \frac{\beta k}{\omega} - \frac{\beta^2}{c^2}y^2)\tilde{v} = 0 \tag{1.6}$$

To have non-zero solutions away from the equator, the frequency and wavenumber have to satisfy the discrete dispersion relationship:

$$\frac{\omega^2}{c^2} - k^2 - \frac{\beta k}{\omega} = (2n+1)\frac{\beta}{c} \tag{1.7}$$

This solution applies to all the above-mentioned waves with different values of n. When n=-1, it represents the Kelvin waves. When n=0, it represents Yanai waves. When n=1,2,3,... it represents Poincaré or Rossby waves.

The approximation between Rossby and Poincaré waves is that Poincaré waves have a higher frequency, so we can ignore $\beta k/\omega$, and the dispersion relation is $\omega^2 =$

$c^2k^2 + (2n+1)\beta c$.

For Rossby waves with lower frequency, we can ignore ω^2/c^2, and the dispersion relation becomes: $\omega = -\frac{\beta k}{k^2+(2n+1)\beta/c}$. Therefore, Rossby waves have negative wavenumber and only migrate westward.

Yanai wave is also called mixed Rossby-gravity waves, and it also only occurs at the equator. It has antisymmetric phase patterns north and south of the equator. The eastward-propagating Yanai waves behave like Poincaré waves and the westward-propagating waves behave like Rossby waves.

The dispersion relation for all these waves can be shown in Fig. 1.1.

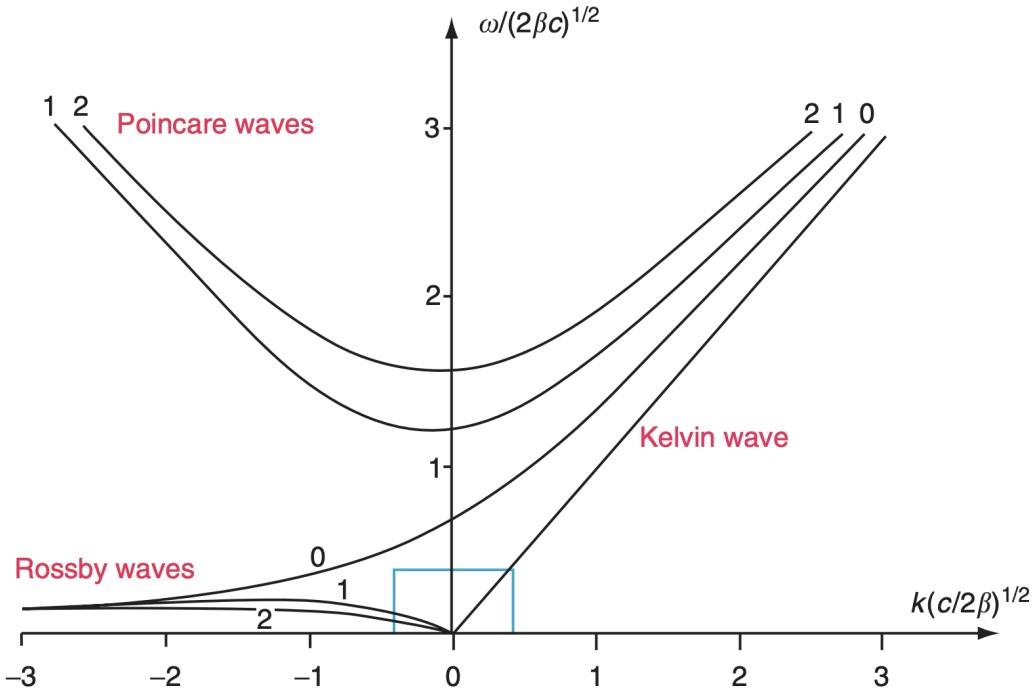

Figure 1.1: Dispersion relation for different waves. Figure from Fedorov et al. [2009]

1.4.2 Topology

In condensed matter areas, topology is often used to explain the topological insulators. A simple example of topology is the hairy ball theorem (also called the hedgehog theorem in Europe) [Renteln, 2013]. The hairy ball theorem tells us that a sphere

with odd dimensions can not have tangent vector fields that can exist all over its surface. This property is what distinguishes a ball from a donut, and it does not change with continuous deformation. Topology classifies one family to another, and members in the same family share the same property and can deform continuously to each other, which can help us simplify the problems. This non-trivial property can be quantified by a topological invariant, which in the hairy ball example can be understood by the number of holes on the sphere's surface, and in physics, it is called the Chern number.

When the topological invariant changes, there will be the existence of gapless conducting states at interfaces. These edge states no longer conserve the topological properties, and they only exist in the boundary between different gauges. The edge state has an asymmetric property in that it propagates only in one direction along the boundary. An example in quantum physics is when skipping motion electrons execute as their cyclotron orbits bounce off the edge. This bouncing motion is chiral and it only moves in one direction. This chiral property of the edge modes makes it immune to many types of disorder, and it is not sensitive to background situations. The Chern number difference predicts the number of edge modes that exist between the states. This chiral edge state can also be expressed as the edge connection band between different states having a positive group velocity. This positive group velocity can be the different combinations of left and right moving modes, but the difference between them is determined by the topological bulk states and the difference in Chern number between these states. This phenomenon is called bulk-boundary correspondence [Hasan and Kane, 2010].

The same theory can be applied to the climate waves in the earth system. The rotation of the earth breaks the time reversal symmetry and separates the northern and southern hemispheres as different gauges, and the equator as a boundary [Delplace et al., 2017]. Because of the opposite signs of Coriolis frequency in the Northern and

Southern Hemisphere, Poincaré waves in the Northern Hemisphere have the winding number of 1 and the winding number becomes -1 in the Southern Hemisphere. Due to the winding number difference of 2 between the different hemispheres, there must be the existence of 2 edge modes at the equator. In reality, we do observe these two different equatorial trapped modes as Kelvin waves and Yanai waves (Figure 1 in Kiladis et al. [2009]). Similar to the one-directional bouncing of the cyclotron, the equatorial Kelvin and Yanai waves only propagate towards to the east, and they are also robust to the perturbations.

1.5 Outline of the thesis

In this thesis, the main idea is to understand how the Andes influences the climate system, and how to apply topology theory in climate waves. The slab-ocean climate modeling project about how the Andes influence the mean-state eastern Pacific climate is in Chapter 2. The atmosphere-ocean coupled modeling project about how the Andes influence ENSO variations is in Chapter 3. The high-resolution modeling project about how the Andes influences South America land precipitation is in Chapter 4. The project about diagnosing topological patterns in stratosphere Poincaré waves is in Chapter 5. The summary of the thesis and future works is in Chapter 6.

Chapter 2

The Andes and the Southeast Pacific Cold Tongue Simulation

2.1 Introduction

Changes in the tropical Eastern Pacific climate has significant influence on global and regional climate systems [Xie et al., 2007]. In the tropical Pacific, the easterly trade wind moves warm surface ocean water towards the Western Pacific and forms the Western Pacific warm pool. Upwelling of deep ocean water in the Eastern Pacific lowers the sea surface temperature (SST), forming the Eastern Pacific cold tongue. The ascending branch of the Walker Circulation is located in the Western Pacific warm pool region and is accompanied by heavy rainfall, while the descending branch is located in the Eastern Pacific cold tongue accompanied by strong lower-troposphere stability and low-level clouds [Xie, 1998]. Ocean-atmosphere interaction in this region leads to the El Niño–Southern Oscillation (ENSO) phenomenon [Dommenget, 2010], which influences temperature and precipitation of other regions [Leathers et al., 1991] by the Pacific/North America (PNA) teleconnection pattern [Yeh et al., 2018]. Furthermore, climate model study suggests that the cooling in the Eastern Pacific in the recent decade is responsible for the slowing down of global warming trend [Kosaka and Xie, 2013]. Therefore, the correct simulation of the climate over this region is crucial.

Despite its importance, there is a large bias in simulating the Eastern Pacific climate. Climate models have difficulty in simulating the Eastern Pacific climate where low-level clouds are formed by large scale descending air [Bony, 2005]. Analysis of climate models from the phase 5 of Coupled Model Inter comparison (CMIP5) [Taylor et al., 2012] reveals that most models simulate too high SSTs and too much precipitation in the tropical Southeastern Pacific [Wang et al., 2014]. The overestimation of precipitation in the tropical South Pacific leads to the double Intertropical Convection Zone (ITCZ) problem [Takahashi and Battisti, 2007a].

Previous studies have suggested that the SST and precipitation biases are closely related to the atmospheric energy budget in climate models [Hwang and Frierson,

2013, Li and Xie, 2014, Adam et al., 2016]. Adam et al. [2018] and Boos and Korty [2016] argue that the asymmetric SST bias is related to the hemispherically and zonally uneven heating anomalies, possibly due to the errors in simulating the radiative effect of clouds and the strength of Atlantic Meridional Overturning Circulation (AMOC) [Wang et al., 2014]. Overall, studies suggest that models simulate too little reflection of shortwave radiation [Williams et al., 2013], and as a result the Southeast Pacific is too warm.

These above mentioned biases result in a more symmetric distribution of SST and precipitation over the Pacific Ocean in the Northern Hemisphere (NH) and the Southern Hemisphere (SH). However, average SSTs are higher in the NH than in the SH, and the ITCZ is located in the NH [Marshall et al., 2014]. For SST, the asymmetry is probably related to the uneven distribution of continents and topography. Philander et al. [1996] suggests that the shape of South America is more favorable for upwelling, forming low SSTs on the Southeast Pacific. Moreover, the relatively low SSTs in South Pacific form a regional high surface pressure while the higher SSTs in North Pacific form a low surface pressure. This asymmetric pattern brings an anticyclonic motion in the South Pacific and a cyclonic motion in the North Pacific. These motions strengthen the easterly trade winds in SH and weaken that in NH. The stronger trade winds in SH further decrease SST with wind-evaporation-sea surface temperature (WES) feedback [Xie and Philander, 1994b].

For precipitation asymmetry, Takahashi and Battisti [2007a] argued that the Andes is the most important driver for the northward distribution of the Eastern Pacific ITCZ. The Andes blocks the mid-latitude westerlies from the Pacific Ocean, and squeezes the isentropic surface as low-level air approaches the Andes. To conserve potential vorticity, the mid-latitude winds have to turn equatorward as it descend. This effect brings cold and dry air from the polar region and enhances the anticyclonic motion [Rodwell and Hoskins, 2001] as well as the subsiding motion in SH. This

dynamic motion also affects the formation of clouds. Because ITCZ is located in NH, the southern branch of the Hadley circulation is stronger, enhancing the descent over the Southeast Pacific region. The enhanced decent helps maintain boundary layer clouds [Mechoso et al., 1995] and temperature inversion above the cold tongue [Wang et al., 2004].

Several experiments have highlighted the importance of the Andes in the formation of the climate features (e.g. clouds and SSTs) and energy transport over the Pacific. Xu et al. [2004] removed the Andes in a regional climate model and showed that the removal of Andes caused a significant reduction of stratocumulus clouds and decrease in absorption of solar radiation on the sea surface in the Southeast Pacific. Feng and Poulsen [2014] changed the elevation of the Andes from 1 to 3 km and found that the uplift of the Andes accounts for half of the cool SST over the cold tongue and significantly strengthens the Walker circulation and cloud radiative cooling. In addition, using aqua-planet modeling experiments, Maroon et al. [2015] showed that adding the Andes did lower the SST over the Southeast Pacific and cause a northward propagation of the ITCZ.

The Andes is very important for the maintenance of the SST and precipitation features in the Southeast Pacific. However, because it is a narrow mountain range, its elevation may be too low to influence the Southeast Pacific climate when the topography is smoothed in low resolution models. As a result, it cannot effectively block the mid-latitude westerlies. Xu et al. [2004] and Gent et al. [2010] showed that a higher resolution climate model has a better performance in simulating the wind and temperature pattern, and this is mainly because of the better resolved orography. Therefore, we hypothesize that the CMIP5 model bias in the Southeast Pacific is related to the topography settings in climate models. We modified the topography setting in South America and examined the influence of the topographic smoothing of the Andes on the Southeast Pacific climate. Our results show that when the low-level

wind is properly blocked by the Andes, SSTs in the Southeast Pacific decrease as a result of enhanced wind and low-level clouds. The rest of the paper is organized as follows. Section 2 introduces the climate model and the model settings of our experiments. Section 3 compares the precipitation and SST of model results with control and higher Andes cases, as well as the climate sensitivity for the elevation of the Andes and the change in atmospheric energy transport. Section 4 summarizes our findings.

2.2 Methods

2.2.1 Model Description

We used the National Center for Atmospheric Research (NCAR) Community Earth System Model (CESM) version 1.2.2. The Community Atmospheric Model, version 4 (CAM4) is the atmosphere component of CESM. We ran the model with the finite volume (FV) dynamical core and a slab ocean. In a slab ocean model, only the interaction between atmosphere and mixed layer of the ocean is considered, and the SST is determined by the depth of mixed layer and the energy fluxes [Lee, 2019]. Although a slab ocean model ignores the change in the ocean circulation, it is widely used to study the response of the climate system to an imposed forcing because the atmosphere adjusts very fast to the environment. The ocean circulations take hundreds to thousands of years to reach an equilibrium [Neale et al., 2013], so a slab-ocean model can capture the fast response resulting from the atmospheric circulation.

To assess the skill of CESM-CAM4 and the effects of changing topographic setting of the Andes in simulating Southeastern Pacific, we compared our model results with instrumental records. For SST, we used the average of mean annual SST from 2004 to 2018 derived from the Hadley Centre Sea Ice and Sea Surface Temperature (HADISST) data set ($1^\circ \times 1^\circ$)[Rayner et al., 2003]. For precipitation, we used the

average of mean annual precipitation over 1979-2018 from the Tropical Rainfall Measuring Mission (TRMM) for comparison with models [Kummerow et al., 1998].

2.2.2 Experiments

Compared with the 1-km high-resolution topography from the National Oceanic and Atmospheric Administration (NOAA) National Geophysical Data Center (NGDC) Global Land One-km Base Elevation (GLOBE) topography [Hastings and Dunbar, 1999] (Fig. 2.1a), 1.9°×2.5° resolution of the CESM control case has much smoothed topography (Fig. 2.1b). In our experiment, we take the highest elevation within each model grid point along the Andes, as shown in Fig. 2.1c, so that the Andes can effectively block the zonal winds. The model results for the original topography setting (Fig. 2.1b) will be referred to as the control run, and the output for the modified elevation (Fig. 2.1c) will be referred to as the 'Higher Andes' case. To compare with modern satellite data, the CO_2 concentration is set to be 400 ppm.

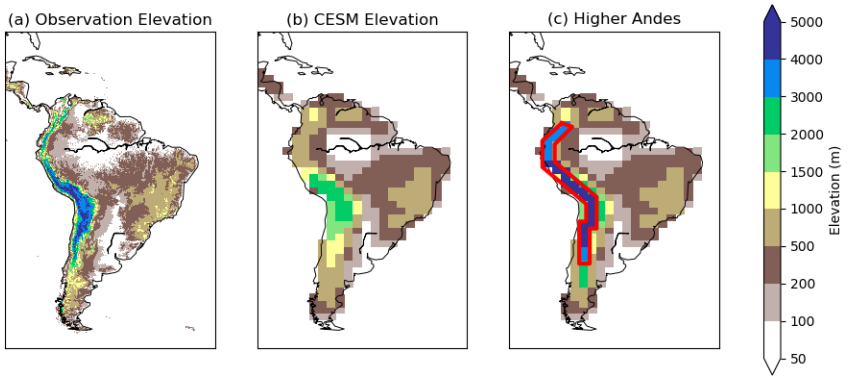

Figure 2.1: Elevation in South America from (a) National Oceanic and Atmospheric Administration (NOAA) National Geophysical Data Center (NGDC) Global Land One-km Base Elevation (GLOBE) topography, (b) $1.9^o \times 2.5^o$ resolution of CESM control run, and (c) Higher Andes topography. The area where we performed the sensitivity test is marked with a red line.

In order to examine how different elevations of the Andes affect the Southeast

Pacific climate, we also ran a series of sensitivity tests for the elevation of the Andes. We set the elevation of the region within the red line in Fig. 2.1c to 50 m, 1 km, 2 km, 3 km, 4 km, 5 km and 6 km.

2.3 Results and discussion

2.3.1 Change in SST

Compared with the observations, simulated SST in the control run is too high in the Pacific, particularly in the northern and southern tropical/subtropical Pacific between 20°S and 20°N (Fig. 2.2d). In the North Pacific, the overestimation is most severe near 20°N and 120°W on the west coast of North America with the magnitude of 3°C, and it expands toward the central Pacific. In the South Pacific, the SST bias is highest near the west coast of South America and also expands toward the central Pacific. This bias is about 2°C on average. The regions where SST is overestimated in the region from 160°E to 80°W in the South Pacific over tropical region, which means that the extent of the cold tongue in the South Pacific is underestimated. In mid latitude area of the Northwest Pacific, the SST is abnormally cold compared with the observation (Fig. 2.2d). The change in the Atlantic ocean and Indian ocean is not as obvious as in the Pacific ocean (Fig. S1), so it is not shown in the main text.

The warm SST bias in the South Pacific in the control run is reduced in the Higher Andes case. (Fig. 2.2ef). In 0-20°S, the SST difference decreases from 1.47°C to less than 0.40°C. It also induces the Pacific/North American teleconnection pattern (PNA) in the North Pacific (Fig. 2.2f), with positive SST anomaly over mid and high latitude North Pacific and negative SST anomaly over tropical Pacific, similar to the results from Kosaka and Xie [2013]. This teleconnection explains how the cooling over the Southeast Pacific SST also eliminates the SST bias over the tropical North Pacific to some extent, by triggering Rossby waves which transports a cold SST signal

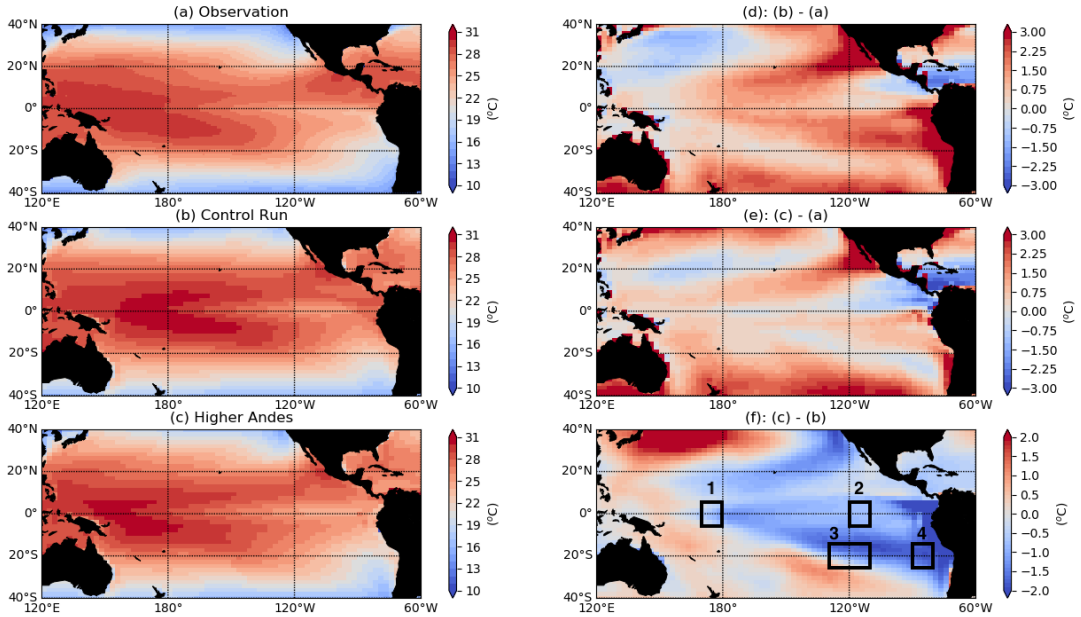

Figure 2.2: Left panel: Annual mean Sea Surface Temperature from HADISST (a), control CESM (b), and higher Andes CESM (c). Right panel: SST difference between control and HADISST (d), High Andes and HADISST (e), and High Andes minus control (f). The box 1 to 4 in (f) are the areas where we did the energy budget analysis.

in the tropical area to the subtropical regions as a warm SST signal [Dai et al., 2017].

To quantitatively show the change due to the modification of the Andes, we calculated the Root Mean Square Error (RMSE) between the model outputs in each case and the HADISST (Table 2.1). In the tropical North Pacific, the RMSE has been reduced by 6.5%, while in the tropical South Pacific, it has been reduced by 22.3%. The overall RMSE over the tropical Pacific is reduced by 15.1%.

Table 2.1: Root Mean Square Error (RMSE) for SST. Tropical Pacific is the ocean region from 120^{o}E to 60 ^{o}W, 40^{o}S to 40^{o}N.

SST RMSE (^{o}C)	Tropical Pacific	NH Tropical Pacific	SH Tropical Pacific
Control	1.52	1.37	1.66
Higher Andes	1.29	1.28	1.29

Our results suggest that the evaporative cooling and radiative cooling reduced the

bias in the Southeast Pacific SST (see below). Evaporative cooling accounts for the lowering of SST in the central South Pacific, while the radiative cooling explains the change in coastal areas of South America.

The evaporative cooling comes from stronger winds. In the tropics, the zonal wind blows from east to west. Near the west coast of South America, the strong northward wind induces the Ekman transport away from the coast of surface ocean water, resulting in low SSTs in the Southeast Pacific. Around 120°W in the South Pacific, the low latitude easterlies, mid-latitude westerlies and the equatorward wind on the coast of South America form an anticyclonic motion, establishing a high surface pressure center in the Southeast Pacific (Fig. 2.3a).

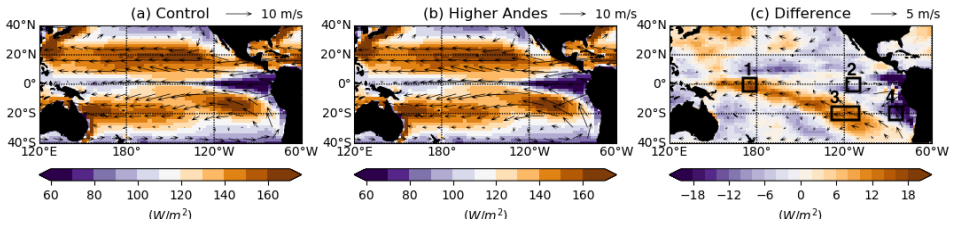

Figure 2.3: Contour: Surface latent heat. Arrows: Horizontal wind at 850 hPa. (a) Control run, (b) Higher Andes run, (c) Their difference. Box areas are the same as Fig. 2.2.

By increasing the elevation of the Andes, the northward motion near the west coast of South America, as well as the easterlies near 20°S, is enhanced (Fig. 2.3c). The stronger northwestward surface air flow induces evaporation over the ocean, increases latent heat flux, and results in a lower SST in the central South Pacific. We compared the surface wind distribution with the ECMWF reanalysis data (Fig. S2), but it is difficult to tell if there is an obvious improvement due to the large discrepancy.

The radiative cooling comes from the increase of low-level clouds. Xu et al. [2004] found that the narrow steep Andes has a significant contribution to the formation of clouds over the Southeast Pacific, and therefore results in the latitudinal asymmetry in the Eastern Pacific climate. In our experiment, the change in the coastal Southeast

Pacific climate is the result of the change in low-level cloud fraction. The higher Andes setting in the model enhances the descent motion of air over the subtropical ocean, forming a low-level trade inversion and low-level marine boundary layer (MBL) clouds (Fig. 2.4a) [Bony, 2005]. This region covers the longitude from 120°W to 80°W in subtropical area of the Southeast Pacific. The radiative effects of low clouds decrease local SSTs.

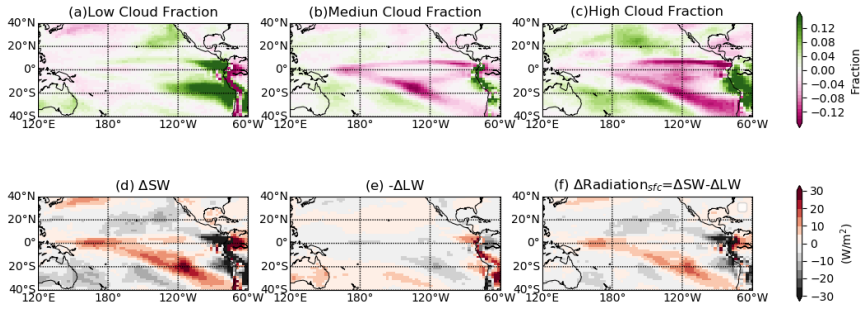

Figure 2.4: (a)-(c): Changes in cloud fraction from higher Andes to Control cases.. (a) low-level clouds (Surface pressure to 700 mb), (b) medium-level clouds (700 mb to 400 mb) and (c) high-level clouds (400 mb to the model top). (d)-(f): Changes in surface radiation. (a) incoming shortwave, (b) outgoing longwave, (c)net radiation at the surface. Box areas are the same as Fig. 2.2.

Fig. 2.4b and 2.4c show the change in medium and high cloud fraction. Both medium and high cloud fractions show a decrease in the same region where SST is lowered (Fig. 2.2f). The decrease of medium and high clouds ends up with a weaker warming radiative effect. Medium and high clouds show an increase in the Southwest Pacific where precipitation bias in the South Pacific Convection Zone (SPCZ) is improved (Section b).

To examine the radiative effect from the change of cloud fraction, we show the distribution of energy budget at the surface (Fig. 2.4d-f). Therefore, we examine the distribution of the change in shortwave radiation (Fig. 2.4d), outgoing longwave radiation (Fig. 2.4e) and change of energy absorption at the surface (Fig. 2.4f).

Our results show that with the higher Andes, the absorbed solar radiation shows a decrease near the west coast of South America at the latitude near 20 °S where low-level clouds increase. From the equatorial Western Pacific to the Southeast Pacific, both incoming shortwave energy and outgoing longwave energy increases as a result of the decreasing medium and high cloud fractions in this area. However, the incoming shortwave radiation increases by a great amount and the increase of outgoing longwave radiation only offsets a small part of it. As a result, the overall change of the surface radiation still shows an effect of heating up the major areas of the South Pacific, and cooling down the coastal area of South America.

To analyze how much different types of energy accounts for the decrease in the SST under the modification of the Andes topography, we took 4 boxes as shown in Fig 2.2 where SST is decreasing and calculated the average energy change within each box (Table 2.2). In the equatorial Western Pacific (Box 1) and central South Pacific (Box 3), the surface is absorbing more shortwave radiation, but it is balanced by the increased outgoing longwave radiation and stronger evaporation. In the coastal region of South America (Box 4), the evaporation is getting smaller, and the incoming shortwave radiation has decreased by a greater amount. For the region over the tropical Western Pacific (Box 2), the high-level cloud fraction has reduced with the Higher Andes setting (Fig. 2.4c), increasing upward longwave radiation and decreasing SST.

Table 2.2: Area-averaged deviations in SST(^{o}C) and net surface SWs, LWs, LHFs, and SHFs (W/m^{-2}) for the Higher Andes minus Control run. Fluxes are positive into the ocean. See text for the location of the boxes.

Box	ΔSST	ΔSW	ΔLW	ΔLHF	ΔSHF
1	-0.63	15.16	-4.13	-10.64	-0.24
2	-0.77	-0.02	-2.1	3.97	-0.58
3	-1.01	21.43	-8.02	-11.73	-0.51
4	-1.77	-16.23	4.62	13.61	-0.59

However, the change in cloud fraction is more likely to be a feedback of the change in the SST instead of directly causing SST change [Takahashi and Battisti, 2007a]. Thus, it is necessary to diagnose what would be the most initial change that is made by the modification of the Andes topography. Following Takahashi and Battisti [2007a], we used the same equation as

$$\Delta T = \alpha_r(-\frac{\Delta U}{U_r} + \frac{1}{1+B_r}\frac{\Delta q}{q_{sr}-q_r} + \frac{B_r}{1+B_r}\frac{\Delta T_a}{T_r - T_{ar}} - \frac{\Delta F}{(1+B_r)LHF_r}) \qquad (2.1)$$

In which,

$$\alpha_r = (1+B_r)[\frac{\gamma}{LHF_r} + \frac{1}{q_{sr}-q_r}(\frac{\partial q_s}{\partial T})_r + \frac{B_r}{T_r - T_{ar}}]^{-1} \qquad (2.2)$$

and B is the Bowen Ratio that equals to SHF/LHF and the subscript r indicates the control case. U is the surface wind speed, q is the specific humidity near the surface and q_s is the near-surface saturation specific humidity. T is SST and T_a is near-surface air temperature. ΔF is the extra radiative forcing.

The four terms in Table 2.3 represents the change in SST due to the change in surface wind speed (U term), specific humidity (q term), surface air temperature (T term) and radiative fluxes (F term). Here, change in shortwave radiation is only considered as a feedback, and ΔF is estimated as a change in longwave radiative forcing on the SST due to the change in upper-troposphere humidity with the elevation of the Andes [Takahashi and Battisti, 2007a]. To know the relative importance from the change in these parameters, we are only comparing these four terms inside the parentheses. Table 2.3 shows the values of these four terms in the box shown in Fig.2.2.

It is clear that in the central and Eastern Pacific region (Box 2-4), the most important contribution to the decrease of SST comes from the decrease of specific humidity (q) term. This implies that in the equatorial Eastern Pacific, the central South Pacific and Southeast Pacific area, the lowered SST in the Higher Andes run results from

Table 2.3: Area-averaged relative contributions to SST changes, through latent and sensible heat fluxes, by changes in surface wind speed (U term), in specific humidity (q term), in surface air temperature (T_a term), and by changes in longwave radiative fluxes (F term).

Box	U term	q term	T_a term	F term
1	-0.16	-0.17	-0.02	-0.03
2	0.04	-0.26	-0.02	-0.02
3	-0.10	-0.33	-0.04	-0.05
4	-0.04	-0.31	-0.09	0.03

the drying effect associated with the lifting of the Andes. The strengthening of the anticyclonic motion brings the dry air from upper atmosphere and induces stronger evaporation over the entire South Pacific. However, when SST decreases, the saturation vapor pressure will decrease according to the Clausius-Clayperon equation. This reduction in specific humidity is the strongest negative feedback that prevents evaporation. Even though we are not considering the change in the shortwave radiation as the force in the equation that initiates the lowering of the SST, it is the major feedback that enhances the cooling. The colder sea surface temperature induces the formation of low-level clouds by turbulent mixing in the atmospheric boundary layer [Schneider et al., 2019]. The low-level clouds blocking the insolation is the most important factor that enhances this cooling effect and further lowers the SST [Takahashi and Battisti, 2007a]. In the tropical Western Pacific region represented by Box 1, the increase of near-surface wind speed and the drying effect play similarly important roles in the decrease of the SST. In all the four boxes, longwave radiative effect (F) term is relatively smaller than the other terms, implying that the change in the longwave radiation is not an important original cause of the lowered SST.

2.3.2 Change in Precipitation

In the control run (Fig. 2.5b), the SPCZ is much stronger and parallel to the equator compared with observations (Fig. 2.5a), and it covers the area from 120°E to 120°W. The control run fails to predict the strength and the location of precipitation observed over the South Pacific (Fig. 2.5d). The SPCZ shifts northeastward and is much stronger in the control run than in the observation. As a result, the cold tongue only extends to 120°W in the South Pacific, and the dry band at the equatorial Eastern Pacific is too narrow.

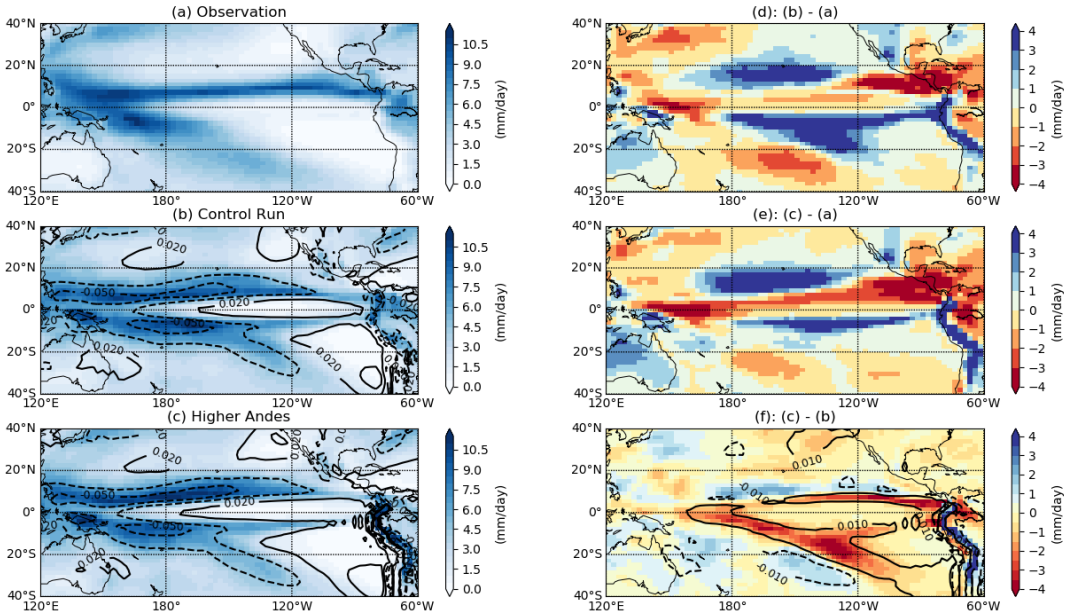

Figure 2.5: Left panel: Color: Annual mean precipitation from TRMM (a), control CESM (b), and higher Andes CESM (c). Right panel: Precipitation difference between control and MODIS (d), High Andes and MODIS (e), and High Andes minus control (f) Contour: vertical velocity at 500 hPa (pa/s), with solid lines as positive values (descending motion) and dashed lines as negative values (ascending motion).

When we increase the height of the Andes, the narrow, dry band at the equatorial Eastern Pacific strengthens and extends westward, and the triangular dry region in the Southeast Pacific extends to 140°W (Fig. 2.5c). The location of the SPCZ is closer to the observation in the Higher Andes run (Fig. 2.5e), and the strong precipitation bias in the central South Pacific is somewhat eliminated. The model results indicate

that the higher elevation setting in the Andes can provide a better simulation of the dry zone in the Southeast Pacific. The change in precipitation over other ocean basins are not as significant (Fig. S3).

The RMSE is also calculated for precipitation with reference to the TRMM data (Table 2.4). The RMSE for the tropical South Pacific has significantly reduced (by 29.2%). Even though the RMSE is slightly increased in the tropical North Pacific, the RMSE for the entire tropical Pacific is still reduced by 9.29%. It proves that the simulation of the tropical Pacific precipitation is getting better with the Higher Andes setting.

Table 2.4: Root Mean Square Error (RMSE) for precipitation. Tropical Pacific is the ocean region from 120^{o}E to 60 ^{o}W, 40^{o}S to 40^{o}N.

Precipitation RMSE (mm/day)	Tropical	NH Tropical	SH Tropical
Control	1.83	1.70	1.95
Higher Andes	1.66	1.89	1.38

The vertical motion at 500 hPa is shown in the line contours in Fig. 2.5. The descending motion is coupled with divergence and the ascending motion is coupled with convergence. Because of the westward propagation of the convergence center in the Higher Andes run, the descent motion in the mid-latitude Southeast Pacific is enhanced (Fig. 2.5f) along with the enhancement of equatorward wind (Fig. 2.3c). This is because when air flow is blocked by the higher Andes, the mid-latitude westerly wind will be redirected towards the equator. This equatorward motion not only brings cold and dry air from higher latitudes, but also descends as a result of the conservation of potential vorticity. This descent motion inhibits convection in the Southeast Pacific, resulting in a reduction in precipitation over the South Pacific Ocean.

2.3.3 Regional Averaged Pattern

Fig. 2.6 shows the regional distribution of SST and precipitation. In the zonal distribution of SST over the South Pacific (Fig. 2.6a), the modeled SSTs are higher than the observed SSTs across the whole Pacific basin, with a smaller bias in the Western Pacific and a larger bias in the Eastern Pacific. In the Eastern Pacific, the modeled SST is 3°C higher than the observation, demonstrating that the simulated Southeast Pacific cold tongue is too weak. With the higher elevation of the Andes, the Eastern Pacific SSTs become similar to the observation. In the Western Pacific, however, the SST bias in the Higher Andes case is 0.8°C, somewhat higher than the control run (0.6°C).

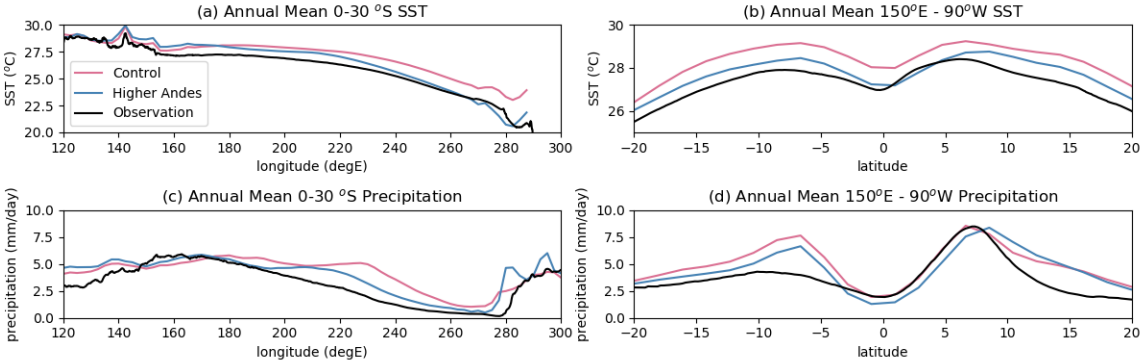

Figure 2.6: Zonal (a, c) and meridional (b, d) distribution of annual mean SST (a, b) and precipitation (c, d). SST is calculated only over the ocean area, and precipitation includes both land and ocean.

In the meridional distribution of the SST (Fig 2.6b), the SSTs in control run are about 1°C higher than observation throughout the whole tropical area. With the higher Andes, this difference has been reduced by half, and the results are more similar to the observation, particularly near the equator. This improvement is related to the reduction of incoming solar radiation at the surface due to the increase in low clouds and the increased surface evaporative cooling induced by the stronger winds.

Fig. 2.6c shows the zonal distribution of precipitation in the SH tropical region in the Pacific area. In observation, precipitation decreases almost linearly from west to

east in 160°E to 90°W. However, in the control run, the precipitation values are high from 180°E to 130°W with a peak at 130°W, where simulated precipitation is twice as high as the observation. With the higher Andes, precipitation over the central Pacific Ocean decreases from 5 mm/day to 3.5 mm/day. Although it is still higher than the observation, precipitation peak shifts westward to 150°W and is weakened. The higher elevation in South America deflects the mid latitude wind to turn counterclockwise, inhibiting precipitation off its west coast and enlarges the dry and cold area, resulting in the westward migration of precipitation center.

Fig. 2.6d is the meridional distribution of precipitation over the Pacific region. The observations show a large contrast of precipitation between the North and South Pacific. However, both Control and Higher Andes runs clearly show obvious double precipitation centers on both hemispheres. Results from the Control run are similar to the observed values from 2°S to 8°N, but are highly overestimated in the SH. Results from the Higher Andes case exhibit a slight decrease of precipitation over the region from 20°S to 9°N, but the precipitation values near the equator and in the Northern Pacific are underestimated.

To understand how the elevation of the Andes changes the east-west circulation over the Pacific, we calculate the stream function of divergent component of zonal wind over equatorial Pacific (Fig. 2.7). The result shows that the Walker Circulation is strengthened with the higher elevation of Andes. This result agrees well with the improved east-west temperature gradient and the larger cold tongue area.

2.3.4 Sensitivity Test and Energy Budget Analysis

To obtain more insight on how the elevation of the Andes affects the climate over the Southeast Pacific Ocean, we performed a series of sensitivity tests. In the area outlined by red lines in South America (Fig. 2.1c), we set the elevation to 50 m (indicated as the 'No Andes' in the following sections), 1km, 2 km, 3 km, 4 km, 5 km

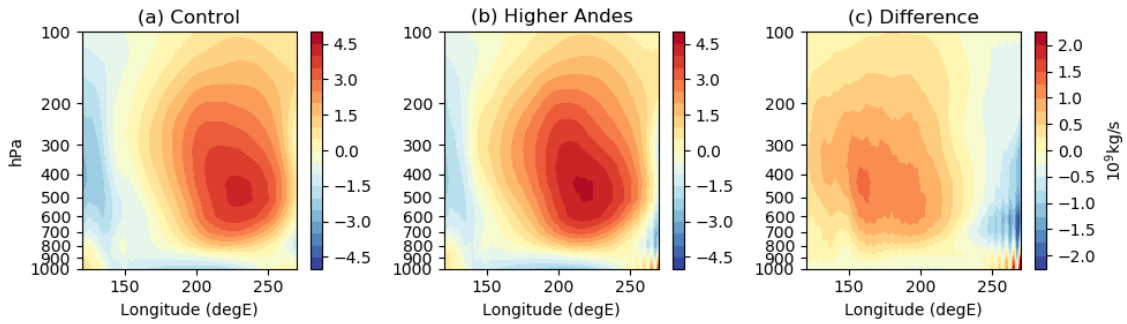

Figure 2.7: Stream function of divergent component of zonal wind averaged over 5^oS to 5^oN over Pacific region. Stream function is calculated as $\Psi = a\Delta\phi \int_0^p u_D dp/g$ as Yu et al. [2012]. Because the Walker circulation and the Hadley circulation are interconnected, the change in the vertical motion can result from both the zonal and meridional circulation. Therefore, we use the Ψ-vector method of Keyser et al. [1989] to partition the irrotational part of the three-dimensional flow into a pair of orthogonal two-dimensional circulations.

and 6 km.

Fig. 2.8 presents the zonal and meridional distributions of SST and precipitation of the cases with different heights of the Andes. In the SST zonal distribution (Fig. 2.8a), the SSTs do not show an apparent difference with different heights of the Andes on the Western Pacific at the longitude from 160°E to 170°W. The differences in SSTs increase eastward. By changing the elevation in the Andes area from 50 m to 6 km, the differences in SSTs over the Southeast Pacific can be as large as 7°C. In the SST meridional distribution, with the increasing height of the Andes (Fig. 2.8b), the overall tropical SSTs over the Pacific basin decrease, and the greatest change occurs at around 7°S. The decrease of SST over the NH is much weaker than the SH, resulting in a meridional asymmetry SST pattern over the Pacific Ocean.

Similar to SST change, in the zonal precipitation distribution (Fig. 2.8c), as the height of the Andes increases, the precipitation in the Western Pacific does not change. However, from 160°E to 90°W, it decreases almost linearly to the east. With lower elevations of the Andes, precipitation peaks at 130°W over the South Pacific. With the increasing elevation of the Andes, this precipitation peak is lowered and migrates

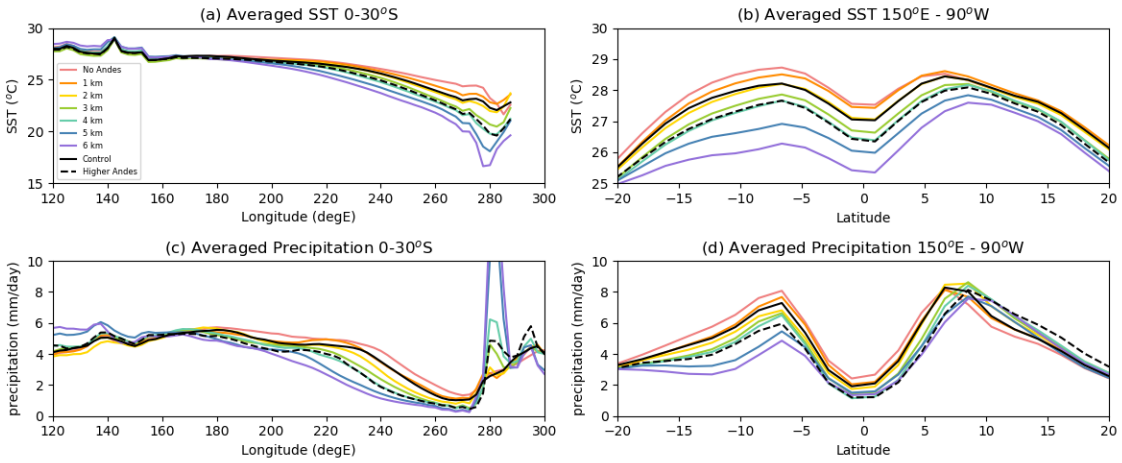

Figure 2.8: Sensitivity test for the height of Andes and SST (a), (b); sensitivity test for the height of Andes and precipitation (c), (d).

westward. When the elevation is as high as 5 km or 6 km, the precipitation pattern is very similar to the observation, although this elevation is unrealistic. However, we can still conclude that the Andes with higher elevation does a better job in inhibiting precipitation over the east and central South Pacific. In the meridional precipitation distribution (Fig. 2.8d), when the Andes is removed, the precipitation pattern is very symmetric about the equator and shows the double ITCZs. The increasing elevation of the Andes significantly decreases the precipitation in the SH, while it only decreases the precipitation in the North Pacific by a small amount. As a result, the north-south precipitation difference increases. With the increasing elevation of the Andes, there is less precipitation along the equator, consistent with the low SST and increasing amount of low-level clouds.

The Control Run (solid black lines) model results show a similar distribution as the case with a 2 km elevation of the Andes, while the Higher Andes Run (dashed black lines) results show a distribution similar to the case of 4 km. These results suggest that 2 km and 4 km are the effective heights of the Andes in the Control and the Higher Andes cases. This explains why in the Control run, the height of the Andes is not enough to block the zonal winds.

To have a more straightforward comparison for the sensitivity test results, we plotted Fig. 2.9 as another interpretation for Fig. 2.6 and Fig. 2.8. From the sensitivity test (grey line), the SST over all the areas in the Pacific, and the precipitation over the South Pacific (Fig. 2.9a-g shows a decreasing trend with the increasing height of the Andes. The Control run (red line) overestimates the SST for all regions over the Pacific compared with the observation (black line), and also overestimates the precipitation except for the Southwest Pacific. In the Higher Andes case (blue line), the simulation result approaches the observation obviously in the SST and precipitation over the Southeast Pacific and the South Central Pacific. Although there is slight increase of biases in the Southwest Pacific SST and the North Central Pacific precipitation, and the Southwest Pacific precipitation barely changes with the Higher Andes setting, this modification can be still considered effective.

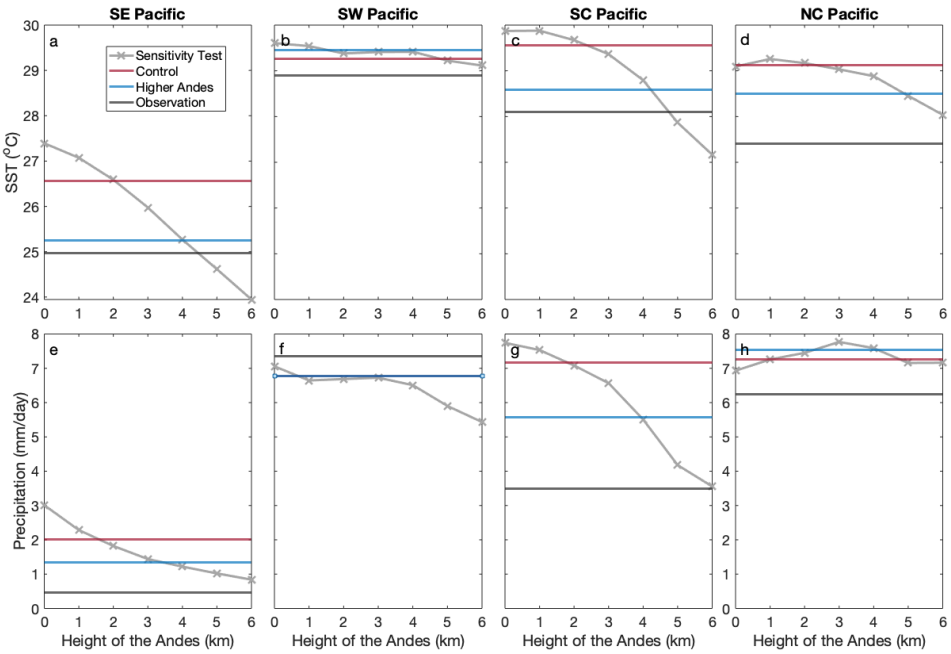

Figure 2.9: Sensitivity test comparison and results. (a)-(d): Comparison for SST. (e)-(h): Comparison for precipitation. (a),(e): Change in the Southeast (SE) Pacific, 0^o-20^oS, 100^oW-120^oW. (b),(f): Change in the Southwest (SW) Pacific, 0-20^oS,160^oE-180^o. (c),(g): Change in the South Central (SC) Pacific, 5^oS-15^oS, 180^o-120^oW. (d),(h): Change in the North Central (NC) Pacific, 5^oN-15^oN, 180^o-120^oW.

It is also worth noted that the observation values for precipitation do not fall on the sensitivity test lines at all in the precipitation figures (Fig 2.9e-h). This indicates changing the height of the Andes can not entirely solve the precipitation biases in the CESM. This precipitation bias, which is related to the ITCZ problem, is a result of atmospheric net energy input biases near the equator and the cross-equatorial divergent atmospheric energy transport [Adam et al., 2018, Xiang et al., 2017].

To have a further insight into this problem, we analyze meridional energy transport in the atmosphere (Fig. 2.10), a factor that is shown to be closely related to the location of the ITCZs [Bischoff and Schneider, 2016]. Adam et al. [2018] suggested that ITCZs are located further south compared with the observation, and this bias in the ITCZ is related to the atmospheric energy budget. They suggest that the southward shift of the ITCZ is related to either too much energy absorption in the Southern Hemisphere or too little energy absorption in the Northern Hemisphere. Here, we used the Energy Flux Equator (EFE), a latitude where northward energy flux becomes zero, to indicate the location of the ITCZ. EKE shifts northward as the elevation of the Andes increases, and all the cases show positive slope and a single intersection at the zero line (Fig. 2.10a). Fig. 2.10b shows that more energy is transported by the atmosphere from NH to SH with higher Andes, and the observation value is consistent with the model result when the height of the Andes is between 5km and 6km. These two figures indicate that with the increasing elevation of the Andes, the global mean ITCZ migrates northward. Since the Andes is an important factor that shapes the north-south ITCZ asymmetry [Takahashi and Battisti, 2007a], correcting the effective height of the Andes is necessary to improve the global energy budget and large scale circulation.

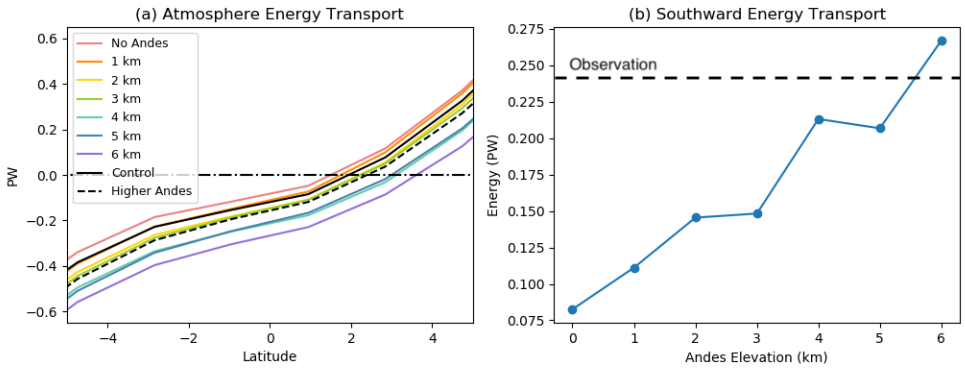

Figure 2.10: (a) Northward Atmospheric Energy Transport (AET) near the equator. (b) Cross-equator southward energy transport.

2.4 Summary and Conclusion

Eastern Pacific climate has an important regional and global influence [Collins et al., 2010]. However, climate models have difficulty in simulating the cold tongue off the west coast of South America. For example, compared with observations, CESM overestimates temperature and precipitation in the Southeast Pacific region [Bogenschutz et al., 2018].

In this study, using the CESM slab ocean model, we showed that the smoothed topography in South America will influence the model's simulation for precipitation and SST over the Southeast Pacific. The Andes is a narrow mountain range, and in low-resolution models, its elevation is too smoothed that it cannot efficiently block zonal winds. When we modified the elevation so that the mid-latitude westerly wind is blocked and turns equatorward while descending, the anticyclonic motion in the South Pacific is strengthened, increasing the amount of low-level clouds and surface evaporation. As a result, the precipitation in the South Pacific is inhibited and the SST in the Southeast Pacific is decreased.

Our sensitivity test results show that with the increasing elevation of the Andes, the east-west SST difference in tropical South Pacific increases, and the tropical Pacific SSTs decrease. Precipitation in the tropical South Pacific also decreases,

and the precipitation peak is propagating westwards from the central South Pacific to the Western Pacific. The result also shows that the southward cross-equatorial atmospheric energy transport increases with the increasing elevation of the Andes, indicating a larger NH-SH energy imbalance, closer to the observation. Our results indicate that the control topography setting of the Andes in the CESM model with resolution of $1.9^\circ \times 2.5^\circ$ has an effective height of 2 km; the modified Andes has an effective height of 4 km.

It has been shown that the higher resolution climate model can significantly improve the mean climate simulation. Small et al. [2014] showed that a 0.25° resolution climate model can simulate the Southeast Pacific cold tongue better than a low resolution model. The major reason is that a better resolved orography will simulate a more accurate atmospheric flow. Adcroft [2013] considered the representation for topography as impermeable walls and porous barriers, and his results approximately simulated for the key features for lateral transport. His study provides a possible solution to fix the bias in a low-resolution global climate model.

With a better simulation of the mean tropical Pacific climate, we expect that the ENSO simulation will be improved, as well as the future projection of the global climate. However, the role of the ocean has not been tested in this work and there are still some biases in the NH that may be related to the representation of the topography in a low-resolution model. In the future, we hope to examine the role of the ocean with a fully-coupled global climate model.

Chapter 3

The Andes affect ENSO statistics

3.1 Introduction

The tropical Pacific climate is formed by the large-scale interaction between the atmosphere and the ocean. Its mean state has strong contrast between the wet and warm western Pacific and the cold and dry eastern Pacific. Deviating from this mean state, the tropical Pacific climate has a natural interannual variation called El Niño/Southern Oscillation (ENSO, see McPhaden et al. [2020] for a review). ENSO events alter the global atmospheric circulation, causing unusual floods or droughts occur in many regions [e.g., Prieto, 2007], creating threats to our society in many aspects including agriculture [Nicholls, 1991], fisheries [Lehodey et al., 2020], public safety [Fang et al., 2021], and economic vitality [Bastianin et al., 2018].

Due to ENSO's impacts, understanding its dynamics and predicting it a few seasons in advance has been the focus of intensive research over the last 50 years. Early methods built simplified models to simulate the components that affect ENSO's initiation, generation and dissipation [e.g. Bjerknes, 1969, Wyrtki, 1985, Cane and Zebiak, 1985, Jin, 1996, 1997a,b]. These simplified climate models do simulate a quasi-periodic signal and reveal some of the key components of the ENSO cycle, but many important aspects of ENSO are not accounted for. With the lack of seasonal modulation and the non-linear processes in these simplified models, they are too limited in scope and cannot reproduce the full complexity and diversity of ENSO [Jin et al., 2020, Levine et al., 2016]. Coupled Global Circulation Models (CGCMs) are better suited to capture many characteristics of ENSO compared with simplified models, but they still have a lot of systematic errors [Guilyardi et al., 2009, Bellenger et al., 2014, Guilyardi et al., 2020, Planton et al., 2021], including biases in the mean state, in processes contributing to the growth and decay of ENSO and occurrence statistics. Biases in the mean state include the SST distribution, double Inter-Tropical Convergence Zones (ITCZs) bias, and the errors in surface wind simulation [e.g., Guilyardi et al., 2020, Planton et al., 2021]. Biases in ENSO properties include the wrong

amplitude, too sharply peaked power spectrum, excess westward displacement of the ENSO pattern, too little skewness and so on [e.g., Guilyardi et al., 2020, Planton et al., 2021]. In addition, there are still considerable uncertainties in ENSO properties under warmer climate, although climate models are improving in the agreement of future projections [Cai et al., 2018, 2021].

Progress in overcoming these difficulties has taken many forms. One solution is increasing the spatial and temporal resolutions of the atmosphere and ocean models [Wittenberg et al., 2018]. However, it is a slow and challenging process to reach higher resolution model simulations, since each increase in resolution is exponentially more difficult. Fox-Kemper et al. [2014] showed that the past decades' rate of computational improvement results in the doubling of full-complexity CGCM resolution only every 10.2 years [consistent with a recent update by Haine et al., 2021]. Therefore, instead of using a higher-resolution climate model, we attempt to improve ENSO simulations by better representing dynamical processes.

As many errors in ENSO properties and errors in the mean state climate are closely connected [e.g., Zhang and Sun, 2014, Abellán et al., 2017, He et al., 2018], adjustments that can improve the mean state simulations may also improve the ENSO simulation. The mean state over the Pacific can be influenced by many aspects of the modeling system, but the focus in this paper is the representation of the Andes. Previous studies showed that removing all orography in a CGCM modulates the mean states and ENSO has a stronger amplitude and increased regularity [Kitoh, 2007, Naiman et al., 2017]. As the Andes alone are important for the formation of the southeast Pacific cold tongue [Takahashi and Battisti, 2007a], Xu and Lee [2021] hypothesized that the Andes are not high enough in the low-resolution CGCMs and improving that could improve the simulation of the Pacific mean state and variability. Indeed, with too low Andes, the modeled range insufficiently modulates the atmospheric circulation and result in too warm SST in the southeast Pacific and too

much precipitation over the south Pacific. To test this hypothesis, Xu and Lee [2021] modified the Andes in a coupled system with a slab-ocean model and compared the experiment with a higher elevation of the Andes model versus a control experiment with the standard coarsened Andes orography. They found an improvement in the simulation of the tropical Pacific mean state with lowered SST in the southeast Pacific cold tongue and the inhibition of precipitation over the central south Pacific. We hypothesize that modifying the Andes will affect ENSO as well.

In this paper, we explore whether modification of the Andes can improve simulations of the mean state climate and the ENSO cycle in the tropical Pacific using a CGCM, focusing on the role of upper ocean dynamical feedbacks. Section 2 introduces the experimental setup and the model setting. Section 3 and 4 compare the model results in terms of the mean state and ENSO cycle. Section 5 discusses the mechanism explanations of our result and Section 6 talks about its scientific importance.

3.2 Method

3.2.1 Model and Experiment

We used the National Center for Atmospheric Research (NCAR) Community Earth System Model (CESM) version 1.2.2 [Hurrell et al., 2013]. It includes the Community Atmospheric Model, version 4 (CAM4) as the atmosphere component, and an extension of the Parallel Ocean Program (POP) Version 2 from Los Alamos National Laboratory (LANL) as the ocean component. We ran the model with CO_2 concentration as in year 2000 (367 ppm) so that we can compare our result with the satellite data. We used the atmospheric resolution of $1.9° \times 2.5\,°$ with 26 vertical layers and nominal oceanic resolution of $1°$ with 60 vertical layers for our experiment.

Boos and Kuang [2010] showed that the narrow Himalayas mountain ranges, rather than the Tibetan plateau, is essential to modulate the South Asian monsoon. Inspired

by their study, we consider the Andes as a similar barrier that influences the topical Pacific circulations. Fig. 3.1a shows the 1-km high-resolution topography from the National Oceanic and Atmospheric Administration (NOAA) National Geophysical Data Center (NGDC) Global Land One-km Base Elevation (GLOBE) topography, and Fig 3.1b is the default topography setting in CESM (used in our control experiment). In order to understand the influence from the Andes, we modified the height of the Andes to the highest value according to the GLOBE topography (Fig. 3.1c; experiment called 'Higher Andes'). In each coarse-grained grid cell along the Andes in the climate model, we computed its elevation as the maximal elevation within the cell area of the fine-grained observations. Our approach is to evaluate the maximum possible influence of the Andes, and not to simulate the exact influence of the Andes. Both experiments were run for 350 years to allow the upper ocean to adjust to the modification, and we used the last 160 years of model output for our analysis.

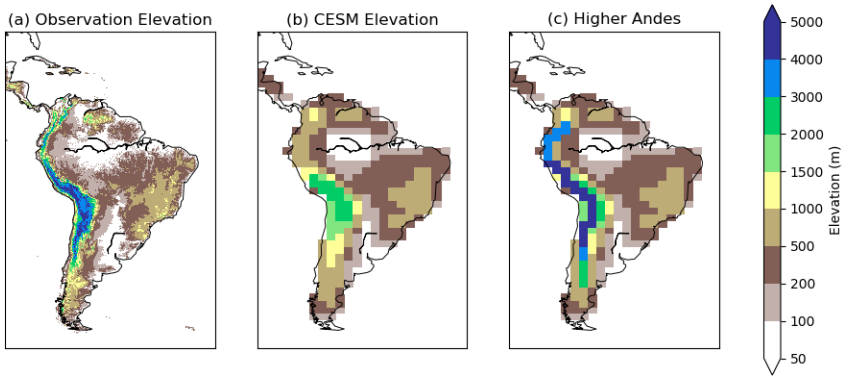

Figure 3.1: Elevation in South America from (a) National Oceanic and Atmospheric Administration (NOAA) National Geophysical Data Center (NGDC) Global Land One-km Base Elevation (GLOBE) topography, (b) 1.9° × 2.5° resolution of CESM Control experiment topography, and (c) Higher Andes experiment topography. The height of the Andes is adjusted to the highest value according to the GLOBE topography: in each coarse-grained grid cell along the Andes in the climate model, we computed its elevation as the maximal elevation within the cell area of the fine-grained observations. Same as Fig. 1 in Xu and Lee [2021].

3.2.2 Analysis

To analyze the model performance, we used the ENSO metrics package developed by the International Climate and Ocean: Variability, Predictability and Change (CLIVAR) Pacific Region Panel [Planton et al., 2021]. These metrics allow us to rapidly diagnose and evaluate the model's performance regarding the ENSO-related mean state and properties, teleconnection pattern, and dynamical coupling. In this research, we will focus on the comparison of the simulation accuracy between the Control and Higher Andes experiments.

To evaluate the model's performance on the tropical Pacific climate, we use HadISST's SST [Rayner et al., 2003], GPCPv2.3's precipitation [Adler et al., 2003], TropFlux's net surface heat fluxes and surface wind stress [Praveen Kumar et al., 2012, 2013], and the Met Office Hadley Centre's EN4 ocean temperature profile [Good et al., 2013]. We use monthly data from these products over the period 1979 to 2018. Although the CO_2 forcing within this period is not constant as in the model, it increases linearly with the average value approximately equal to that in year 2000. Therefore we still consider it a fair comparison.

To compare the spatial distributions between the observations and the simulations, all data is interpolated onto a regular $1^\circ \times 1^\circ$ grid. The gridded observational datasets available are not perfect and choosing another group of datasets may slightly change the metric values [e.g., Planton et al., 2021]. Using these observational datasets we do not precisely evaluate the model, but merely detect the differences between the Control and Higher Andes experiments and estimate if the new simulation is getting better or worse.

In the evaluation of the mean state distribution (Fig. 3.2, 3.4, 3.5), the model mean distributions are calculated from averaging the 160 year model results. In order to make comparisons with the 40 years observation data, the error bars are calculated using the bootstrapping method. We did 10,000 bootstrapping samples each selecting

480 months of data (i.e., 40 years) and calculated the average distribution of each sample. The error bars are calculated as the standard deviation over the 10,000 40-year-equivalent averages. The distribution of the 10,000 averages is nearly Gaussian, so the standard deviation is an adequate measure of uncertainty.

For the ENSO variations section (Fig. 3.7, 3.8, 3.10), unlike the mean state uncertainties, the ENSO variations are interannual signals continuous in time. Their spectral analysis is most meaningful within a continuous decadal-scale period matching in duration to the available observational data. Thus, the 160 years of model results are divided into 4 non-overlapping sections of 40 continuous years. Corresponding distributions of each section are plotted as the thin, light lines, and the averaged values of the 4 sections are plotted as the thick, dark lines. Root-Mean Square Errors (RMSEs) are calculated between the averaged distributions and the observations.

To quantify the processes that influence the ENSO variation, we calculated the Bjerknes stability index [Jin et al., 2006] with the same equation as Zhao and Fedorov [2020].

$$2I_{BJ} = -\alpha_s - \frac{<\overline{u}>}{L_x} - \frac{<-2y\overline{v}>}{L_y^2} - \frac{<\mathcal{H}(\overline{w})\overline{w}>}{H_m} + \mu_a\beta_u\Big\langle\frac{\partial\overline{T}}{\partial x}\Big\rangle + \mu_a\beta_w\Big\langle\frac{\partial\overline{T}}{\partial z}\Big\rangle + \mu_a\beta_h a_h\Big\langle\frac{\overline{w}}{H_m}\Big\rangle \tag{3.1}$$

The terms on the right hand side of this equation represent (1) Thermal Damping (TD), (2) the 2nd, 3rd, and 4th terms add up as the Mean Advection Damping (MA), (3) Zonal Advection Feedback (ZA), (4) Ekman Feedback (EK) and (5) Thermocline Feedback (TH). The first two mechanicms act as a damping effect on ENSO, while the remaining three feedback processes strengthen ENSO. This equation separates the different mechanisms that can influence the ENSO cycle, which allows us to understand what are key the processes that the Higher Andes experiment differs

from the control experiment.

3.3 Changes in the mean state

Similar to the slab-ocean model simulations [Xu and Lee, 2021], the Higher Andes in the atmosphere-ocean coupled model changes the mean state of the ocean and atmosphere. We will evaluate these changes in four aspects related to mean changes usually taken to affect ENSO: SST, precipitation, wind stress and ocean stratification.

3.3.1 SST and precipitation

Bayr et al. [2018] and Wengel et al. [2018] found a link between the mean SST bias and ENSO seasonality as well as the balance of mechanisms generating SST anomalies. As SST and precipitation biases are linked [e.g. Oueslati and Bellon, 2015, Brown et al., 2020], the effect of the height of the Andes on these biases are analyzed together in this section.

Figure 3.2 shows the latitudinal and longitudinal distribution of SST and precipitation in the Observation (black line), Control (red line) and Higher Andes experiments (blue line). In the eastern Pacific (Fig. 3.2a), the SST across latitudes is too warm in both experiments, but this warm bias is smaller in the Higher Andes experiment than in the Control experiment (RMSE of 0.6 °C and 1.2 °C respectively), especially south of the equator. As a consequence, the north-south (N-S) SST gradient (defined as the difference between the highest SST in the northern and southern hemisphere) is better reproduced in the Higher Andes experiment than in the Control experiment (Higher Andes: 1.4 °C; Control: 0.7 °C; observation: 1.5 °C). Both experiments are also too warm along the equator (Fig. 3.2b), but again, the bias is reduced in the Higher Andes experiment compared to the Control experiment (RMSE of 0.5 °C and 0.8 °C respectively). Note that the bias is reduced everywhere but west of the

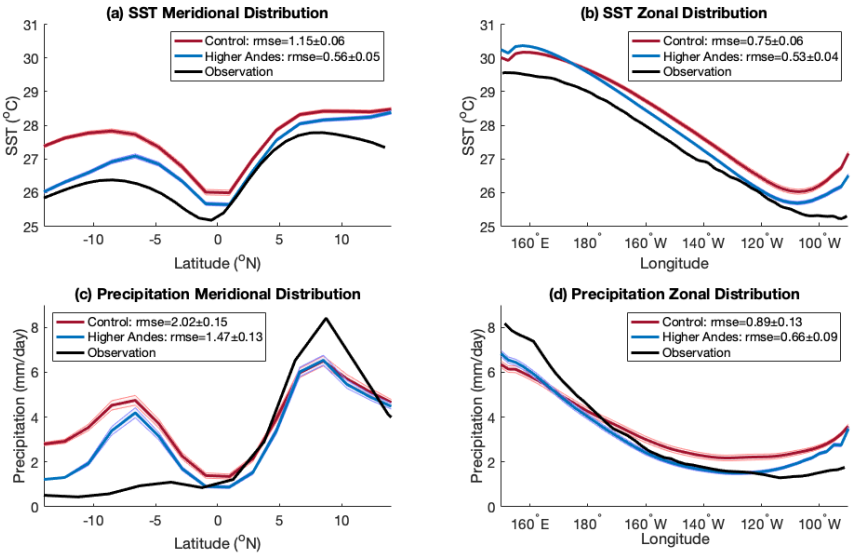

Figure 3.2: (a),(b) SST distribution in Observation, Control and Higher Andes experiments (°C). (c),(d) Precipitation distribution in Observation, Control and Higher Andes experiments (mm/day). (a),(c) are distributions across latitudes (zonal average 150°E-90°W). (b),(d) are distributions along the equator (meridional average 5°S-5°N). The solid lines in model results are the averaged distribution over 160 years. The error bars are calculated with the bootstrapping method. We did 10,000 times of bootstrapping with 480 months (40 years) of data, and calculated the average distribution of each bootstrapping samples. The error bars are the standard deviations of these 10,000 average distributions. The observation distributions (black lines) are the average distribution of 40 years. The legends also show the Root Mean Square Errors (RMSEs) calculated as the averaged difference between the model mean values (blue and red solid lines) and observations (black solid line). Uncertainties of the RMSEs are the averaged values of the error bars. See Method section for detailed explanations.

dateline.

In the tropical Pacific, the air from the southern and northern hemispheres converges. The converged air is forced upward and creates the intertropical convergence zone (ITCZ), a region of heavy precipitation, on average located at the north of the equator [Philander et al., 1996]. The observed precipitation distribution across latitudes in the eastern Pacific (Fig. 3.2c; black line) displays a strong N-S precipitation difference, with around 1 mm/day south of the equator and a peak reaching 8 mm/day around 7°N. In both experiments, the distribution of precipitation is too symmetric

with respect to the equator, a persistent error in climate models called the double ITCZs bias [e.g., Lin, 2007, Bellenger et al., 2014, Planton et al., 2021]. The section-averaged bias is around 2.0 mm/day in the Control experiment (red line), and N-S precipitation gradient (defined as the difference between the largest precipitation in the northern and southern hemisphere) is around 2.1 mm/day. In the Higher Andes experiment, the double ITCZ bias is still present but reduced (the N-S precipitation difference of 2.4 mm/day), slightly reducing the mean bias (1.5 mm/day). However, increasing the height of the Andes does not improve the dry bias in the western equatorial Pacific, as shown in Fig. 3.2d. But it inhibits central and eastern tropical Pacific precipitation and still reduces the total precipitation bias (RMSE of 0.9 mm/day in the Control experiment and of 0.7 mm/day in the Higher Andes experiment).

The changes brought by the modification of the Andes are similar in the present experiment with a fully-coupled climate model and in the experiment from Xu and Lee [2021] with a slab ocean model (Fig. 3.3): a higher elevation of the Andes setting lowers the SST and reduces precipitation over the eastern tropical Pacific area. However, the difference between the Control and the Higher Andes experiments is smaller in the fully-coupled climate model, which means that the ocean circulation feedbacks respond to withstand the changes in the atmosphere, and end up weakening the influence from the Andes.

3.3.2 Wind stress

The surface wind over the tropical Pacific is an important factor that influences the heat and moisture transport, controls the coastal upwelling, and contributes to the development of the ENSO cycle [McPhaden et al., 2020]. As both zonal and meridional wind stress modulate the amplitude of ENSO events [Hu and Fedorov, 2018, Zhao and Fedorov, 2020], we analyze their evolution between the two experiments in this section (Fig. 3.4).

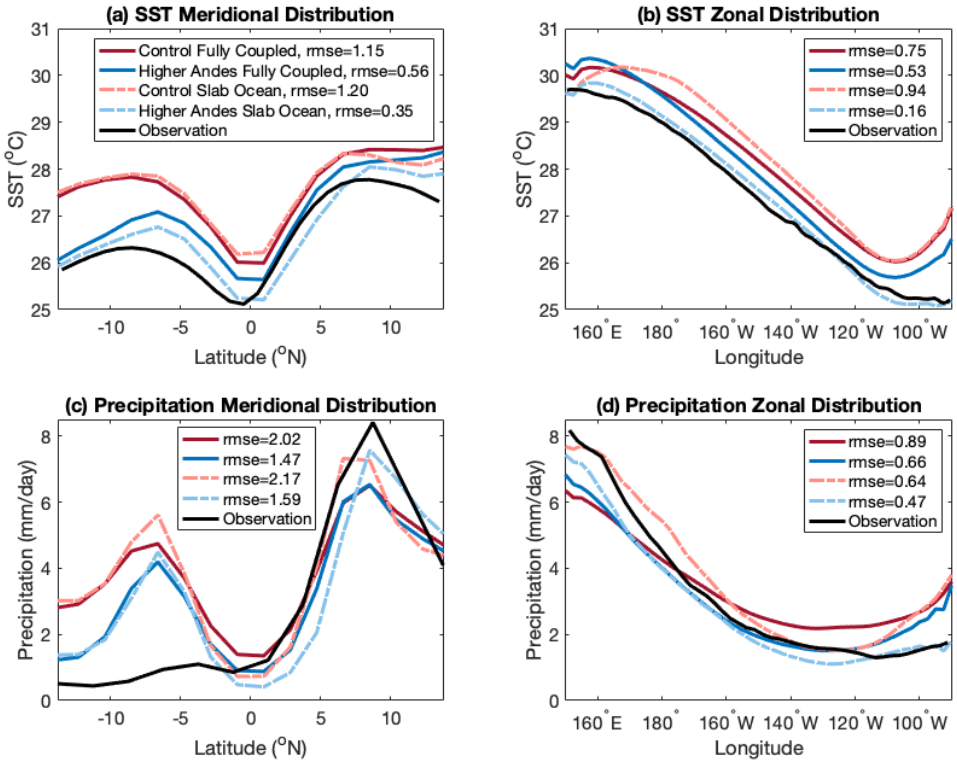

Figure 3.3: Similar to Fig. 3.2, but for the comparison between fully-coupled model results (thick solid lines) and slab-ocean model results (thin dashed lines). The modeled fully-coupled distributions are averaged over the last 160 years of 350 years simulations. The slab-ocean distributions are averaged over the last 10 years of 30 years simulations. Here we only showed the average distributions but not the error bars because the fully-coupled experiments and the slab-ocean experiments are run for different lengths compared with the observation. The legends also show the RMSEs calculated between the each modeled average values and observations.

The tropical Pacific region, zonal wind stress is, on average, from east to west along the equator in the Pacific. The meridional component is northward in the southern hemisphere and up to 7°N and southward in higher latitudes, to form the ITCZ (Fig. 3.4, black lines). This pattern is well reproduced in the Control experiment, but the cross-equatorial winds in the eastern equatorial Pacific are too weak (they reach 30×10^{-3} N m^{-2} in the observation, but only 12×10^{-3} N m^{-2} in the Control experiment; Fig. 3.4d).

With the Higher Andes experiment, zonal wind stress becomes stronger than in the

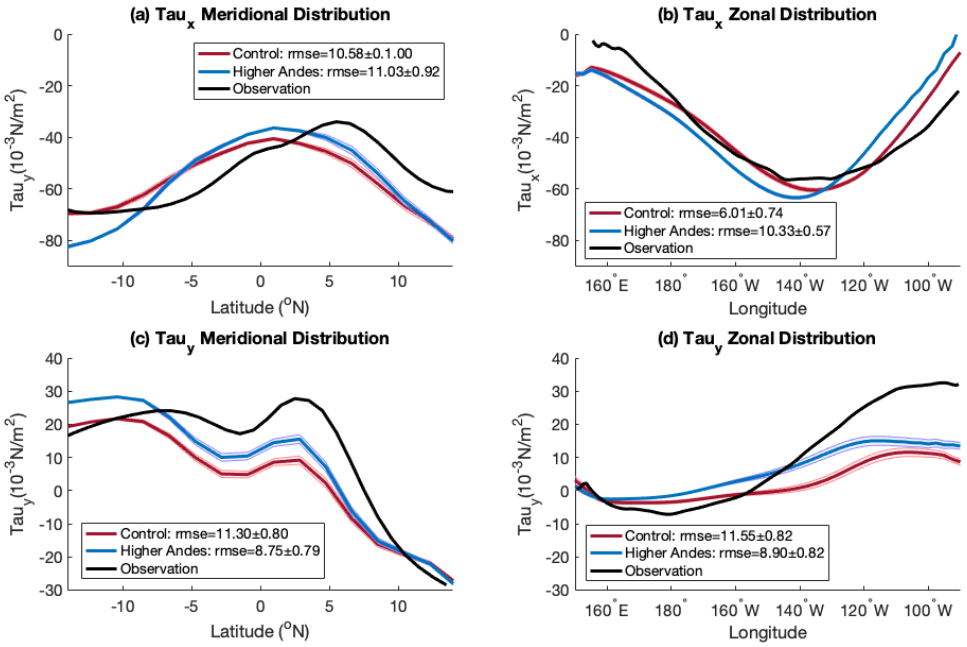

Figure 3.4: Same as Fig. 3.2, but for the zonal and meridional wind stress (10^{-3}N m^{-2}). In (a) and (c), zonal average is computed between 150°E and 270°E.

Control experiment and observations in the south Pacific (Fig. 3.4a) and in the central to western Pacific region (Fig. 3.4b), and becomes weaker in the eastern Pacific region (Fig. 3.4b). As a consequence, the zonal wind stress biases are slightly larger in the Higher Andes experiment than in the Control experiment, across latitudes (4.5×10^{-3} N m^{-2} and 2.7×10^{-3} N m^{-2} respectively) and along the equator (11.0×10^{-3} N m^{-2} and 6.7×10^{-3} N m^{-2} respectively). The meridional component does not change much across latitudes (Fig. 3.4c). It becomes slightly too strong south of 5°S in the Higher Andes experiment and gets closer to the observation in the equatorial band (5°S to 5°N). This does not change the mean bias much (from 4.7×10^{-3} N m^{-2} in the Control experiment to 3.0×10^{-3} N m^{-2} in the Higher Andes experiment). Along the equator (Fig. 3.4d), there is little change west of 200°E, but in the eastern equatorial Pacific, the cross-equatorial winds are strengthened in the Higher Andes experiment, getting closer to the observation (but still too weak). This bias is slightly improved but not by a lot (around 11.5×10^{-3} N m^{-2} in the Control experiment and around 8.9×10^{-3}

N m^{-2} in the Higher Andes experiment).

The modified atmospheric circulation is related to the change in SST. Similar to the slab ocean model results from Xu and Lee [2021] (Fig. 3.3), the Higher Andes experiment lowers the SST in the southeast Pacific by enhanced evaporative and radiative cooling [Xu and Lee, 2021]. The cooler SST in the south Pacific will enhance the high sea surface pressure in the subtropical south Pacific, and therefore enhance the anticyclonic motion [Takahashi and Battisti, 2007a]. This enhanced anticyclonic motion includes stronger easterly winds in the western equatorial Pacific (Fig.3.4b). Also, the colder SST in the south Pacific increases the surface pressure gradient in the south and the north Pacific, forming a stronger cross-equatorial wind from the southern hemisphere to the northern hemisphere (Fig.3.4c). In conclusion, imposing a higher elevation of the Andes induces stronger zonal and meridional wind stress in the tropical Pacific.

SST biases in different climate models are different [e.g. Fig.2 in Burls et al., 2017], but one common problem is that the east-west SST gradient in the climate models is too small. The biases are either a warm bias or a weaker cold bias in the eastern Pacific, indicating that the SST gradient in most of the CMIP5 models is not as strong as in the observations. Our experiment increases the east-west SST gradient by elevating the height of the Andes, and this change is accompanied by stronger winds over the tropical Pacific.

3.3.3 Ocean stratification

Because the Higher Andes setting changes the atmosphere circulation, the upper ocean would respond to this change and reach a new equilibrium. Here we show the upper ocean temperature distribution in the two experiments from years 191 to 350. An important aspect of the signal that develops into an ENSO event is the propagation of a temperature anomaly in the subsurface ocean, and it can be measured by the

change of thermocline depth [e.g., Zhao and Fedorov, 2020].

Fig. 3.5 shows the potential temperature distribution in NINO3 region (150°–90°W, 5°S–5°N) in both experiments and in the observations (left panel), as well as the differences between the model and the observations (right panel). The Higher Andes experiment is closer to the observations, being colder than the Control experiment in the upper 150 m and warmer than the Control experiment from 150 m to 300 m. As shown in Fig. 3.5, compared with the Higher Andes experiment, the Control experiment has a too large vertical temperature gradient in the NINO3 region, implying too strong stratification.

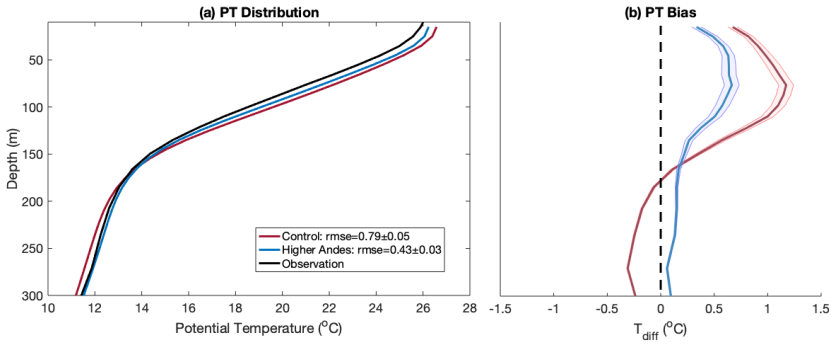

Figure 3.5: (a) Vertical distribution of the potential temperature (PT, °C) averaged over the NINO3 region (210-270°E, 5°S-5°N). (b) Biases of PT in the vertical distribution over the NINO3 region (model experiments minus observations). Error bars are calculated with a similar method as Fig. 3.2.

Fig. 3.6a,b show the vertical distribution and the change of potential temperature in the upper ocean of the equatorial Pacific. The thermocline in the Pacific ocean is tilted (black line in Fig 3.6a); it is deeper in the western Pacific and shallower in the eastern Pacific. A cooler potential temperature indicates a shallower thermocline, while a warmer potential temperature indicates a deeper thermocline. The Higher Andes experiment imposes a cooling in the eastern part of the thermocline, and a warming in the western part (Fig. 3.6b), indicating a shallower thermocline in the east and deeper in the west, resulting in a more zonal thermocline tilt.

However, this change in upper ocean potential temperature is not driven by

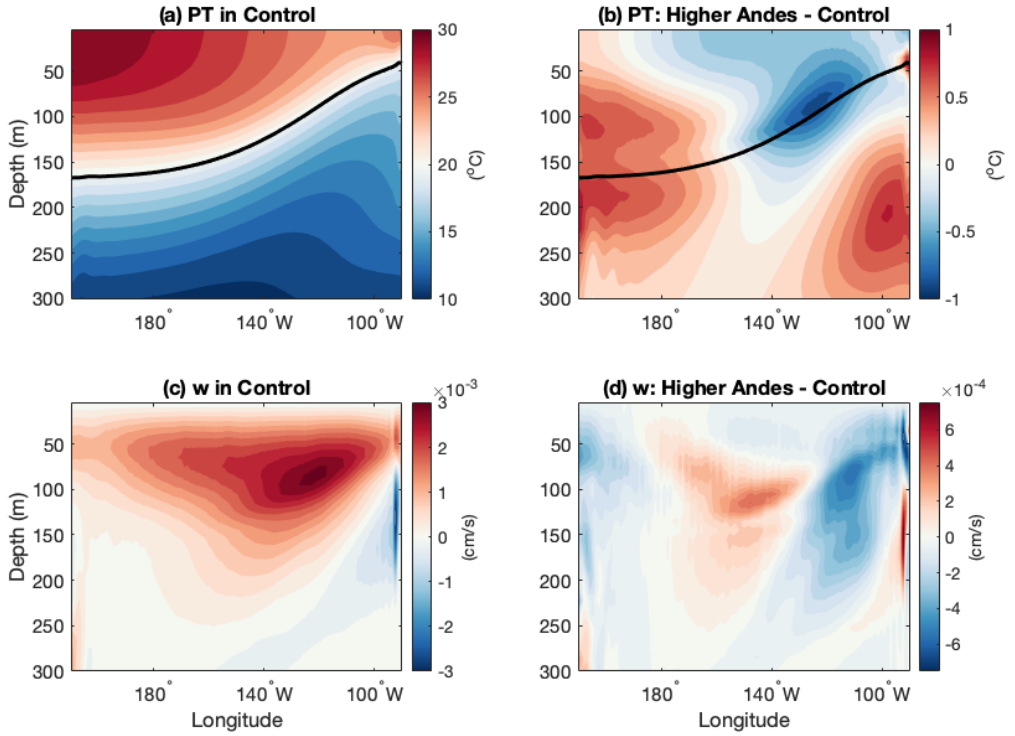

Figure 3.6: (a) Vertical PT distribution at the equator for Control experiment (°C)), the black line representing the depth of the 20°C isotherm (Z20). (b) PT distribution for Higher Andes minus Control (°C)), with the black line representing the same Z20 as in (a). (c) Vertical velocity (w, cm/s) for Control experiment.. (d) Vertical velocity (cm/s) for Higher Andes minus Control.

stronger coastal upwelling. In the eastern equatorial Pacific, the upper ocean is dominated by strong upward motion (Fig. 3.6c), but in the Higher Andes, upwelling weakens due to the weaker zonal wind stress in the eastern Pacific (Fig. 3.4b).

3.4 Changes in ENSO Properties

As the mean state climate over the tropical Pacific is thought to be related to the ENSO variability [Zhao and Fedorov, 2020], the modification of the Andes is expected to influence the ENSO cycle. The long-term changes in ocean mean state climate are the results of the changes in ENSO, as was suggested by Atwood et al. [2017]. In the periods during which ENSO has an unusually large amplitude, the mean state

climate will have cooler SSTs in the eastern Pacific and stronger precipitation in the western Pacific, which tends to damp ENSO variability. In fact, the changes in the mean state can affect the major feedbacks that control the characteristics of the ENSO cycle [Karamperidou et al., 2020]. Therefore, in this section, we will evaluate ENSO performance in the Higher Andes experiment from various characteristics of the ENSO cycle.

3.4.1 Amplitude

Fig. 3.7a shows the zonal distribution of the standard deviation (STD) of SST anomalies (SSTA) over the equatorial Pacific. The observation exhibits a small variability in the western Pacific region but from 190°E to the South American coast, the SSTA has a near-constant STD of about 0.9 °C. In the Control experiment, the SSTA STD is around 0.5 °C larger than observed all along the equator. The simulated SSTA variability also peaks clearly around 245°E before decreasing towards the South American coast. With the Higher Andes setting, the SSTA variability is decreased all over the equatorial Pacific, resulting in a similar amplitude of SSTA STD to the observation from 190°E to 240°E. The differences in the variability strength is consistent with changes in the NINO3 index probability distribution function (PDF) (Fig. 3.7b). In the Control experiment, extreme El Niño and La Niña events happen more frequently than the observations. But in the Higher Andes experiment, the distribution gets more concentrated to the center and the shape of its PDF is more similar to the observation. Although SSTA variability is still too high in the western equatorial Pacific and now has a too low variability in the far eastern Pacific in the Higher Andes experiment, its RMSE is still much smaller than the Control experiment. Overall, the Higher Andes experiment captures a much weaker SSTA variability over the equatorial Pacific compared with the Control experiment, more consistent with the observed variability.

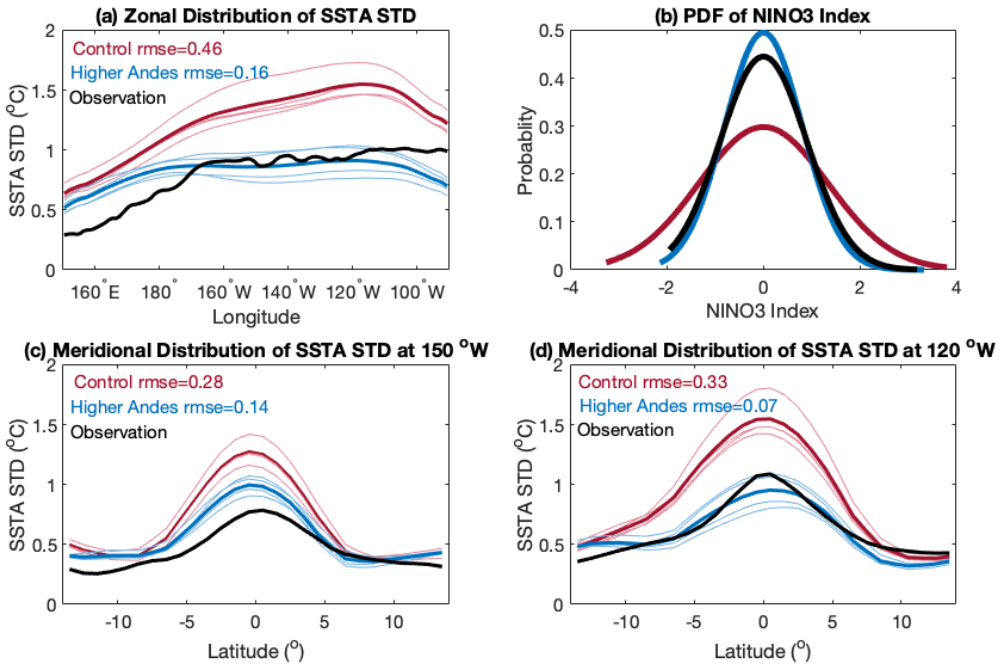

Figure 3.7: (a) Standard deviation (STD) of SST anomaly (SSTA) along the equator (°C; 5°S-5°N average). (b) Probability Distribution Function (PDF) of NINO3 index. (c),(d) meridional distribution of SSTA STD (°) at 150°W and 120°W. The 160 year model results are divided into 4 sections of 40 years. Distributions of each section are plotted as thin, light lines and the averaged values of the 4 non-overlapping sections are plotted as thick, dark lines. The legends also show RMSEs calculated between the averaged distributions and the observations. See Method section for detailed explanations.

Fig. 3.7c and d show the meridional SSTA STD distributions in the central (150°W) and eastern (240°E) Pacific. In the central Pacific, the Control SSTA variations are much stronger than the observation from the 5°S to 5°N region, with an error of 0.5 °C at the equator (66% stronger than the observation). By adjusting the Andes, the difference from the observation is reduced by more than a half and is now down to 0.2 °C larger than observed. In the eastern Pacific, the Control experiment has also a too large STD. With Higher Andes the STD is much reduced and the observation falls within uncertainties (blue shading in Fig. 3.7d). The comparison of the meridional distribution demonstrates that the Higher Andes experiment largely improves the SSTA variation errors near the equator.

In the NINO3 region, the Higher Andes experiment has slightly weaker SSTA STD (0.8 °C) compared to the observation (1.0 °C), while the Control experiment variation is about 50% stronger than the observation (1.5 °C). The distribution of SSTA in the NINO3 region is quite narrow in the observation, with 90% of the SSTA being moderate or neutral SSTA (NINO3 SSTA between -1.5 °C and +1.5 °C). The distribution in the Control experiment is too spread out, with only 72% of moderate or neutral SSTA. In this aspect, the Higher Andes experiment is closer to the observation (94% of moderate or neutral SSTA). The meridional distribution of SSTA is closely related to the frequency of ENSO and the meridional span of the anomalous Bjerknes feedback [e.g., Neale et al., 2008].

Fig. 3.8 shows the seasonality of the ENSO variations. ENSO variability peaks during boreal winter and is weakest during boreal spring. This pattern is reproduced by both experiments but the intensity of the variability is too high in the Control experiment and is mostly correct in the Higher Andes experiment (within the observed values; blue lines). A closer analysis shows that the intensity of the seasonality (defined as the variability during November-January divided by March-May) is slightly increased in the Higher Andes experiment compared to the Control experiment and is closer to the observation (NINO3.4 region ((5°N-5°S, 170°W-120°W): 1.4 (Higher Andes), 1.3 (Control) and 1.7 (Observation); NINO3 region: 1.2 (Higher Andes), 1.2 (Control) and 1.7 (Observation)).

3.4.2 Skewness

The SSTA skewness is a key measurement of the ENSO asymmetry, which is produced by the nonlinear processes in the ENSO cycle [e.g., An et al., 2020]. In the eastern Pacific NINO3 region, the SSTA skewness is strongly positive [Dommenget et al., 2013], meaning that El Niño events can reach larger amplitudes than La Niña events, but occurring less frequently.

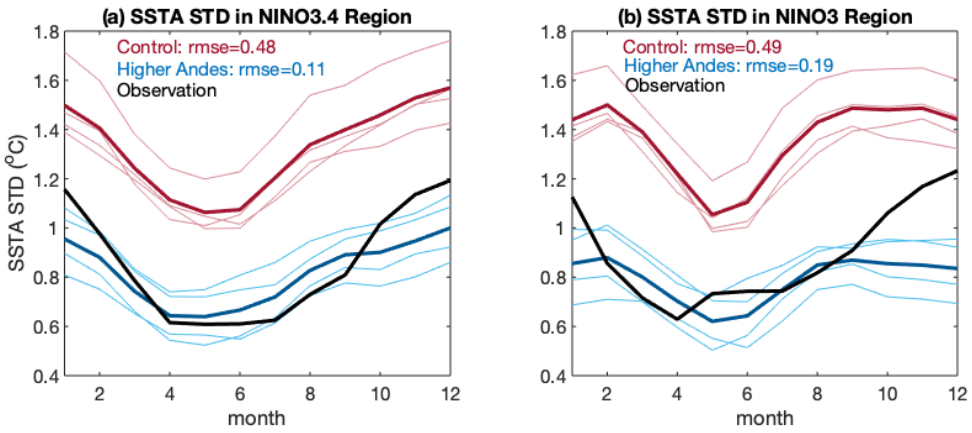

Figure 3.8: Seasonal evolution of SSTA STD (°) in (a) NINO3.4 region and (b) NINO3 region.

Similar to Kohyama et al. [2017], we calculated the skewness of the 11-month running mean NINO3 SSTA (Fig. 3.9a), and find a value of 0.9. The same method is applied to the Control (Fig.3.9b) and Higher Andes (Fig. 3.9c) experiments. In the control experiment, the skewness is less than half of the observed (0.4), suggesting that the El Niño and La Niña events are too similar in amplitude. In the Higher Andes experiment, the skewness (0.7) is still too weak but much closer to the observed value. The calculation of the skewness is consistent with the changes in the PDF of the experiments (Fig. 3.7b). The variation in the observations ranges from -1.94 °C to 3.19 °C. In the Control experiment, the range is -3.26 °C to 3.81 °C, while in the Higher Andes experiment it is -2.14 °C to 3.33 °C. Thus, the Higher Andes experiment captures a more similar variation range and the asymmetry between positive and negative phases.

3.4.3 Spectral Characteristics

The spectra of the NINO3 index can reveal the variability across time scales of the ENSO cycle [Guilyardi et al., 2009]. In the spectrum of the observed NINO3 index time series, the strongest signal is at 0.27 /yr, which is a 3.7 years cycle but even with this strongest signal, its normalized amplitude is only 0.51. The dominant ENSO

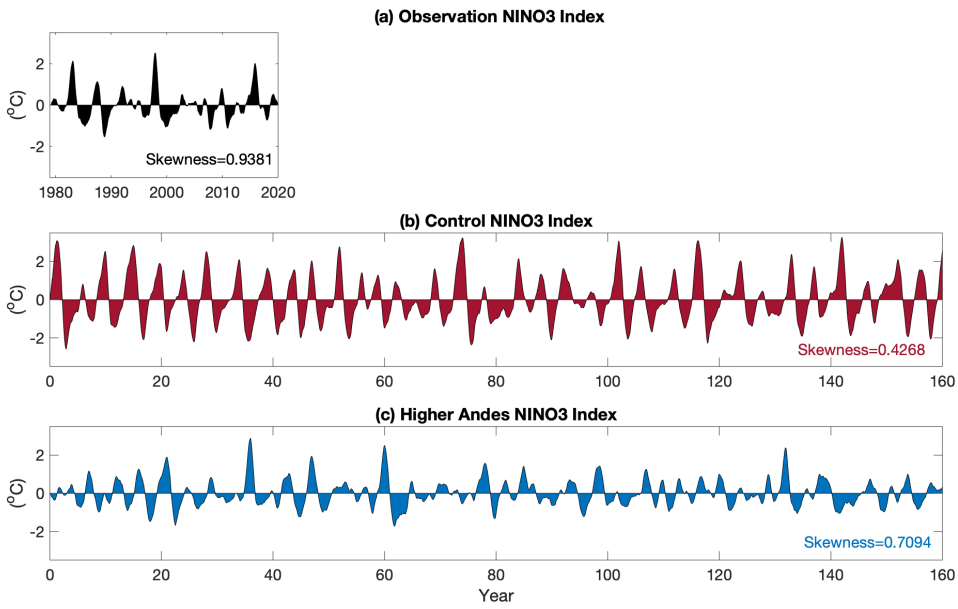

Figure 3.9: Time series of 11-month running mean Niño3 index, as Kohyama et al. [2017], for (a) observations, (b) Control and (c) Higher Andes. Skewness of the distributions indicated at the bottom right of each panel.

cycle does not have a very strong signal at a particular frequency; instead, the ENSO cycle is somewhat irregular and its period is around 4 years.

To perform a spectral analysis with uncertainties appropriate for comparison to the observed 40-year record, we used 160 years of data split into 4 sections of 40-years spans of data. The spectrum is calculated for each section (light lines) and then the average at each frequency (bold lines) for the Control and Higher Andes experiments (Fig. 3.10) are shown. The Control experiment spectrum has an excessive peak at the frequency of 0.22/yr, revealing its very strong periodic 4.5-year cycle, which is contradictory to the observation. A weaker peak near a 10 year period is also present in the Control experiment, but not in the observation. In the Higher Andes experiment, the 4.5-year and 10-year peaks disappear and the spectrum more realistically captures a 3 to 8 year irregular, broadband ENSO cycles. Although the amplitude of the Higher Andes experiment is slightly weaker than the observed spectrum, the observed spectrum falls within the error bars of the Higher Andes experiment in

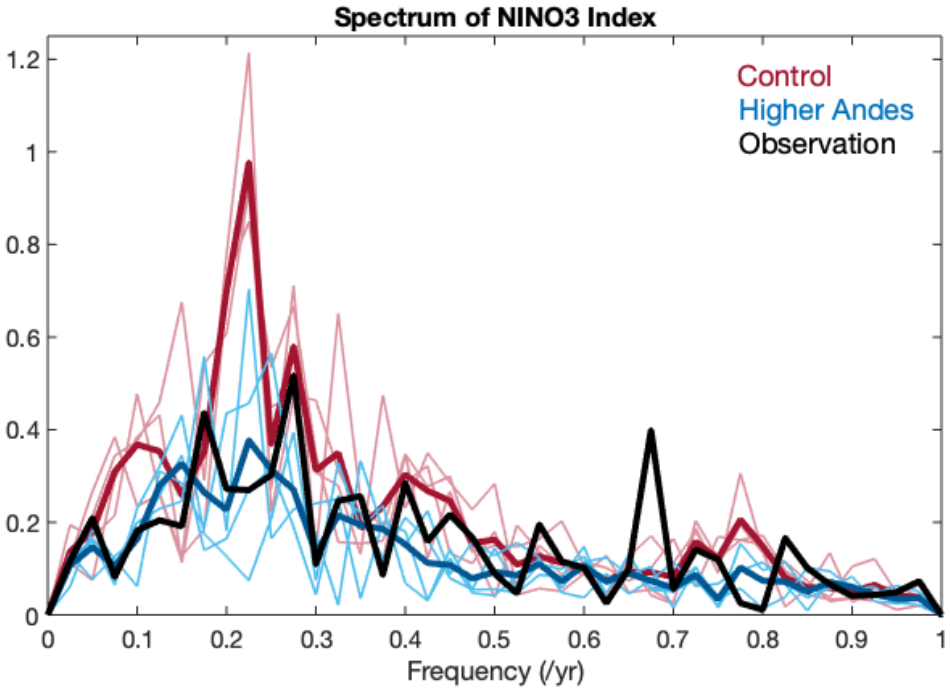

Figure 3.10: Normalized spectrum of Niño3 index. The 160 year model results are divided into 4 non-overlapping sections of 40 years. Spectrum of each section is plotted as thin, light line and the averaged value of the 4 sections is plotted as thick, bold lines. See Method section for detailed explanations.

most of the frequencies between 0.1 and 0.4. At higher frequencies (0.5 cycles/year and above), the observations and both simulations agree. The irregularity of ENSO over its dominant frequency range is therefore much improved in the Higher Andes experiment.

3.5 Mechanism

The modification of the Andes results in a more La Niña-like oceanic mean state (steeper thermocline tilt, colder eastern Pacific surface waters, enhanced eastern Pacific zonal and meridional wind stresses), accompanied by fewer, less periodic, meridionally narrower, and less extreme ENSO events with greater asymmetry between El Niño and La Niña. For the changes in the mean state, the mechanisms are similar

to what has been discussed in Xu and Lee [2021], with the additional influence of ocean dynamical processes, especially upwelling and horizontal advection. A higher elevation of the Andes has a stronger effect in squeezing the isentropic layers in the atmosphere compared with the Control experiment. As a result, when the mid-latitude westerly wind approaches the Andes, it becomes more difficult for the air mass to cross the mountains so the wind turns equatorward. This equatorward turning is accompanied by downward motion because of conservation of potential vorticity. With the strengthening of the anticyclonic motion in the southeast Pacific associated with this equatorward turning, the atmosphere will have lower specific humidity and stronger latent heat uptake, enhancing the formation of the low-level clouds above the ocean. These low-level clouds will block the shortwave radiation and further lower the SST in a positive feedback [Takahashi and Battisti, 2007a]. The thermocline becomes more tilted and the eastern upper Pacific less stratified. The ocean upwelling is weaker in the eastern Pacific and stronger in the central Pacific, consistent with the change in zonal wind stress. These changes in the Higher Andes experiment are correlated with the ENSO variations, either by changing the mean state feedback or by changing the strength of the correlation between anomalies.

We calculated the Bjerknes Index (BJ) as Eq. 3.1 (Fig. 3.11), where uncertainty in each terms is estimated based on 1000 samples using Bootstrapping method. Detailed comparisons for each term are shown in Table 3.1. Results indicate that the reason for the weaker ENSO in the Higher Andes experiment is the stronger damping effect from the mean state. Among the contributions from the different terms, the difference is mainly due to the stronger Thermal Damping, the stronger Mean Advection Damping and the weaker Thermocline feedback.

The thermal damping term is the linear regression between the surface energy flux anomaly and the eastern Pacific SST anomaly. The surface energy flux depends negatively on the regional SST, and in the Higher Andes experiment this regression

Name of the Term	Decomposition Definition	Control	Higher Andes	
TD	$-\alpha_s$	$Q_s = -\alpha_s < T' >$	**-1.64**	**-1.82**
	$*-\alpha_{SW}$	$SW_s = -\alpha_{SW} < T' >$	**-0.40**	**-0.23**
	$*-\alpha_{LW}$	$LW_s = -\alpha_{LW} < T' >$	-0.05	-0.05
	$*-\alpha_{LH}$	$LH_s = -\alpha_{LH} < T' >$	**-1.08**	**-1.41**
	$*-\alpha_{SH}$	$SH_s = -\alpha_{SH} < T' >$	-0.12	-0.13
MA			**-0.59**	**-0.68**
	Udamp	$-\frac{<\overline{u}>}{L_x}$	**0.36**	**0.26**
	Vdamp	$-\frac{<-2y\overline{v}>}{L_y^2}$	**0.49**	**0.46**
	Wdamp	$-\frac{<\mathcal{H}(\overline{w})\overline{w}>}{H_m}$	**-1.45**	**-1.40**
ZA			0.43	0.44
	μ_a	$[\tau_x'] = \mu_a < T' >$	5.36e-3	5.29e-3
	β_u	$< u' >= \beta_u[\tau_x']$	4.26	4.85
	$\left\langle \frac{\partial \overline{T}}{\partial x} \right\rangle \times C_{time}$		**18.63**	**16.97**
EK			0.20	0.19
	μ_a	$[\tau_x'] = \mu_a < T' >$	5.36e-3	5.29e-3
	β_w	$< \mathcal{H}(\overline{w})w' >= -\beta_w[\tau_x']$	2.50e-5	2.37e-5
	$\left\langle \frac{\partial \overline{T}}{\partial z} \right\rangle \times C_{time}$		1.46e+6	1.50e+6
TH			**0.67**	**0.56**
	μ_a	$[\tau_x'] = \mu_a < T' >$	5.36e-3	5.29e-3
	β_h	$< h' >= \beta_h[\tau_x']$	**5.71**	**5.09**
	a_h	$< \mathcal{H}(\overline{w})T_{50m}' >= a_h < h' >$	17.93	17.44
	$\left\langle \frac{\overline{w}}{H_m} \right\rangle \times C_{time}$		1.22	1.19
BJ			**-0.94**	**-1.31**

Table 3.1: BJ index equation (Eq. 3.1) terms comparison. Terms with bold text are not overlapping in 33% - 67% range (1 STD) between the two experiments, which means the change is significant. '*' represents terms that are not directly included in the BJ index equation. C_{time} is the time constant that converts the unit from s^{-1} to yr^{-1}.

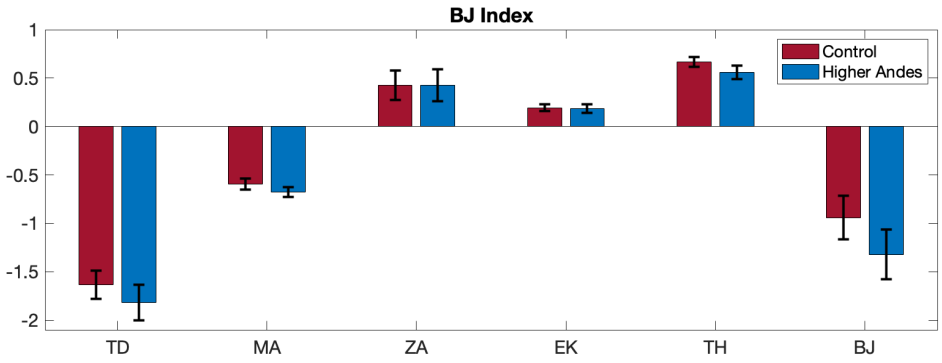

Figure 3.11: BJ Index in both experiments. TD: Thermal Damping. MA: Mean Advection damping. ZA: Zonal Advection feedback. EK: Ekman feedback. TH: Thermocline feedback. BJ: BJ Index, sum of all the previous terms. The error bars represent 95% confidence level. They are obtained by bootstrapping of the original data 1000 times, calculating the corresponding BJ indexes with each bootstrapping sample, then compute the standard deviations of each term.

has a steeper slope. According to Kim et al. [2014], this atmospheric feedback is underestimated in the CMIP3 and CMIP5 models. In our experiment, the changes in the regression are mainly contributed by the change in latent heat flux (Table 3.1). The Higher Andes experiment has stronger downward motion of the air over the southeast Pacific with lowered specific humidity, inducing stronger evaporation and takes up more latent heat flux from the ocean surface. The stronger latent heat flux contributes to a stronger thermal damping. However, this term, estimated by linear regression, has a relatively large uncertainty related to the fact that the thermal damping includes some nonlinear feedback including the subsidence response to SST and the high-level cloud cover. Thus, thermal damping is only moderately stronger in the Higher Andes experiment than in the Control experiment.

The second term that contributes to the stronger damping BJ index is the mean advection damping. Among the three directions, the zonal and meridional mean currents are positive feedback that strengthens the ENSO cycle, but the vertical current has a much stronger negative effect. In the comparison between the Control and the Higher Andes experiments, the changes in all three dimensions are significant

(Table. 3.1). The weaker zonal mean current feedback is the main contributing term for the difference between Higher Andes and Control experiments. In the Higher Andes experiment, the mean westward current velocity in the NINO3 region within the mixed layer decreases from 5.4 cm/s to 3.5 cm/s (36% decrease). This change is consistent with the weaker zonal wind stress in the eastern tropical Pacific region (Fig. 3.4b).

The third term that contributes the the stronger damping is the weakened Thermocline feedback in the Higher Andes experiment. The thermocline feedback quantifies the influence from the thermocline depth anomaly to the eastern Pacific surface temperature anomaly. In the Higher Andes experiment, the eastern Pacific becomes colder and the mean thermocline becomes deeper (Fig. 3.6. As a result, the upper ocean is less stratified in the NINO3 region (Fig. 3.5). When the eastern equatorial Pacific becomes less stratified, the zonal thermocline slope is less sensitive to the wind stress [Kim et al., 2014] (β_h in Table 3.1). With the weaker oceanic response to the wind anomaly in the Higher Andes experiment, the Thermocline Feedback becomes weaker and results in a weaker ENSO cycle.

Combining all the terms of the BJ index, the average damping index changed by 38%, from -0.94 in the Control experiment to -1.31 in the Higher Andes experiment. Therefore, it is very likely that the ENSO amplitude is weaker in the Higher Andes experiment because of the stronger overall damping effect.

3.6 Conclusion

In this study, we performed an experiment to understand how the simulated height of the Andes affects the Pacific climate of the CESM atmosphere-ocean global coupled model. The results show that by elevating the height of the Andes, the model simulates the tropical Pacific mean state climate and the ENSO variations better, which

suggests that creating elevation maps by simply smoothing away the high and low features of high resolution observations is an oversimplification. For the mean state climate, the Higher Andes experiment results in a greater east-west and north-south SST gradient, and reduced precipitation over the south Pacific. Easterly wind stress in the eastern and central Pacific becomes stronger, accompanied by stronger cross-equator southerly wind stress. In the upper ocean, the Higher Andes experiment is less stratified over the eastern tropical Pacific, and it has a steeper east-west thermocline slope. ENSO variability is strongly affected: the Higher Andes experiment exhibits a smaller amplitude, a greater skewness and a less regular ENSO period. All of these changes exceeded the uncertainty due to limited simulation length, and all are more consistent with observations results. Therefore, in this version of CESM a higher elevation of the Andes allows better simulation of the tropical Pacific mean state as well as ENSO variations in the CESM coupled model.

Although the improvement in the mean state climate and the ENSO properties are related, it is hard to distinguish cause and effect. On the one hand, the changes in the climate mean state can influence the ENSO characteristics [e.g., Fedorov and Philander, 2000, Hu and Fedorov, 2018, Zhao and Fedorov, 2020]. Zhao and Fedorov [2020], suggesting that strengthening of thermocline stratification and deepening the mean thermocline depth will produce stronger ENSO. In our simulations, the Higher Andes experiment has a weaker upper ocean stratification and a shallower thermocline depth over the central and eastern Pacific (Fig. 3.6), and we found a consistent change toward weaker ENSO events (Fig. 3.7). In addition, Hu and Fedorov [2018] suggests that with a stronger zonal wind over the central-western Pacific and stronger cross-equatorial winds over the eastern Pacific, there will be a weaker amplitude of ENSO variations. Consistently, our results also suggest that the elevation of the Andes strengthens the wind and weakens ENSO variability. On the other hand, the changes in the ENSO variations can also influence the tropical Pacific mean state. Because of

the asymmetry of El Niño and La Niña, the changes of the mean state can result from the varying occurrence and strength of strong El Niño and La Niña events, and the residual between them [Rodgers et al., 2004, McPhaden et al., 2011, Atwood et al., 2017]. In our result, the Higher Andes experiment significantly reduces the occurrence of strong El Niño events, but has a smaller influence on the La Niña events (Fig. 3.9). As a result, the eastern Pacific will have a cooler mean state in the Higher Andes case.

Feng and Poulsen [2014] performed a similar experiment of modifying the height of the Andes in a similar global coupled climate model (CCSM4), and examined the response of the Pacific climate. However, their purpose was to understand the impact of Andean uplift over geological time, while our purpose was to understand biases in the modern Pacific climate and ENSO. Furthermore, the details of how the Andes were changed and thus the results are quite different. Feng and Poulsen [2014] carried out their experiment to understand if the long-term climate transition in the Pacific since late Cenozoic is the result from the from 1 to 3 km kilometer-scale uplift of the central Andes. Our experiment is seeking an appropriate representation of the Andes in global climate models for the present day (changing the maximum elevation from about 2 km to about 5 km), so as to understand the model biases in the Pacific climate simulation. With this purpose, we compare our results against observations to evaluate the simulation's performance. In addition, the resulting changes in ENSO here are distinct from Feng and Poulsen [2014]. In their experiment, as the height of the Andes increases, the ENSO period decreases. In comparison, here no obvious change in the dominant frequency occurs, but the strength of the NINO3 index spectral band reduces in our Higher Andes experiment (Fig. 3.10). In their histogram of ENSO events, they have slightly more extreme El Niño and La Niña events, less moderate El Niño and La Niña events and more weak El Niño and La Niña events in the Higher Andes experiment. In our result, both extreme and

moderate El Niño and La Niña events decreased in frequency in the Higher Andes experiment (Fig.3.7b), and phase asymmetry increased. However, consistent with our results, they find that the mean zonal SST gradient increased with increasing the height of the Andes, although more so than in our experiment. They found major strengthening of zonal winds while we find modest changes to the mean wind magnitude and structure.

Overall, we consider the modification of the Andes an improvement in representing the South American topography and the tropical Pacific mean climate and its variability. This work highlights the fact that increasing the resolution of a climate model without addressing the height of the Andes could be problematic.

Chapter 4

The Andes and extreme precipitation in South America

4.1 Introduction

La Plata basin has the most intense storms, with the highest occurrence of top 0.001% strong convection in the world [Zipser et al., 2006]. Located in the southeast of South America, it is bounded by the Brazilian Highlands to the north, the Andes Mountains to the west, and Patagonia to the south, and it is the intersection area of many countries including Bolivia, Brazil, Paraguay, Uruguay, and Argentina. Using the Tropical Rainfall Measuring Mission (TRMM) data and analyzing different precipitation features, Zipser et al. [2006] shows that these intense storms take place in austral spring, from September to November. More precisely, the high-resolution precipitation data shows that the hourly rainfall is stronger in October than in September and November [Filho et al., 2014]. Consistently, Rasmussen et al. [2014] also uses lightning data to show the La Plata basin region has the world's deepest convective storms in October.

Understanding these severe storms is of great importance. These severe storms are accompanied by intense rainfall, big hail, and strong lightning, and they cause damage to towns and vineyards [Witze, 2018]. In the recent few decades, severe thunderstorms are occurring more frequently in the La Plata basin [Taszarek et al., 2021]. Cerón et al. [2021] finds that the total precipitation days has increased by 15% and heavy precipitation day in the south La Plata basin has increased by 20%, bringing more concerns to the more frequent extreme climate conditions under global warming. In addition to global warming, Zhu et al. [2016] finds that South America is experiencing significant land use change. The change in surface types can influence convective features and precipitation [Lee et al., 2011].

Among the possible factors that contribute to the formation of these severe storms, we are particularly interested in the influence from the Andes. The Andes creates the South America Low-Level Jet (SALLJ) located at the west, whose strength is closely related to the strength of La Plata precipitation. Montini et al. [2019] suggests that the trend of increased precipitation over the La Plata basin in the recent decades is

a result of the enhanced SALLJ, which is related to the poleward expansion of the South Atlantic subtropical high-pressure center [Zilli et al., 2017]. SALLJ contributes to the severe storms for two important reasons. First, it provides moisture supplies for precipitation. Over 70% of the available water vapor for precipitation over the La Plata basin is directed by SALLJ [van der Ent et al., 2010, Montini et al., 2019], which is similar to the contribution from the Rocky mountains to the North America tornadoes [Doswell III et al., 2012]. Second, the capping from the upper-level westerlies creates an environment for the accumulation of instability in SALLJ, providing the condition for intense convection when this large instability releases [Houze Jr., 2012].

In this paper, our goal is to confirm the time and location of these severe storms with the precipitation data and understand how the Andes influence their formations. To achieve these goals, we use satellite data to examine the South America extreme precipitation, and climate models to investigate how the Andes influence the formation of these severe storms. We explain our data and model experiments in Section 2. We analyze the high-resolution satellite data to understand the seasonal cycle and location of these severe storms in Section 3. We design two model experiments and quantify the how the Andes influence these severe storms in Section 4, and analyze the change in vertical wind shear and moisture flux the mechanism in Section 5. We conclude our results in Section 6.

4.2 Satellite Data and Model Experiment

4.2.1 Satellite Data

In addition to the lightning data shown in Rasmussen et al. [2014], we investigate the severe storms in terms of the precipitation extremes so that we can compare with model outputs in the same variable. Therefore, we use the Climate Prediction Center

(CPC) Morphing Technique (MORPH) precipitation data [Xie et al., 2020], with a time resolution of 30 minutes and a spatial resolution of 8km. The data is available from 1998 to 2019, and we use the entire time series for our study.

We use this very high time and spatial resolution satellite data in order to keep track of these short-term processes. For our research interest, we only subset the data located within the range of 15°S-45°S, 38°W-75°W in our analysis.

4.2.2 Model Experiment

To investigate the influence of the Andes, we use the National Center for Atmospheric Research (NCAR) Community Earth System Model (CESM) version 1.2.2, with Community Atmosphere Model, version 4 (CAM4) as the atmospheric component. The experiments are run with slab ocean settings because the major features of the mean climate and atmospheric circulation features due to the mountain are well captured without ocean circulation [e.g., results in Xu and Lee, 2021, Xu et al., 2022]. We choose the resolution of $0.47° \times 0.63°$ to resolve the shape and elevation of the Andes better. The atmosphere CO_2 concentration is set to be 367 ppm to match the value in the year 2000. The experiments are run for 35 years and we use the last 15 years of outputs for our analysis since it already reached the equilibrium. The model's daily outputs for precipitation and moisture flux are used for the analysis.

At the resolution in our experiments, the model's default topography setting in South America is as Fig. 4.1b. Compared to the 1-km high-resolution topography from the National Oceanic and Atmospheric Administration (NOAA) National Geophysical Data Center (NGDC) Global Land One-km Base Elevation (GLOBE) topography (Fig. 4.1a) [Hasings et al., 1999], the default setting is representing the shape and the height of the Andes reasonably.

Choosing a high-resolution model and capturing the reasonable elevation of the Andes is very important in our experiment. Xu et al. [2022] shows that low-resolution

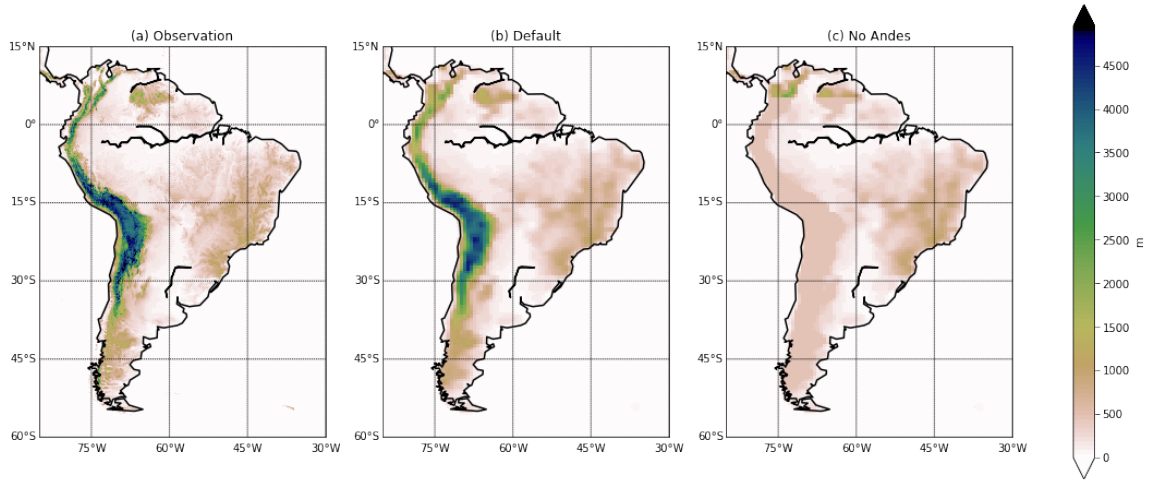

Figure 4.1: (a) High-resolution satellite data for South America topography. (b) CESM default topography setting with the resolution of 0.5°. (c) Topography setting for the 'No Andes' experiment. The whole Andes mountain area's elevation is adjusted to 500m.

models can not block the mid-latitude westerly wind from the Pacific Ocean sufficiently because the Andes is too low, resulting in errors in simulating the eastern Pacific cold tongue. Similarly, the high-resolution climate model will effectively redirect tropical easterly wind at the east of the Andes.

We modify the Andes as Fig. 4.1c, in which we choose the Andes area and adjust its elevation to 500 m. The whole Andes region is a plain field. We run the slab-ocean model for this experiment with the exactly same setting as the default one except for the topography and compare the difference between their results.

4.3 Precipitation Extremes in South America

CMORPH satellite data shows the annual mean precipitation takes place on the La Plata basin as well as on the South Atlantic Ocean. The annual mean precipitation distribution (Fig. 4.2a) shows that the region with the highest average precipitation is near 27°S, 55°W on the South America continent, as well as near 38°W in the open ocean. Precipitation is suppressed near the Andes mountain area as well as on the

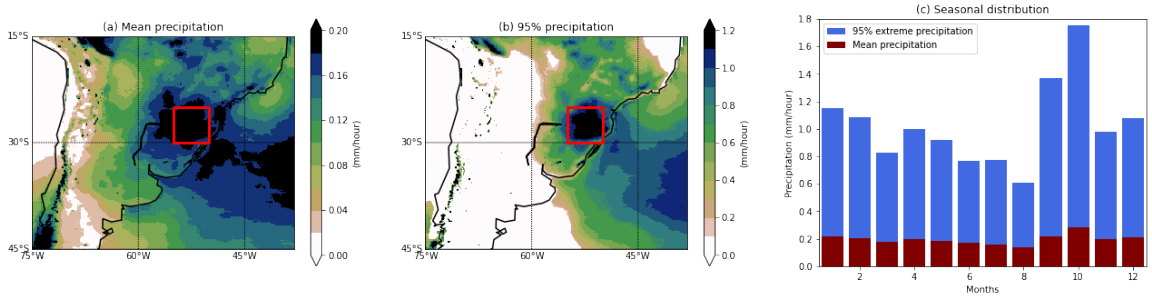

Figure 4.2: CMORPH satellite data for precipitation. The time resolution is half an hour. (a) Annual average precipitation in South America. (b) The 95% precipitation strength of half-hourly local precipitation. (c) Seasonal cycle for precipitation extremes in the selected region. Red columns are average precipitation and blue columns are above 95% of the half-hourly value in this month.

eastern coast of the Pacific Ocean.

Extreme precipitation is only strongest over the La Plata basin. For the satellite data, extreme precipitation for each grid point is calculated as the 95% value of 30-minute precipitation ranked over 22 years time series. As shown in Fig. 4.2b, the spatial distribution of extreme precipitation is different from the distribution of the average precipitation. Firstly, the most severe precipitation occurs on the La Plata basin at around 28°S, 52°W. Compared with the land area, although the ocean also has high average precipitation, its extreme precipitation is weaker. The ocean has more frequent but milder precipitation, while land has stronger single precipitation events. Secondly, the majority of the region to the west of 60°W has extreme precipitation values below 0.1 mm/hour, which means that this region rarely rains and only has mild rainfall. The La Plata basin has stronger mean and extreme precipitation compared with the south Amazon forest. The region where the most severe precipitation occurs is very consistent with the region shown in Fig. 1 of Rasmussen et al. [2014], indicating that the region with severe lightning is accompanied by severe precipitation.

The seasonal cycle of precipitation over La Plata basin shows the maximum mean and extreme precipitation are both in October. We select the region where the most

severe precipitation is strongest, as was shown in the red box in Fig. 4.2b, and did the same ranking process for each month (Fig. 4.2c). The monthly average precipitation varies in a small amplitude, with the least precipitation in August and most precipitation in October. The 95% precipitation has the strongest peak in October, with the amplitude of 1.77 mm/hour (42.5 mm/day). The strongest extreme precipitation in October consistent with Rasmussen et al. [2014], which observes strongest lightning in October on La Plata basin.

4.4 The Influence from the Andes

The CESM default experiment precipitation is similar to the satellite data in spatial distribution and seasonal cycle, but the No Andes experiment has a different seasonal cycle and much weaker mean and extreme precipitation over the La Plata basin.

The annual mean precipitation shows a strong decrease at the La Plata basin and the eastern hillside without the Andes. From the default experiment annual mean precipitation (Fig. 4.3a), the La Plata basin, the east side of the Andes foothill, the coastline of the Brazilian plaetau and the south Amazon forest. When the Andes is removed, the mean precipitation over the La Plata basin and the eastern hillside of the Andes strongly decreases (Fig. 4.3b,c). Reduced rainfall at the foothill of the Andes is because without the mountain, there is no longer an elevation difference, and the easterly will not be uplifted and condensation does not occur, forming rainfalls at the west side of the continent. Rainfall at the La Plata basin is reduced because the moisture from the tropical region is no longer directed south by the mountain, and the lack of moisture supply reduces the rainfall by a great portion. The coastal precipitation along the eastern coastline remains strong in both experiments. This is because the formation of coastal precipitation is related to the Brazilian Plateau [Junquas et al., 2016], which we did not modify it in our settings.

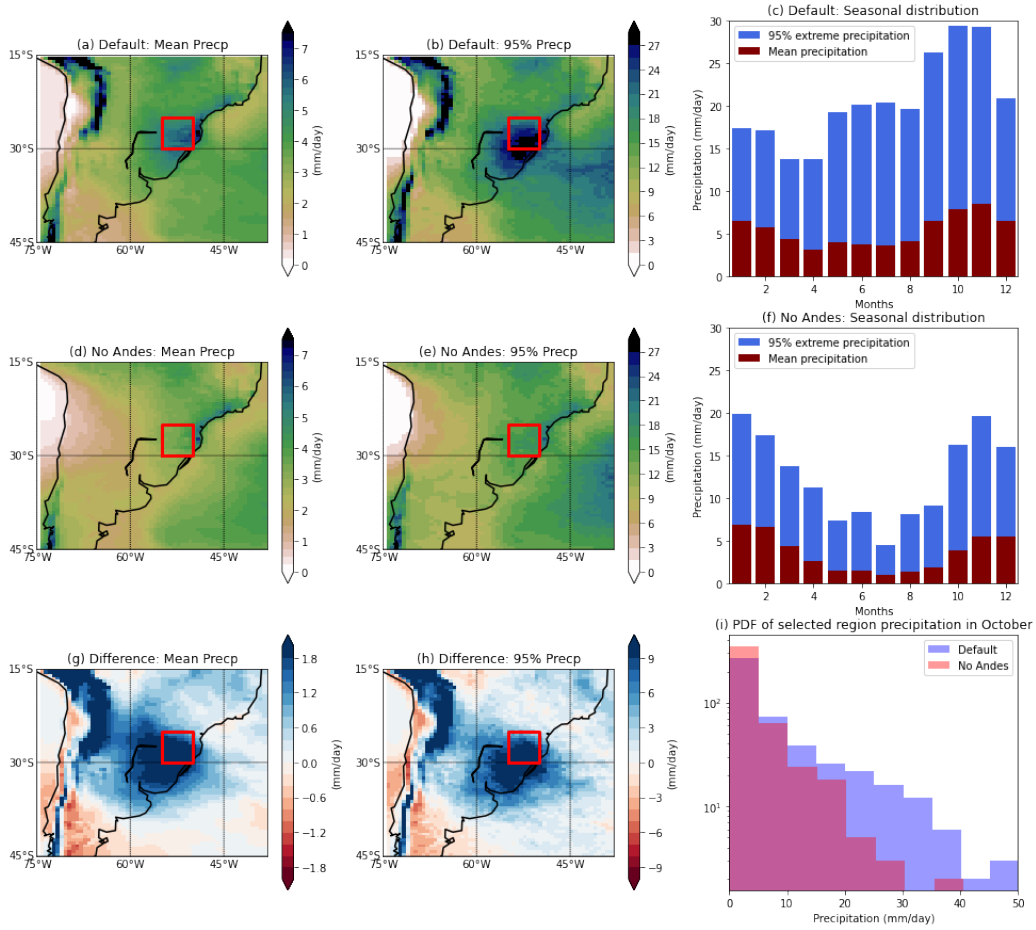

Figure 4.3: (a-c) Same as Fig. 4.2, but for the daily precipitation in the default model experiment. (d-f) Same as Fig. 4.2, but for the daily precipitation in the No Andes model experiment. (g) Difference between (a) and (g). (h) Difference between (b) and (e). (i) Probability Distribution Function (PDF) of the selected region's daily precipitation strength in October.

Extreme precipitation also decreases over the La Plata basin and the eastern hillside in the No Andes experiment. In the model results, extreme precipitation is calculated as 95% most intense daily precipitation over 15 years (Fig. 4.3b,e). The extreme precipitation is weaker than the satellite data because in the model results we rank the daily data while in satellite observation we ranked the half-houly data. In the default topography experiment, the region with the greatest intensity is similar in the eastern Andes foothill and the La Plata basin, which implies these two regions have frequent occurrences of strong precipitation. On the contrary, the

Amazon forest and the Atlantic ocean have high average precipitation but relatively weak extreme precipitation, which means these two regions rain very often but with mild intensity. In the No Andes experiment, regions that receive a large decrease in extreme precipitation (Fig. 4.3h) is similar those in mean precipitation (Fig. 4.3g). This result implies that role of the Andes for the mean and extreme precipitation is similar. For the La Plaba basin, it provides a pathway for the available moisture supply from north to south. For the eastern hillside, it forces the uplift of air and causes condensation of water vapor.

The La Plata basin mean and extreme precipitation change without the Andes. We calculate the monthly values of mean and 95% extreme precipitation within the boxed area for both experiments (Fig. 4.3c,f), and find a large difference between the two experiments. Firstly, the mean and extreme precipitation are a lot weaker in the No Andes experiment. The annual mean precipitation decreases from 5.4 mm/day in the default experiment to 3.5 mm in the No Andes experiment, with a decrease of 35%. The annual 95% extreme precipitation (not shown in the figure) decreases from 21.7 mm/day in the default experiment to 14.5 mm/day in the No Andes experiment, with a decrease of 49%. Secondly, the seasonal contrast is more obvious in the No Andes experiment. Comparing the precipitation in winter times (June - August) with the summer times (December-February), the No Andes experiment shows a larger difference with much dryer summer in the La Plata basin region. Thirdly, the month with the strongest extreme precipitation changes without the Andes. Similar to the satellite observation, the default experiment still finds the most extreme precipitation in October, but the November extreme precipitation is almost equally strong. In the No Andes experiment, the month with the largest mean precipitation and strongest extreme precipitation is January, around the time that insolation is at its maximum in the southern hemisphere.

The October daily precipitation histogram of La Plata basin shows the No An-

des much less heavy rain days without the Andes (Fig. 4.3). We notice that the distribution switch to a longer tail with a lower peak pattern, indicating there are fewer near-zero precipitation days and more medium and strong precipitation days. This result supports that the Andes is an important factor for the October extreme precipitation in the La Plata basin region.

4.5 Mechanism

To understand how the Andes changes precipitation, we examine two major factors in both experiments: vertical wind shear and surface moisture flux (Fig. 4.4). According to Pucik et al. [2021], the developments of strong convection require the existence of strong vertical wind shear that provides instability. In the meanwhile, sufficient moisture supply can ensure enough precipitation water required for these severe storms [Montini et al., 2019], and near surface moisture is important to the formations of heavy-rain-producing convective systems [Schumacher, 2015].

For the vertical wind shear analysis, we select the same boxed area as in the precipitation extreme to examine the local environment's instability. October vertical wind shear in the default and No Andes experiments (Fig. 4.4a,c) show similar spatial distributions, with the strongest wind shear belt at 30°S. In the mid-latitude region, the vertical wind shear is mainly decided by the upper-level wind because it is much stronger than the surface wind. The upper-level wind at 300 hPa is less influenced by the Andes, resulting in a similar vertical wind shear pattern in both experiments. In the default experiment, this belt is slightly deflected to the south, because the isentropes have to stretch to cross the mountain, and this stretching of air column will result in a poleward turn. This poleward deflection of the wind belt causes a weaker vertical wind shear within the boxed region in the default experiment (Fig. 4.4e), but the overall seasonal cycles are similar in both experiment, which October is

the month with the strongest vertical wind shear. This strong vertical wind shear can prevent the undercut of the inflow of the storms, providing a favorable environment for storm-relative winds. In addition, it can develop an upward vertical pressure perturbation gradient force at the center of a storm, which ensures its persistence [Pucik et al., 2021].

In spite of the similar characteristics from the vertical wind shear, the different incoming surface moisture flux in different Andes settings causes the difference in extreme precipitation. Due to the close correlation between the near-surface moisture income and heavy precipitation [Schumacher, 2015], we only consider the moisture transport below 900 hPa. In order to sufficiently count for all the upstream flux, we enlarge the box region by 5° in each direction. In October, the near surface moisture source is from the northeast direction in both experiments (Fig. 4.4b,d), so we quantify the incoming moisture source from north and east in all seasons (Fig. 4.4f). The seasonal cycle shows that the default experiment has much stronger northerly moisture income from the Amazon forest all year round, and slightly stronger easterly moisture flow from the Atlantic in the spring. In October, the No Andes experiment has the anticyclonic wind circle centered towards the east, resulting in a weaker northerly and easterly moisture income in the boxed area. The cumulative moisture income in October is about 75% stronger in the default experiment. In October, although the No Andes experiment also has strong wind shear, it does not have sufficient moisture supply to ensure heavy precipitation.

In addition, the strong upper westerly wind and surface northerly jet (SALLJ) are both very important for the formation of the extreme convection. When the SALLJ reaches the mid-latitude area, the lee side of the mid-latitude westerlies crossed the Andes produce a capping inversion above it. This capping flow of dry air that allows potential instability to build up by the accumulation of sensible and latent heating below it [Houze Jr., 2012]. When the cap is broken, deep convection erupts and results

in the severe rainfall in La Plata basin. The lack of moisture supply and accumulation of instability explains the absence of severe storms are in the No Andes experiment.

In summary, the extreme precipitation in the October La Plata basin is closely related to the strong vertical wind shear, sufficient surface moisture supply and the existence of southward jet. The vertical wind shear is strongest in October, providing an environment with the instability that ensures the persistence of strong storms. The surface moisture flux from north and east is much stronger with the presence of the Andes, which provides the sufficient water supply for strong precipitation, resulting in severe storms in the La Plata basin. The upper westerly wind provides a capping for the low level jet to accumulate instability, building up capabilities for strong convection.

4.6 Conclusion

In this study, we use the high-resolution CESM model to show that the Andes is very important for the moisture supply for extreme precipitation for La Plata basin during October, and it influences the seasonal cycle of mean and extreme precipitation. We first analyze the satellite data from CMORPH to prove that the extreme precipitation in South America occurs in the La Plata basin region and these rainfalls are strongest in October. To understand how the Andes contribute to these extreme precipitation events, we run the CESM 1.2.2 with the slab ocean configuration and design two experiments with and without the Andes. The model results show that without Andes, the October severe precipitation in the La Plata basin region no longer exists. The annual mean precipitation decreases by 35% and extreme precipitation decreases by 49%. The seasonal cycle also changes without the Andes, with stronger summer-winter contrast and strongest extreme precipitation occurring in January. From further analysis of the vertical wind shear and surface moisture

flux in October South America, we find that the strength of the vertical wind shear provides the large-scale disturbance in October, forming an environment for intense convection. The Andes introduces stronger surface moisture from the Amazon and the Atlantic that provides the precipitation water. The accumulation of instability in SALLJ formed by the Andes increases the strength of convection. All these factors result in severe precipitation in the La Plata basin region during October.

Our ultimate goal is to understand the formation of the La Plata basin's severe storms better. Xu et al. [2022] shows that the correct representation of the Andes is important for the accurate simulation of the atmospheric circulation for the formation of the tropical Pacific climate. Similarly, in the simulation of the La Plata basin precipitation, a good representation of the Andes can improve the simulation of the moisture flux, resulting in better simulations of precipitation seasonality and intensity. Climate models still have some difficulties capturing the regional precipitation patterns and trends in South America precipitation [Rivera and Arnould, 2020], so having a better understanding for the related factors such as the Andes is very important. Under the background of global warming, there are more uncertain factors that we need to consider aside from the Andes, such as moisture supply and local land surface conditions. The warmer climate will hold more water vapor according to the Clausius-Clapeyron equation. In the mid-latitude southern hemisphere, precipitation extremes intensity increases by 5% with 1K of warming [O'Gorman and Schneider, 2009]. The change of local vegetation type in the La Plata basin is likely to change the soil moisture, surface temperature, and surface roughness, which will all influence the strength of convection. Extreme precipitation is expected to occur more frequently and with greater intensity under global warming [Masson-Delmotte et al., 2021], and having a better explanation and preparation is an important topic in climate science.

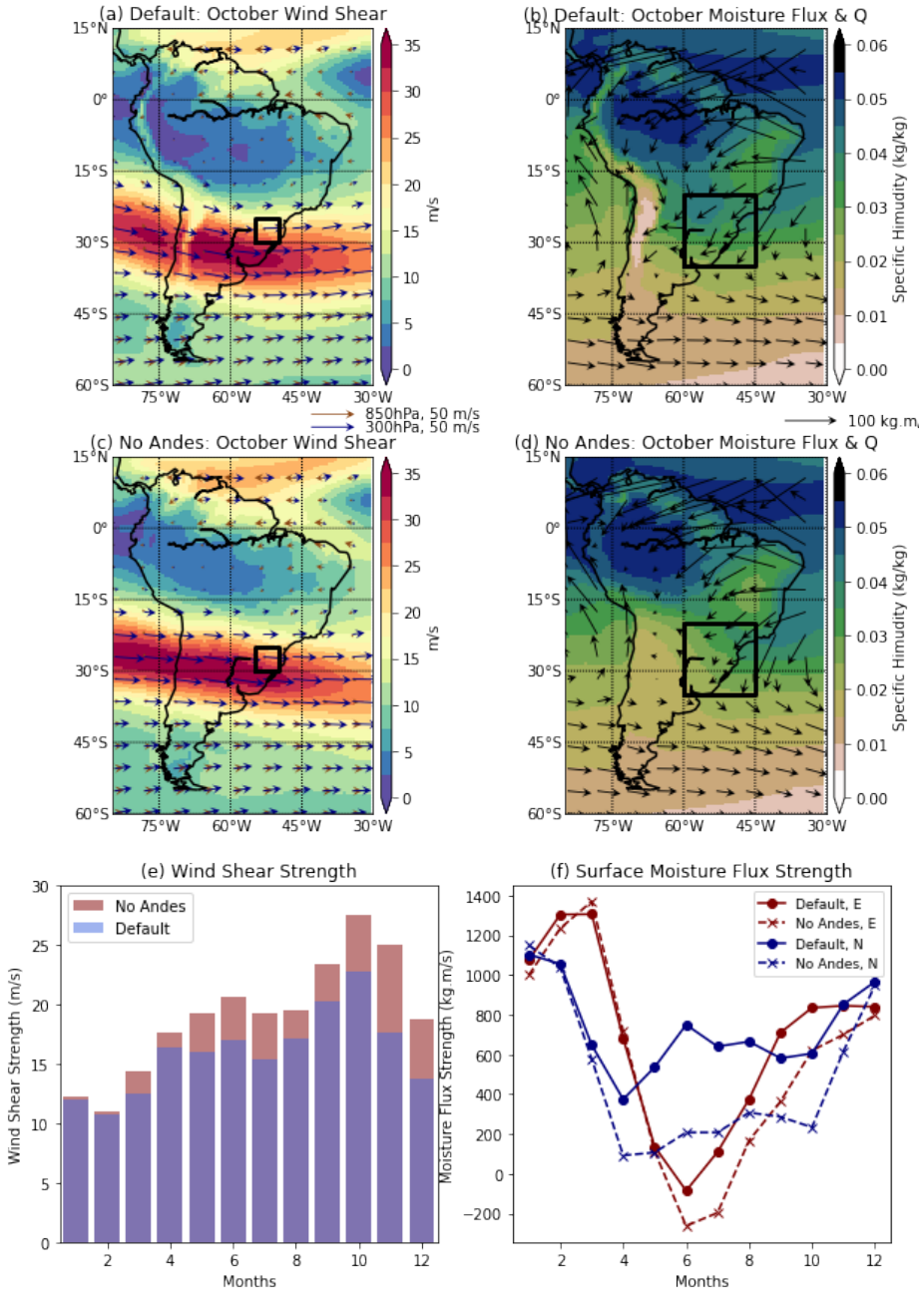

Figure 4.4: (a) Default experiment October: Arrows are the wind at 300 hPa (Blue) and 850 hPa (Brown). Color contours are the wind shear strength between 300 hPa and 850 hPa. Boxed area is the same as Fig. 4.2a. (b) Default experiment October: Arrows are the moisture flux (UQM and VQM) below 900 hPa. Color contours are the specific humidity below 900 hPa. Boxed area is extended by 5 ° in each direction. (c, d) Same as (a, b), but for the No Andes experiment. (e) The seasonal cycle of the strength of wind shear in the box area of (a, c). (f) The seasonal cycle of the strength of incoming surface zonal moisture transport from east of the box (red lines), and the meridional moisture transport from north of the box (blue lines).

Chapter 5

Topological Signature of Stratospheric Poincaré – Gravity Waves

5.1 Introduction

Much of what we understand about the climate system is made possible by recognizing the importance of waves in Earth's atmosphere and oceans. Waves are characterized by predictable periodic motion that contrasts with the chaotic or stochastic behavior displayed by many other components of the climate system. Remarkably, oceanic and atmospheric waves share fundamental physics with those in quantum matter, and topology plays an important role in the movement of the atmosphere and oceans. Although the basic equations for idealized equatorial plane waves in the atmosphere and ocean have been long known [see the historical perspective in Hendershott and Munk, 1970], wavelike variability has been observed in the atmosphere [Wheeler and Kiladis, 1999] and ocean [Farrar, 2008], and these waves have been linked to phenomena such as El Niño [Wyrtki, 1975] and the Madden-Julian Oscillation [Madden and Julian, 1971], their connection to topology has only recently been discovered [Delplace et al., 2017]. This discovery presents an opportunity to use more sophisticated statistical and mathematical analysis of the wave-like aspects of these phenomena, sharpening our insights into their emergence from diverse variability, fundamental mechanisms, and especially the ability of our modeling systems to appropriately simulate them. Waves are usually categorized dynamically by matching observed variability to predicted dispersion relations [e.g., Wheeler and Kiladis, 1999, Farrar, 2008], which relate the frequencies and spatial scales where waves may occur and how they propagate through space and time (Fig. 5.1). Here we demonstrate a different distinguishing and qualitative feature of certain waves, nontrivial topology, that can also be discerned from observations. The nontrivial topology found here in reanalysis data of stratospheric waves agrees with a recent theoretical prediction Delplace et al. [2017].

Topology is the field of mathematics concerned with the properties of spaces that do not change under continuous deformations. A doughnut and an orange are topologically distinct because the doughnut has a single hole (we say that it has a genus of

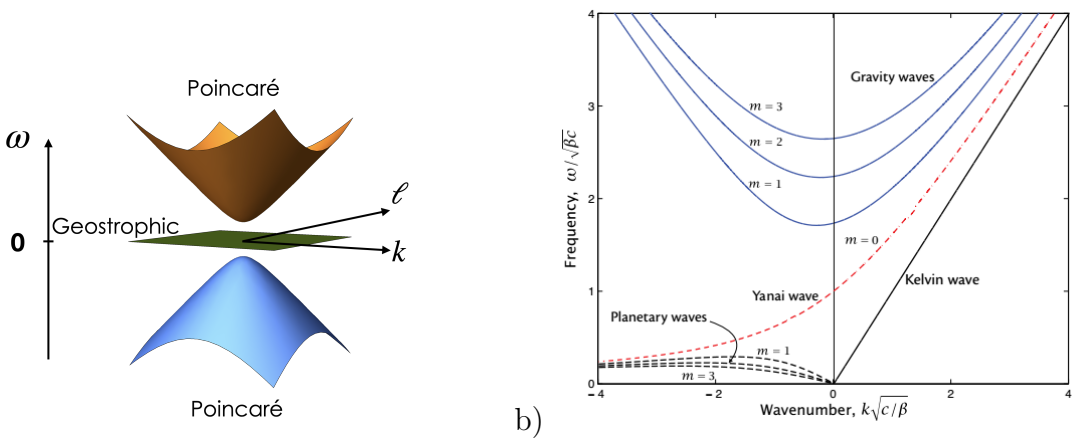

Figure 5.1: a) Dispersion relationship in frequency-wavevector space for the shallow water equations in the f-plane approximation. The upper and lower bands are positive and negative superinertial frequency modes of the Poincaré waves, and the subinertial range has only a zero frequency band containing modes in geostrophic balance as there is no β effect in the f-plane approximation. b) Equatorial β-plane dispersion relation showing the subinertial, quasi-geostrophic Rossby waves, the superinertial Poincaré waves, and the Kelvin and Yanai waves. Figure from Vallis [2019].

1) while the orange has a genus of 0. Likewise a coffee mug has the doughnut topology because it too has a single hole (the handle). Another example, more closely connected to the phenomena discussed below, is known as the Hairy Ball or Hedgehog Theorem that says that it is impossible to comb the spines of a hedgehog (because there will always be at least one tuft) [Renteln, 2013]. By contrast, if one's head were a torus instead of spherical, one's hair could be combed smoothly without a part–but probably only boring people would choose that hairstyle. Topology is a powerful tool that turns complicated problems into simple ones. For example, across an interface between topologically distinct states of matter, a general principle known as bulk-boundary or bulk-interface correspondence [Hasan and Kane, 2010] guarantees the existence of boundary or interfacial waves. The waves move in one direction and evidence *topological protection*, or immunity to backscattering even in the presence of defects. On a rotating planet, the equator acts as the boundary between two topologically-distinct hemispheres, and so some equatorial waves propagate only in one direction and are topologically protected (Fig. 5.1).

Past uses of topology in fluid mechanics have usually focused on coherent structures in space such as vortices. Here by contrast we study topology in wavevector-frequency space where it can for instance guarantee the existence of eastward propagating equatorial waves in Earth's climate system. In particular there is a topological origin for two well-known equatorially trapped waves, the Kelvin and Yanai modes, caused by the breaking of time-reversal symmetry by Earth's rotation, that helps to explain the robustness of these waves against buffeting by the weather. This resilience may also be implicated in other emergent equatorial wavelike phenomena such as the Madden-Julian Oscillation (MJO), remarkable for its eastward propagation along the equator.

Fig. 5.1a shows the dispersion relation for the idealized shallow-water model on the f-plane. There are three distinct bands: Positive and negative frequency Poincaré waves and a zero-frequency geostrophically balanced mode. The topology of each band is distinct and may be quantified in terms of a winding number (defined below) in frequency-wavevector space. In particular, the Poincaré-gravity modes are characterized by a vortex with winding number of ± 1. (The sign of the winding number depends on the sign of the product of the Coriolis parameter and the wave frequency.) Geostrophically balanced modes (that become Rossby waves once the Coriolis parameter is allowed to vary with latitude) are by contrast topologically trivial with zero winding number. The winding number of the Poincaré-gravity waves changes by 2 upon crossing the equator. By bulk-interface correspondence, there must therefore be 2 waves that traverse the otherwise forbidden region of frequency space. Spectral flow in frequency-wavevector space as the zonal wavenumber increases shows that the negative frequency Poincaré band loses two modes, the geostrophic band gains and loses one mode and the positive frequency Poincaré band gains the two modes. These are the equatorial Kelvin and Yanai waves. The two equatorial modes move with an eastward group velocity at all zonal wavenumbers, and this

unidirectional propagation reflects the breaking of time-reversal invariance by the planetary rotation.

In this chapter of the thesis, I quickly review the theory of topology in the context of the shallow water equations on the (constantly rotating) f-plane (Section 2). Then I discuss how I process the ERA5 reanalysis data from the stratosphere (Section 3). The winding number for the waves is presented in Section 4. A brief conclusion is presented in Section 5.

5.2 Theoretical Motivation

To motivate our investigation of the topology of waves in the stratosphere we briefly review the linearized shallow water equations on the f-plane following Delplace et al. [2017].

$$\begin{cases} \frac{\partial u}{\partial t} - f_0 v = -g\frac{\partial h}{\partial x} \\ \frac{\partial v}{\partial t} + f_0 u = -g\frac{\partial h}{\partial y} \\ \frac{\partial h}{\partial t} + H(\frac{\partial u}{\partial x} + \frac{\partial v}{\partial y}) = 0 \end{cases} \tag{5.1}$$

Here u and v are the zonal and meridional velocity, f_0 is the Coriolis parameter in the f-plane approximation and g is the gravitational acceleration. Also h is the height anomaly and H is the average depth of the shallow water.

By adopting periodic boundary conditions to eliminate any boundaries, the normal modes of the linearized shallow water equations may be easily found by Fourier transformation to frequency-wavevector space. Introducing the 3-component vector $\Psi(x,y,t) \equiv (u(x,y,t),\ v(x,y,t),\ h(x,y,t))$ and substituting $\Psi(x,y,t) = \tilde{\Psi}(k,\ell,\omega)\, e^{i(\vec{k}\cdot\vec{x}-\omega t)}$

with $\vec{k} = (k, \ell)$, we obtain

$$\begin{bmatrix} -i\omega & -f_0 & igk \\ f_0 & -i\omega & ig\ell \\ iHk & iH\ell & -i\omega \end{bmatrix} \times \begin{bmatrix} \tilde{u} \\ \tilde{v} \\ \tilde{h} \end{bmatrix} = 0 \tag{5.2}$$

This secular equation is solved to obtain three normal mode angular frequencies of $\omega_\pm = \pm\sqrt{gH(k^2+\ell^2) + f_0^2}$ and $\omega_0 = 0$. The corresponding amplitudes of the non-zero frequency Poincaré-gravity waves are:

$$\tilde{\Psi}_\pm = \begin{bmatrix} (k \pm i\ell) f_0 \\ (\ell \ \mp ik) f_0 \\ \pm H(k^2+\ell^2) \end{bmatrix} \tag{5.3}$$

Normal modes are defined only up to an overall phase and magnitude. To quantify the topoology we follow Zhu et al. [2021] by introducing gauge-invariant but complex-valued quantity Ξ defined as follows:

$$\Xi(k, \ell) \equiv v(k, \ell)\ h^*(k, \ell). \tag{5.4}$$

We say that Ξ is gauge-invariant because the phase of the normal modes cancels out; only the internal phase difference between the two components of the waves (in this case, meridional velocity and height) remains. For Poincaré-gravity waves, the gauge-invariant quantity displays a vortex or antivortex (depending on the signs of the frequency and the Coriolis frequency) centered at the origin in wavevector space:

$$\Xi_\pm(k, \ell) = \pm H f_0 (k^2+\ell^2)(l \mp ik) \tag{5.5}$$

The vortex / antivortex has winding number ± 1 which constitutes its topological

charge. The zero-frequency geostrophic mode, by contrast, has

$$\Xi_0(k,\ell) = v_0(k,\ell) \cdot h_0^*(k,\ell) = igf_0 k \tag{5.6}$$

and thus has a domain wall at $k = 0$ and zero winding number. Its topological charge therefore vanishes. The same result may be obtained from the barotropic quasigeostrophic equations as the wave height is proportional to the stream function while the meridional velocity is proportional to the zonal derivative of the stream function thus leading in wavevector space to the same form as Eq. 5.6.

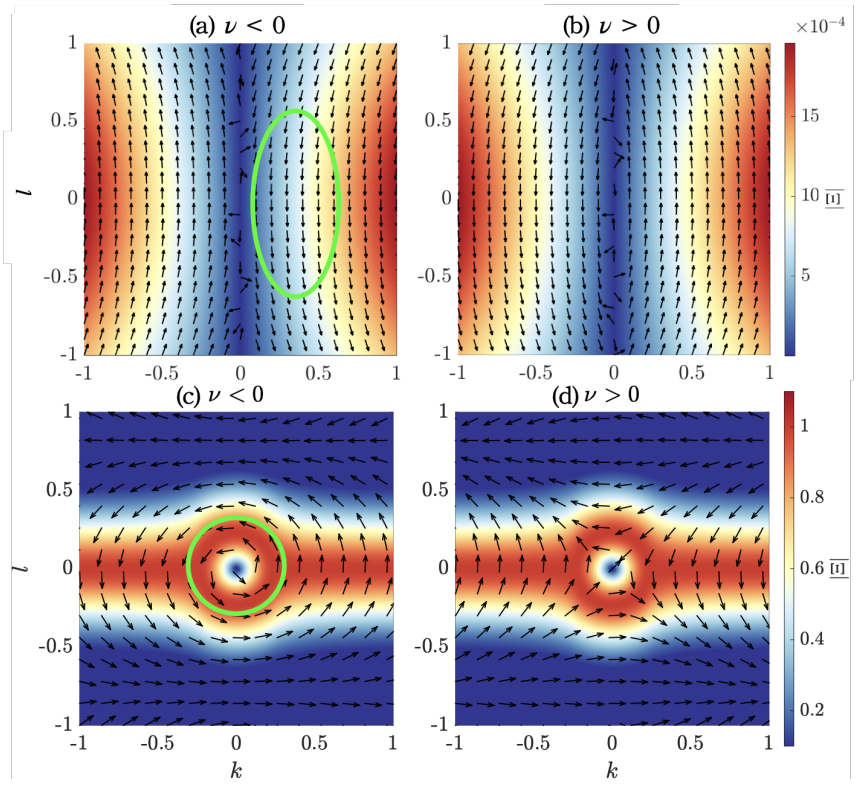

Figure 5.2: Theoretical calculation of the cross-correlation $\Xi(k,\ell)$ for normal modes at different frequencies. The color bar represents the magnitude of Ξ and arrows show the phase of its complex-value. The low-frequency planetary waves have a domain wall at $k = 0$ and are topologically trivial. Note that the winding number of the high-frequency Poincaré-gravity waves (bottom figures) depends on the sign of the frequency.

Representing the phase of Ξ with an arrow makes these patterns evident as shown

in Figure 5.2. In Delplace et al. [2017] and many subsequent papers, linearized wave equations have been characterized in terms of the topological Chern number. However the Chern number has several disadvantages. First, in contrast to systems on spatial lattices (where the Chern number was first applied), for continuous systems the Chern number need not be integer and its value depends on how an integral over the Berry curvature is regularized at high wavevectors. This ambiguity can sometimes be avoided Delplace et al. [2017] if sufficient care is taken but is more of a mathematical problem than a physical one because at small scales dissipation becomes important and ultimately at the smallest scales the fluid description must be replaced by discrete molecular dynamics. In any case the ambiguity does not arise for the winding number which is determined at finite wavevectors. Second, it is unclear how to extend the Chern number to systems with dissipation, driving, or nonlinearities – all properties of geophysical fluids. Finally it is difficult to compute the Chern number from observations or simulations because it involves an integral of the Berry curvature over wavevector space. We note that the winding number has recently been utilized in a number of different contexts including active optical media.

5.3 Method

5.3.1 Data

In order to investigate the topology of the Poincaré waves in the observations, the velocity field and geopotential height variable (u, v, h) has to satisfy several conditions. First, it has to be away from the equator so that the the Coriolis force is large enough to influence the wave activity, and the signal of the equatorial Kelvin wave and Rossby waves are small enough. Second, the fluid needs to be stratified to apply the shallow water equation, so we need to avoid lower troposphere where convection occurs a lot. Third, the time resolution should be high enough to resolve the signal

with frequency of 1-2 cycles per day (CPD).

Inspired by Pahlavan et al. [2021] who diagnosed the equatorial Kelvin and Yanai waves as well as Poincaré waves signal in spectral analysis of the ERA5 data in the stratosphere, we use the ERA5 reanalysis data [Hersbach et al., 2020] at the 50hPa level to avoid the influence from convection. We select 4 time windows per day from the hourly data in pressure levels in order to diagnose the Poincaré waves of 1-2 CPD frequency. The data has a time duration from 2017 to 2020, and spatial range from 25°N to 65°N across all longitudes with horizontal resolution of 0.25°.

5.3.2 Data Processing

To observe the topological features on the stratosphere signals, we first reduce the resolution of the data to 1° in latitude and 2.5° in longitude. The Poincaré waves are the long waves in the horizontal direction, so it is safe to reduce the horizontal resolution and still preserve the waves properties.

After that, we want to preserve only the high-frequency signals and remove the seasonal signals from the data. We achieve this by first applying a low-pass boxcar filter with a window of 182 days (half year) in the time dimension, then subtract the low-frequency signals.

This process as a whole acts as a high-pass filter, and it only preserves the high-frequency signals. The Poincaré waves can be observed when frequency is close to the Coriolis frequency, which in the region we select (25°N - 65°N), the average approximation is $f_0 = 2\Omega \sin(\phi) = 1.42$ CPD, which ϕ=45°N is taken as the average latitude, and Ω =1 CPD is the frequency in the unit of cycles per day.

Then we do a very similar process as Wheeler and Kiladis [1999] by cutting the time series into segments of 128 days with 96 days of overlaps. We cut the entire time series into small segments because the waves that we are interested about has a period shorter than 128 days, so it is safe to analyze the shorter time series. In

addition, by adding up the spectrum from different segments, we can increase the statistical significance to the waves analysis. We remove the linear trends from each segment, and then we taper the latitudinal and time dimensions of the data to avoid the edge effect from the Fourier transform. The tapering window we selected is the Tukey window with α=0.5 [Prabhu, 2014].

$$\begin{cases} \nu[n] = \frac{1}{2}[1 - \cos\frac{2\pi n}{\alpha N}], & 0 \leq n \leq \frac{\alpha N}{2} \\ \nu[n] = 1, & \frac{\alpha N}{2} \leq n \leq \frac{N}{2} \\ \nu[N-n] = \nu[n], & \frac{N}{2} \leq n \leq N \end{cases} \tag{5.7}$$

This is a cosine-tapered window with the cosine lobe of width N/4 in both ends and a rectangular window in the center with the width of N/2, in which N is the number of data in the time dimension. The tapering process can avoid leakage in the Fourier transform in the next step.

After the data has been pre-processed, we perform a 3-dimensional complex Fourier transform on both the geopotential height (h) and the meridional wind (v), so that we can observe the data in the frequency-wavevector space.

$$\mathcal{F}(k, \ell, \nu) = \iiint f(x, y, t) e^{i(kx + \ell y - \nu t)} dx dy dt \tag{5.8}$$

Then we multiply the conjugate of v with h and arrive at a 3-dimensional gauge-invariant complex number Ξ on the frequency - zonal wavenumber - meridional wavenumber space. We select a specific frequency so then the data is now a 2-D complex data in the k-ℓ space and can be visualized. We then apply a 2-D moving Gaussian filter to accumulate statistics over a range of wavevectors, in order to improve the statistical significance. This Gaussian window has the same size as the data with σ=1.5.

$$\mathcal{G}(k,\ell) = \frac{1}{2\pi\sigma^2} e^{-\frac{k^2+\ell^2}{2\sigma^2}} \tag{5.9}$$

Finally we visualize the spectrum and phase of the result in zonal wavenumber - meridional wavenumber space.

5.4 Topology of Stratospheric Waves

To look at the similar pattern as Fig. 5.1 from a vertical section, we calculate the 3-dimensional spectrum of v and h separately, average over the meridional wavenumber (ℓ) dimension, and plot the spectrum of magnitude in zonal wavenumber (k) - frequency (ν) space (Fig. 5.3). We can find from the spectrum a cluster of bowl-shaped signal away from the zero-frequency area, which represents the signal that satisfies the dispersion relationship of the Poincaré waves. The strength of signals is slightly different in the meridional wind and geopotential height, but in the distribution in k-ν space, they both have a gap with the strong signal at zero 0 frequency, which can be explained by the eigenvalues of non-zero angular frequency: $\omega = \sqrt{f_0^2 + gH(k^2+\ell^2)}$. The gap represents a phase singularity property that the signal can not continuously distribute in the gap between different eigenmodes. We note that there is a strong signal at $\nu = 1$ CPD, which is the signal of diurnal cycle.

The topological property can be shown more clearly from the phase distribution in the k-ℓ space. In our simulation results (Fig. 5.2), we expect that in the Poincaré mode, there will be a vortex pattern with the negative frequency and a anti-vortex pattern with the positive frequency. In the center of the vortex / anti-vortex, the magnitude of the signal will be drop because of the lack of phase singularity. While in the planetary waves mode, there will be a wall at k=0 that separates the different directions of the vertically pointing phases. In the analysis of the ERA5 data, we observe the similar patterns (Fig. 5.4). We choose different values of ν in order to

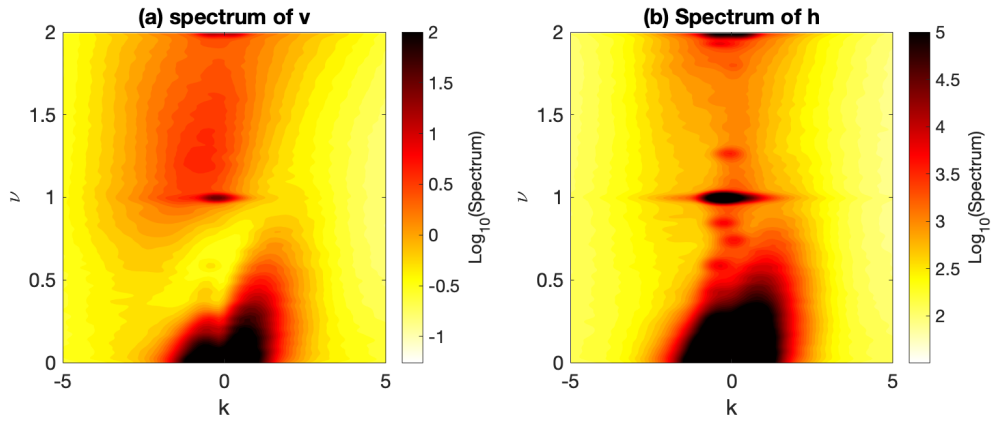

Figure 5.3: Spectrum of meridional velocity (v) and geopotential height (h) in the zonal wavenumber (k) - frequency (ν) space. The height of the variables is 50hPa, and the latitude is from 25°N to 65°N. Color contours are the Log10 of the spectrum. ν has the unit of cycles per day (CPD), and k has the unit of cycles per circumference.

show the cross sections for different layers in Fig. 5.1. $\nu = -0.1$ CPD represents the pattern for the Rossby waves which have a near-zero frequency. It is consistent with the simulation that it has oppositely pointing phase in the ℓ direction with positive and negative values of k. The Poincaré waves patterns are in the frequencies with absolute values larger than 1.4 CPD, where the phase forms a vortex around the original point, and the magnitude of the signal is small at the center of the vortex. The figures for frequency values in between show the phase pattern at the gap between these two wave systems, where you can see the transition from the Rossby wave pattern to the Poincaré wave pattern. The amplitude of the spectrum is strong near the region where $k = 0$ and $\ell = 0$, but it weakens quickly away from the origin point, which tells us that the long waves are the dominant signals in the data we explored.

When we look at the spectrum and phase relationship in the troposphere, we can still find the similar pattern for Rossby waves but the vortex pattern for Poincaré waves no longer exist (Fig. 5.5). This is because in the troposphere, with all the convection and moist processes, the atmosphere is no longer nicely stratified and the Poincaré waves are no longer the dominant signals. Although the vortex patterns

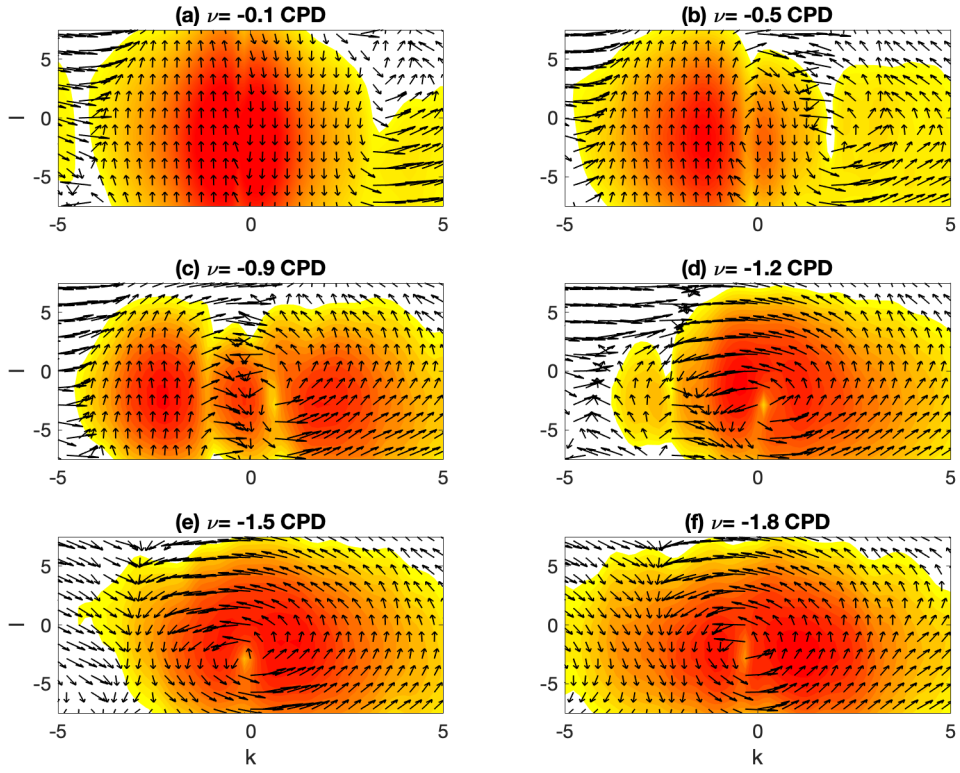

Figure 5.4: Plot of Ξ obtained from ERA5 data, 25°N-65°N, 50hPa. Subplots represent different frequencies (ν, unit: CPD). Color contours represent strength of signal (magnitude of Ξ), and arrows represent the phase of Ξ.

no longer preserve, we do noticed two other phenomena. Firstly, when ν=-1.5 and -1.8, the spectrum has the strongest signals with the negative value of k, which indicates that the dominant signal is the westward propagating wave. The stronger westward propagating signal is consistent with many of the previous analysis showing a stronger signal in the negative k region compared with the positive k region [e.g., Wheeler and Kiladis, 1999]. Secondly, the area with strong signal spans a larger range of k and ℓ. This result is consistent with the result from Kiladis (2022) that the dispersion relationship of Kelvin waves and Poincareé waves show a steeper slope when at the higher altitude atmosphere. Therefore, when we observe the signals from the troposphere, the dispersion slope for ν and k is much flatter, so the edge slope for the bowl-shape pattern for Poincaré waves (Fig. 5.1) is also wider and flatter. As

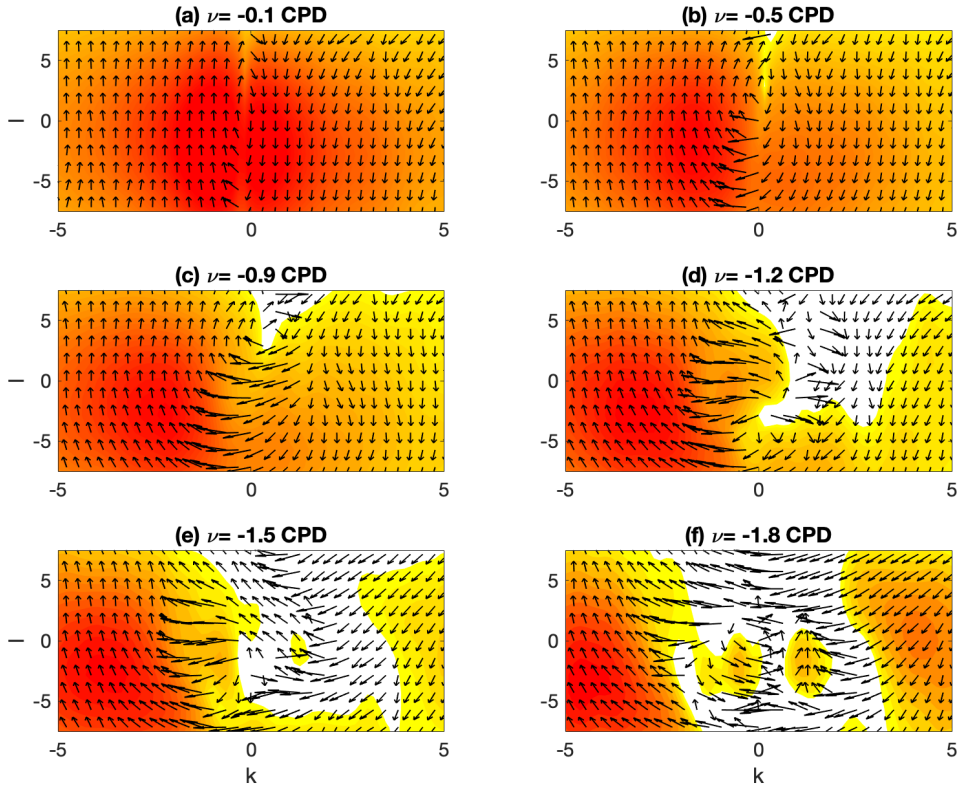

Figure 5.5: Same as Fig.5.4, but for the altitude of 850hPa.

a result, when we take a slice from a specific frequency, there will be a larger area contained within the Poincaré wave pattern in the troposphere, where we can observe the strong signals.

5.5 Conclusion

In this paper we demonstrated that Poincaré-gravity waves in the stratosphere have the non-trivial topological signature expected from theory. The Poincaré-gravity modes of the shallow water equations on the f-plane have non-zero winding number in wavevector space. By contrast planetary waves show only trivial topology. Using the ERA5 reanalysis data at 50 hPa pressure level, we find the expected winding

numbers of ± 1 at higher frequency and 0 at low frequencies. The winding number of the Poincaré waves changes by 2 passing from the Northern to Southern hemispheres, and the principle of bulk-interface correspondence predicts the existence of two localized modes at the equator. These are the Kelvin and Yanai waves that have been previously seen in observation.

The mathematics of topology has great predictive power because it makes complicated problems simple by focusing on robust features. The topology we investigate here plays out in frequency-wavevector space, rather than in real space. Topology in this setting is a new tool for climate science that is relatively immune to background noise as the distinct signatures of topology found in ERA5 observations of Poincaré-gravity waves qualitatively distinguishes them from planetary waves. Future application to emergent wavelike phenomena such as the Madden-Julian Oscillation may be envisioned.

Chapter 6

Conclusion

6.1 Summary

The main goal of this thesis is to improve our understanding of the interaction between the mountain and the climate system, and to understand the climate waves from the topology concepts. From Chapter 2 to 4, I use climate models to understand how the Andes influence the climate system on the tropical Pacific as well as the South America. In Chapter 5, I discover topological patterns in the stratosphere Poincaré waves.

Key findings and highlights for each chapter are listed below:

- In Chapter 2, we use slab-ocean model to show that the Andes is underestimated in the low-resolution global climate models, resulting in insufficient blocking for the mid-latitude westerlies from the Pacific. The maximum instead of the mean elevation is a better representation of the blocking effect of the Andes in the climate models, which lowers the eastern Pacific SST and inhibits south Pacific precipitation. The key finding of this chapter is Andes influences the tropical Pacific climate by blocking the mid-latitude westerlies and force an equatorward turning, so it has to be high enough in the climate models to serve as an effective barrier. There are two highlights in this chapter. First, we quantify the mechanism of how the higher Andes setting lowers the SST for different regions, and we find that the coastal eastern Pacific is mainly from radiative cooling, while the central Pacific is mainly from evaporative cooling. Secondly, we run a series of sensitivity runs and find that the model's default setting of the Andes only has en effective height of 2 km, while the Higher Andes setting captures the effective height of 4 km.

- In Chapter 3, we continue the experiment of elevating the height of the Andes, but instead we use the atmosphere-ocean coupled model and to see how it changes the ENSO cycle. The key finding is that the compared with the default

topography setting, the higher Andes setting can not only regulate the tropical Pacific climate mean state by lowering the eastern Pacific SST, but also change the variations by reducing the ENSO amplitude, increasing ENSO asymmetry and producing more irregular cycles, which are more similar to the observations. A highlight of this chapter is that when we do the mechanism analysis for the change in ENSO cycle, we add the significance analysis in our results. This significance analysis is lacked in many of the previous studies, but we find that it is very necessary because the uncertainty is very large, so the interpretation of the results will be different considering this large uncertainty.

- In Chapter 4, we use the high-resolution climate model and remove the Andes to understand the mechanism of the extreme precipitation on the La Plata basin changes compared with the default topography. The key finding of this project is that the Andes influences the precipitation seasonal cycle of La Plata basin, and the extreme precipitation strength reduces by about 50% without the Andes. The highlight of this research is that it was generally thought that the severe storm occurs in October because the moisture supply is strongest, but in our research, we find that this is not correct. The reason for October storm is because the vertical wind shear is strongest in October, providing a large-scale condition that is best for perturbation. With the sufficient moisture supply directed by the Andes, the severe storms occur in October.

- In Chapter 5, we analyze the ERA5 stratosphere data, and diagnose the non-trivial topology pattern in the Poincaré waves that matches the theoretical simulations. The key finding of this project is that for the first time we use the climate data to prove the theory introduced in Delplace et al. [2017], which implies topology can be applied to the future studies in climate waves. The highlight of this project is that the non-trivial topology is not obvious in the real

space but has to be observed in the wavevector space. The topology properties in the wavevector space is not sensitive to the background noise, which makes it a useful tool for the wave studies.

6.2 Future work

6.2.1 The Andes and the transient climate sensitivity

For the continuation of the study about how the Andes influences the climate system, I also want to study how the Andes influences the transient global climate sensitivity. Kosaka and Xie [2013] shows that the global mean temperature is closely related to the eastern Pacific SST. Since the Higher Andes setting can decrease the eastern Pacific SST, we hypothesize that by changing the topography, the global mean surface temperature will also be influenced.

Given that the Higher Andes setting can help provide a more accurate simulation of the present day climate, it is likely that it can provide a more reliable future climate projection as well. Instead of using a global climate model with constant forcing, in this study we will use an atmosphere-ocean coupled model with high-emissions scenario (RCP 8.5) setting, and explore how the different settings of the Andes will influence the global climate sensitivity.

There are several questions to be studied in this experiment. First is the global mean temperature response. We will first analyze by 2100, will the global mean surface temperature be the same or different in the different Andes setting simulations. Second is the warming pattern spatial distribution. Long et al. [2014] find that the eastern and western Pacific are responding at different paces to global warming. Since with the higher Andes setting, the Pacific east-west SST gradient becomes larger, it will also likely to change this fast and slow response at the tropical Pacific. Third is the precipitation distribution. Held and Soden [2006] explains the 'wet gets wetter,

dry gets dryer' pattern under global warming. The higher Andes setting changes the atmosphere circulation as well as the hydrology cycle, and we are curious how the global precipitation pattern will the different compared with default topography.

By exploring the answer to these questions, we will be able to complete the study of the Andes and the climate system. Based on the first two studies that provided a foundation for the correct representation of the Andes topography, this study will take advantage of the setting and improve the reliability for the future climate projection.

6.2.2 Why La Plata basin has the strongest storms

Following the study about the Andes and the South America extreme storms, there are also other factors to be examined. In this study, we answered the question about why October has the strongest convection by analyzing the vertical wind shear, but there remains two additional questions about formation of these storms.

The first factor to be examined is the source of the moisture. Many of the precipitation centers gain their moisture from the ocean [e.g., Dar et al., 2021]. La Plata basin receive most of the moisture from the Amazon forest [van der Ent et al., 2010]. In this study, we want to examine by how much the moisture from the Amazon forest contributes to these severe storms. We will examine this question by turning off the evapotranspiration of the Amazon forest in the climate models, and see if the moisture from the tropical Atlantic ocean can still create the severe storms over La Plata basin, and how do the intensity and frequency of these severe storms change.

The second factor is the local condition over the La Plata basin. Houze Jr. [2012] shows that the strong westerlies above the South America Low-Level Jet (SALLJ) provides a capping effect that allows the accumulation of instability with surface latent and sensible heat fluxes, and when the instability releases, intense convection occurs. Our first hypothesis is that the surface roughness or the local elevation of La Plata basin triggers the release of the instability, resulting in severe convection. In

the meanwhile, Wu and Lee [2019] shows that the surface vegetation type can also change the scale of convection. We will also examine by how much does the local vegetation contributes to these severe storms.

Bibliography

Esteban Abellán, Shayne McGregor, and Matthew H. England. Analysis of the Southward Wind Shift of ENSO in CMIP5 Models. *Journal of Climate*, 30(7):2415–2435, April 2017. ISSN 0894-8755, 1520-0442. doi: 10.1175/JCLI-D-16-0326.1. URL https://journals.ametsoc.org/view/journals/clim/30/7/jcli-d-16-0326.1.xml.

Ori Adam, Tobias Bischoff, and Tapio Schneider. Seasonal and Interannual Variations of the Energy Flux Equator and ITCZ. Part II: Zonally Varying Shifts of the ITCZ. *J. Climate*, 29(20):7281–7293, October 2016. ISSN 0894-8755, 1520-0442. doi: 10.1175/JCLI-D-15-0710.1. URL http://journals.ametsoc.org/doi/10.1175/JCLI-D-15-0710.1.

Ori Adam, Tapio Schneider, and Florent Brient. Regional and seasonal variations of the double-ITCZ bias in CMIP5 models. *Clim Dyn*, 51(1-2):101–117, July 2018. ISSN 0930-7575, 1432-0894. doi: 10.1007/s00382-017-3909-1. URL http://link.springer.com/10.1007/s00382-017-3909-1.

Alistair Adcroft. Representation of topography by porous barriers and objective interpolation of topographic data. *Ocean Modelling*, 67:13–27, July 2013. ISSN 14635003. doi: 10.1016/j.ocemod.2013.03.002. URL https://linkinghub.elsevier.com/retrieve/pii/S1463500313000425.

Robert F. Adler, George J. Huffman, Alfred Chang, Ralph Ferraro, Ping-Ping

Xie, John Janowiak, Bruno Rudolf, Udo Schneider, Scott Curtis, David Bolvin, Arnold Gruber, Joel Susskind, Philip Arkin, and Eric Nelkin. The Version-2 Global Precipitation Climatology Project (GPCP) Monthly Precipitation Analysis (1979–Present). *Journal of Hydrometeorology*, 4(6):1147–1167, December 2003. ISSN 1525-7541, 1525-755X. doi: 10.1175/1525-7541(2003)004⟨1147:TVGPCP⟩2.0.CO;2. URL https://journals.ametsoc.org/view/journals/hydr/4/6/1525-7541_2003_004_1147_tvgpcp_2_0_co_2.xml.

Soon-Il An, Eli Tziperman, Yuko M. Okumura, and Tim Li. ENSO Irregularity and Asymmetry. In *El Niño Southern Oscillation in a Changing Climate*, pages 153–172. American Geophysical Union (AGU), 2020. ISBN 978-1-119-54816-4. doi: 10.1002/9781119548164.ch7. URL https://agupubs.onlinelibrary.wiley.com/doi/abs/10.1002/9781119548164.ch7.

Kentaro Ando and Michael J. McPhaden. Variability of surface layer hydrography in the tropical Pacific Ocean. *Journal of Geophysical Research: Oceans*, 102(C10):23063–23078, 1997. ISSN 2156-2202. doi: 10.1029/97JC01443. URL https://onlinelibrary.wiley.com/doi/abs/10.1029/97JC01443. _eprint: https://onlinelibrary.wiley.com/doi/pdf/10.1029/97JC01443.

A. R. Atwood, D. S. Battisti, A. T. Wittenberg, W. H. G. Roberts, and D. J. Vimont. Characterizing unforced multi-decadal variability of ENSO: a case study with the GFDL CM2.1 coupled GCM. *Clim Dyn*, 49(7):2845–2862, October 2017. ISSN 1432-0894. doi: 10.1007/s00382-016-3477-9. URL https://doi.org/10.1007/s00382-016-3477-9.

Andrea Bastianin, Alessandro Lanza, and Matteo Manera. Economic impacts of El Niño southern oscillation: evidence from the Colombian coffee market. *Agricultural Economics*, 49(5):623–633, 2018. ISSN 1574-0862. doi: 10.1111/agec.12447. URL https://onlinelibrary.wiley.com/doi/abs/10.1111/agec.12447.

David S. Battisti. Dynamics and Thermodynamics of a Warming Event in a Coupled Tropical Atmosphere–Ocean Model. *Journal of the Atmospheric Sciences*, 45(20):2889–2919, October 1988. ISSN 0022-4928, 1520-0469. doi: 10.1175/1520-0469(1988)045⟨2889:DATOAW⟩2.0.CO;2. URL https://journals.ametsoc.org/view/journals/atsc/45/20/1520-0469_1988_045_2889_datoaw_2_0_co_2.xml. Publisher: American Meteorological Society Section: Journal of the Atmospheric Sciences.

Tobias Bayr, Mojib Latif, Dietmar Dommenget, Christian Wengel, Jan Harlaß, and Wonsun Park. Mean-state dependence of ENSO atmospheric feedbacks in climate models. *Clim Dyn*, 50(9):3171–3194, May 2018. ISSN 1432-0894. doi: 10.1007/s00382-017-3799-2. URL https://doi.org/10.1007/s00382-017-3799-2.

H. Bellenger, E. Guilyardi, J. Leloup, M. Lengaigne, and J. Vialard. ENSO representation in climate models: from CMIP3 to CMIP5. *Clim Dyn*, 42(7):1999–2018, April 2014. ISSN 1432-0894. doi: 10.1007/s00382-013-1783-z. URL https://doi.org/10.1007/s00382-013-1783-z.

Tobias Bischoff and Tapio Schneider. The Equatorial Energy Balance, ITCZ Position, and Double-ITCZ Bifurcations. *J. Climate*, 29(8):2997–3013, April 2016. ISSN 0894-8755, 1520-0442. doi: 10.1175/JCLI-D-15-0328.1. URL http://journals.ametsoc.org/doi/10.1175/JCLI-D-15-0328.1.

J. Bjerknes. ATMOSPHERIC ECONNECTIONS FROM THE EQUATORIAL PACIFIC. *Monthly Weather Review*, 97(3):163–172, March 1969. ISSN 1520-0493, 0027-0644. doi: 10.1175/1520-0493(1969)097⟨0163:ATFTEP⟩2.3.CO;2. URL https://journals.ametsoc.org/view/journals/mwre/97/3/1520-0493_1969_097_0163_atftep_2_3_co_2.xml.

P. A. Bogenschutz, A. Gettelman, C. Hannay, V. E. Larson, R. B. Neale, C. Craig,

and C.-C. Chen. The path to CAM6: coupled simulations with CAM5.4 and CAM5.5. *Geoscientific Model Development*, 11(1):235–255, 2018. doi: 10.5194/gmd-11-235-2018. URL https://www.geosci-model-dev.net/11/235/2018/.

Sandrine Bony. Marine boundary layer clouds at the heart of tropical cloud feedback uncertainties in climate models. *Geophys. Res. Lett.*, 32(20):L20806, 2005. ISSN 0094-8276. doi: 10.1029/2005GL023851. URL http://doi.wiley.com/10.1029/2005GL023851.

William R. Boos and Robert L. Korty. Regional energy budget control of the intertropical convergence zone and application to mid-Holocene rainfall. *Nature Geosci*, 9(12):892–897, December 2016. ISSN 1752-0894, 1752-0908. doi: 10.1038/ngeo2833. URL http://www.nature.com/articles/ngeo2833.

William R. Boos and Zhiming Kuang. Dominant control of the South Asian monsoon by orographic insulation versus plateau heating. *Nature*, 463(7278):218–222, January 2010. ISSN 1476-4687. doi: 10.1038/nature08707. URL https://www.nature.com/articles/nature08707.

Josephine R. Brown, Chris M. Brierley, Soon-Il An, Maria-Vittoria Guarino, Samantha Stevenson, Charles J. R. Williams, Qiong Zhang, Anni Zhao, Ayako Abe-Ouchi, Pascale Braconnot, Esther C. Brady, Deepak Chandan, Roberta D'Agostino, Chuncheng Guo, Allegra N. LeGrande, Gerrit Lohmann, Polina A. Morozova, Rumi Ohgaito, Ryouta O'ishi, Bette L. Otto-Bliesner, W. Richard Peltier, Xiaoxu Shi, Louise Sime, Evgeny M. Volodin, Zhongshi Zhang, and Weipeng Zheng. Comparison of past and future simulations of ENSO in CMIP5/PMIP3 and CMIP6/PMIP4 models. *Climate of the Past*, 16(5):1777–1805, September 2020. ISSN 1814-9324. doi: 10.5194/cp-16-1777-2020. URL https://cp.copernicus.org/articles/16/1777/2020/.

Natalie J. Burls, Leslie Muir, Emmanuel M. Vincent, and Alexey Fedorov. Extra-tropical origin of equatorial Pacific cold bias in climate models with links to cloud albedo. *Clim Dyn*, 49(5):2093–2113, September 2017. ISSN 1432-0894. doi: 10.1007/s00382-016-3435-6. URL https://doi.org/10.1007/s00382-016-3435-6.

Wenju Cai, Guojian Wang, Boris Dewitte, Lixin Wu, Agus Santoso, Ken Takahashi, Yun Yang, Aude Carréric, and Michael J. McPhaden. Increased variability of eastern Pacific El Niño under greenhouse warming. *Nature*, 564(7735):201–206, December 2018. ISSN 1476-4687. doi: 10.1038/s41586-018-0776-9. URL https://www.nature.com/articles/s41586-018-0776-9.

Wenju Cai, Agus Santoso, Matthew Collins, Boris Dewitte, Christina Karamperidou, Jong-Seong Kug, Matthieu Lengaigne, Michael J. McPhaden, Malte F. Stuecker, Andréa S. Taschetto, Axel Timmermann, Lixin Wu, Sang-Wook Yeh, Guojian Wang, Benjamin Ng, Fan Jia, Yun Yang, Jun Ying, Xiao-Tong Zheng, Tobias Bayr, Josephine R. Brown, Antonietta Capotondi, Kim M. Cobb, Bolan Gan, Tao Geng, Yoo-Geun Ham, Fei-Fei Jin, Hyun-Su Jo, Xichen Li, Xiaopei Lin, Shayne McGregor, Jae-Heung Park, Karl Stein, Kai Yang, Li Zhang, and Wenxiu Zhong. Changing El Niño–Southern Oscillation in a warming climate. *Nat Rev Earth Environ*, 2 (9):628–644, September 2021. ISSN 2662-138X. doi: 10.1038/s43017-021-00199-z. URL https://www.nature.com/articles/s43017-021-00199-z.

Mark A. Cane and Stephen E. Zebiak. A Theory for El Niño and the Southern Oscillation. *Science*, 228(4703):1085–1087, May 1985. ISSN 0036-8075, 1095-9203. doi: 10.1126/science.228.4703.1085. URL https://science.sciencemag.org/content/228/4703/1085.

Wilmar L. Cerón, Mary T. Kayano, Rita V. Andreoli, Alvaro Avila-Diaz, Irma Ayes, Edmilson D. Freitas, Jorge A. Martins, and Rodrigo A. F. Souza. Recent intensification of extreme precipitation events in the La Plata Basin in

Southern South America (1981–2018). *Atmospheric Research*, 249:105299, February 2021. ISSN 0169-8095. doi: 10.1016/j.atmosres.2020.105299. URL https://www.sciencedirect.com/science/article/pii/S0169809520312369.

Mat Collins, Soon-Il An, Wenju Cai, Alexandre Ganachaud, Eric Guilyardi, Fei-Fei Jin, Markus Jochum, Matthieu Lengaigne, Scott Power, Axel Timmermann, and et al. The impact of global warming on the tropical Pacific Ocean and El Niño. *Nature Geoscience*, 3(6):391–397, May 2010. ISSN 1752-0908. doi: 10.1038/ngeo868. URL http://dx.doi.org/10.1038/ngeo868. Publisher: Springer Nature.

Ying Dai, Steven B. Feldstein, Benkui Tan, and Sukyoung Lee. Formation Mechanisms of the Pacific–North American Teleconnection with and without Its Canonical Tropical Convection Pattern. *Journal of Climate*, 30(9):3139–3155, May 2017. ISSN 1520-0442. doi: 10.1175/jcli-d-16-0411.1. URL http://dx.doi.org/10.1175/JCLI-D-16-0411.1. Publisher: American Meteorological Society.

Shaakir Shabir Dar, Prosenjit Ghosh, and Claude Hillaire-Marcel. Convection, Terrestrial Recycling and Oceanic Moisture Regulate the Isotopic Composition of Precipitation at Srinagar, Kashmir. *Journal of Geophysical Research: Atmospheres*, 126(7):e2020JD032853, 2021. ISSN 2169-8996. doi: 10.1029/2020JD032853. URL https://onlinelibrary.wiley.com/doi/abs/10.1029/2020JD032853. _eprint: https://onlinelibrary.wiley.com/doi/pdf/10.1029/2020JD032853.

Pierre Delplace, J. B. Marston, and Antoine Venaille. Topological origin of equatorial waves. *Science*, 358(6366):1075–1077, November 2017. doi: 10.1126/science.aan8819. URL https://www.science.org/doi/full/10.1126/science.aan8819.

Dietmar Dommenget. The slab ocean El Niño: SLAB OCEAN EL NIÑO. *Geo-*

phys. Res. Lett., 37(20):n/a–n/a, October 2010. ISSN 00948276. doi: 10.1029/2010GL044888. URL http://doi.wiley.com/10.1029/2010GL044888.

Dietmar Dommenget, Tobias Bayr, and Claudia Frauen. Analysis of the non-linearity in the pattern and time evolution of El Niño southern oscillation. *Clim Dyn*, 40 (11):2825–2847, June 2013. ISSN 1432-0894. doi: 10.1007/s00382-012-1475-0. URL https://doi.org/10.1007/s00382-012-1475-0.

Charles A. Doswell III, Gregory W. Carbin, and Harold E. Brooks. The tornadoes of spring 2011 in the USA: an historical perspective. *Weather*, 67(4):88–94, 2012. ISSN 1477-8696. doi: 10.1002/wea.1902. URL https://onlinelibrary.wiley.com/doi/abs/10.1002/wea.1902. _eprint: https://onlinelibrary.wiley.com/doi/pdf/10.1002/wea.1902.

Jhan Carlo Espinoza, René Garreaud, Germán Poveda, Paola A. Arias, Jorge Molina-Carpio, Mariano Masiokas, Maximiliano Viale, and Lucia Scaff. Hydroclimate of the Andes Part I: Main Climatic Features. *Frontiers in Earth Science*, 8, 2020. ISSN 2296-6463. URL https://www.frontiersin.org/articles/10.3389/feart.2020.00064.

Keyan Fang, Qichao Yao, Zhengtang Guo, Ben Zheng, Jianhua Du, Fangzhong Qi, Ping Yan, Jie Li, Tinghai Ou, Jane Liu, Maosheng He, and Valerie Trouet. ENSO modulates wildfire activity in China. *Nature Communications*, 12(1):1764, March 2021. ISSN 2041-1723. doi: 10.1038/s41467-021-21988-6. URL https://www.nature.com/articles/s41467-021-21988-6.

J Thomas Farrar. Observations of the dispersion characteristics and meridional sea level structure of equatorial waves in the Pacific Ocean. *Journal of physical oceanography*, 38(8):1669–1689, 2008. doi: 10.1175/2007JPO3890.1. URL https://doi.org/10.1175/2007JPO3890.1.

Alexey V. Fedorov and S. George Philander. Is El Niño Changing? *Science*, 288(5473):1997–2002, June 2000. ISSN 0036-8075, 1095-9203. doi: 10.1126/science.288.5473.1997. URL https://science.sciencemag.org/content/288/5473/1997.

Alexey V Fedorov, Jaclyn N Brown, and J Steele. Equatorial waves. 2009. Publisher: Academic Press.

Ran Feng and Christopher J. Poulsen. Andean elevation control on tropical Pacific climate and ENSO: Andean uplift and tropical climate. *Paleoceanography*, 29(8): 795–809, August 2014. ISSN 08838305. doi: 10.1002/2014PA002640. URL http://doi.wiley.com/10.1002/2014PA002640.

Augusto J. Pereira Filho, Richard E. Carbone, and John D. Tuttle. Convective Rainfall Systems in the La Plata Basin. *Atmospheric and Climate Sciences*, 4(4): 757–778, August 2014. doi: 10.4236/acs.2014.44068. URL http://www.scirp.org/Journal/Paperabs.aspx?paperid=51127. Number: 4 Publisher: Scientific Research Publishing.

B. Fox-Kemper, Scott $øverline\textrmBachman$, Brodie $øverline\textrmPearson$, and Scott $øverline\textrmReckinger$. Principles and Advances in Subgrid Modeling for Eddy-Rich Simulations. *CLIVAR Exchanges*, 19(2):42–46, July 2014. URL http://bit.ly/1qSMTzA.

Bart Geerts and Edward Linacre. *Climates and Weather Explained*. Routledge, London, October 1997. ISBN 978-0-203-04263-2. doi: 10.4324/9780203042632.

Peter R. Gent, Stephen G. Yeager, Richard B. Neale, Samuel Levis, and David A. Bailey. Improvements in a half degree atmosphere/land version of the CCSM. *Clim Dyn*, 34(6):819–833, May 2010. ISSN 0930-7575, 1432-0894.

doi: 10.1007/s00382-009-0614-8. URL http://link.springer.com/10.1007/s00382-009-0614-8.

Simon A. Good, Matthew J. Martin, and Nick A. Rayner. EN4: Quality controlled ocean temperature and salinity profiles and monthly objective analyses with uncertainty estimates. *Journal of Geophysical Research: Oceans*, 118(12): 6704–6716, 2013. ISSN 2169-9291. doi: 10.1002/2013JC009067. URL https://onlinelibrary.wiley.com/doi/abs/10.1002/2013JC009067.

Eric Guilyardi, Andrew Wittenberg, Alexey Fedorov, C. Collins, Antonietta Capotondi, Geert Jan Van Oldenborgh, and Tim Stockdale. Understanding El Niño in Ocean-Atmosphere General Circulation Models: Progress and Challenges. *Bulletin of the American Meteorological Society*, 90:325–340, March 2009. doi: 10.1175/2008BAMS2387.1.

Eric Guilyardi, Antonietta Capotondi, Matthieu Lengaigne, Sulian Thual, and Andrew T. Wittenberg. ENSO Modeling. In *El Niño Southern Oscillation in a Changing Climate*, pages 199–226. American Geophysical Union (AGU), 2020. ISBN 978-1-119-54816-4. doi: 10.1002/9781119548164.ch9. URL https://agupubs.onlinelibrary.wiley.com/doi/abs/10.1002/9781119548164.ch9.

Thomas WN Haine, Renske Gelderloos, Miguel A Jimenez-Urias, Ali H Siddiqui, Gerard Lemson, Dimitri Medvedev, Alex Szalay, Ryan P Abernathey, Mattia Almansi, and Christopher N Hill. Is Computational Oceanography Coming of Age? *Bulletin of the American Meteorological Society*, pages 1–33, 2021. doi: 10.1175/BAMS-D-20-0258.1.

D. E. Harrison and Gabriel A. Vecchi. Westerly Wind Events in the Tropical Pacific, 1986–95. *Journal of Climate*, 10(12):3131–3156, December 1997. ISSN 0894-8755, 1520-0442. doi: 10.1175/1520-0442(1997)010⟨3131:WWEITT⟩

2.0.CO;2. URL https://journals.ametsoc.org/view/journals/clim/10/12/1520-0442_1997_010_3131_wweitt_2.0.co_2.xml. Publisher: American Meteorological Society Section: Journal of Climate.

M. Z. Hasan and C. L. Kane. Colloquium: Topological insulators. *Rev. Mod. Phys.*, 82 (4):3045–3067, November 2010. doi: 10.1103/RevModPhys.82.3045. URL https://link.aps.org/doi/10.1103/RevModPhys.82.3045.

David A. Hasings, Paula K. Dunbar, Gerald M. Elphingstone, Mark Bootz, Hiroshi Murakami, Hiroshi Maruyama, Hiroshi Masaharu, Peter Holland, John Payne, Nevin A. Bryant, Thomas L Logan, J.-P. Muller, Gunter Schreier, and John S. MacDonald. The Global Land One-kilometer Base Elevation (GLOBE) Digital Elevation Model, Version 1.0., 1999. URL http://www.ngdc.noaa.gov/mgg/topo/globe.html).

David A. Hastings and Paula K. Dunbar. *Global Land One-kilometer Base Elevation (GLOBE) Digital Elevation Model, Documentation.* National Oceanic and Atmospheric Administration, National Geophysical Data Center, 325 Broadway, Boulder, Colorado 80303, U.S.A, volume 1.0 edition, 1999.

Jie He, Nathaniel C. Johnson, Gabriel A. Vecchi, Ben Kirtman, Andrew T. Wittenberg, and Stephan Sturm. Precipitation Sensitivity to Local Variations in Tropical Sea Surface Temperature. *Journal of Climate*, 31(22):9225–9238, November 2018. ISSN 0894-8755, 1520-0442. doi: 10.1175/JCLI-D-18-0262.1. URL https://journals.ametsoc.org/view/journals/clim/31/22/jcli-d-18-0262.1.xml.

Isaac M. Held and Brian J. Soden. Robust Responses of the Hydrological Cycle to Global Warming. *Journal of Climate*, 19(21):5686–5699, November 2006. ISSN 0894-8755, 1520-0442. doi: 10.1175/JCLI3990.1. URL https://journals.

ametsoc.org/view/journals/clim/19/21/jcli3990.1.xml. Publisher: American Meteorological Society Section: Journal of Climate.

Myrl Hendershott and Walter Munk. Tides. *Annual review of fluid mechanics*, 2(1): 205–224, 1970. Publisher: Annual Reviews 4139 El Camino Way, PO Box 10139, Palo Alto, CA 94303-0139, USA.

Hans Hersbach, Bill Bell, Paul Berrisford, Shoji Hirahara, András Horányi, Joaquín Muñoz-Sabater, Julien Nicolas, Carole Peubey, Raluca Radu, Dinand Schepers, Adrian Simmons, Cornel Soci, Saleh Abdalla, Xavier Abellan, Gianpaolo Balsamo, Peter Bechtold, Gionata Biavati, Jean Bidlot, Massimo Bonavita, Giovanna De Chiara, Per Dahlgren, Dick Dee, Michail Diamantakis, Rossana Dragani, Johannes Flemming, Richard Forbes, Manuel Fuentes, Alan Geer, Leo Haimberger, Sean Healy, Robin J. Hogan, Elías Hólm, Marta Janisková, Sarah Keeley, Patrick Laloyaux, Philippe Lopez, Cristina Lupu, Gabor Radnoti, Patricia de Rosnay, Iryna Rozum, Freja Vamborg, Sebastien Villaume, and Jean-Noël Thépaut. The ERA5 global reanalysis. *Quarterly Journal of the Royal Meteorological Society*, 146(730):1999–2049, 2020. ISSN 1477-870X. doi: 10.1002/qj.3803. URL https://onlinelibrary.wiley.com/doi/abs/10.1002/qj.3803.

Robert A. Houze Jr. Orographic effects on precipitating clouds. *Reviews of Geophysics*, 50(1), 2012. ISSN 1944-9208. doi: 10.1029/2011RG000365. URL https://onlinelibrary.wiley.com/doi/abs/10.1029/2011RG000365. _eprint: https://onlinelibrary.wiley.com/doi/pdf/10.1029/2011RG000365.

Shineng Hu and Alexey V. Fedorov. Cross-equatorial winds control El Niño diversity and change. *Nature Climate Change*, 8(9):798–802, September 2018. ISSN 1758-6798. doi: 10.1038/s41558-018-0248-0. URL https://www.nature.com/articles/s41558-018-0248-0.

James W. Hurrell, M. M. Holland, P. R. Gent, S. Ghan, Jennifer E. Kay, P. J. Kushner, J.-F. Lamarque, W. G. Large, D. Lawrence, K. Lindsay, W. H. Lipscomb, M. C. Long, N. Mahowald, D. R. Marsh, R. B. Neale, P. Rasch, S. Vavrus, M. Vertenstein, D. Bader, W. D. Collins, J. J. Hack, J. Kiehl, and S. Marshall. The Community Earth System Model: A Framework for Collaborative Research. *Bulletin of the American Meteorological Society*, 94(9):1339–1360, September 2013. doi: 10.1175/BAMS-D-12-00121.1. URL `https://journals.ametsoc.org/view/journals/bams/94/9/bams-d-12-00121.1.xml`.

Y.-T. Hwang and D. M. W. Frierson. Link between the double-Intertropical Convergence Zone problem and cloud biases over the Southern Ocean. *Proceedings of the National Academy of Sciences*, 110(13):4935–4940, March 2013. ISSN 0027-8424, 1091-6490. doi: 10.1073/pnas.1213302110. URL `http://www.pnas.org/cgi/doi/10.1073/pnas.1213302110`.

F.-F. Jin. Tropical Ocean-Atmosphere Interaction, the Pacific Cold Tongue, and the El Niño-Southern Oscillation. *Science*, 274(5284):76–78, October 1996. ISSN 0036-8075, 1095-9203. doi: 10.1126/science.274.5284.76. URL `https://science.sciencemag.org/content/274/5284/76`.

Fei-Fei Jin. An Equatorial Ocean Recharge Paradigm for ENSO. Part I: Conceptual Model. *Journal of the Atmospheric Sciences*, 54(7):811–829, April 1997a. ISSN 0022-4928, 1520-0469. doi: 10.1175/1520-0469(1997)054⟨0811:AEORPF⟩2.0.CO;2. URL `https://journals.ametsoc.org/view/journals/atsc/54/7/1520-0469_1997_054_0811_aeorpf_2.0.co_2.xml`.

Fei-Fei Jin. An Equatorial Ocean Recharge Paradigm for ENSO. Part II: A Stripped-Down Coupled Model. *Journal of the Atmospheric Sciences*, 54(7):830–847, April 1997b. ISSN 0022-4928, 1520-0469. doi: 10.1175/1520-0469(1997)054⟨0830:

AEORPF⟩2.0.CO;2. URL https://journals.ametsoc.org/view/journals/atsc/54/7/1520-0469_1997_054_0830_aeorpf_2.0.co_2.xml.

Fei-Fei Jin, Seon Tae Kim, and Luis Bejarano. A coupled-stability index for ENSO. *Geophysical Research Letters*, 33(23), 2006. ISSN 1944-8007. doi: https://doi.org/10.1029/2006GL027221. URL https://agupubs.onlinelibrary.wiley.com/doi/abs/10.1029/2006GL027221.

Fei-Fei Jin, Han-Ching Chen, Sen Zhao, Michiya Hayashi, Christina Karamperidou, Malte F. Stuecker, Ruihuang Xie, and Licheng Geng. Simple ENSO Models. In *El Niño Southern Oscillation in a Changing Climate*, pages 119–151. American Geophysical Union (AGU), 2020. ISBN 978-1-119-54816-4. doi: 10.1002/9781119548164.ch6. URL https://agupubs.onlinelibrary.wiley.com/doi/abs/10.1002/9781119548164.ch6.

C. Junquas, L. Li, C. S. Vera, H. Le Treut, and K. Takahashi. Influence of South America orography on summertime precipitation in Southeastern South America. *Clim Dyn*, 46(11):3941–3963, June 2016. ISSN 1432-0894. doi: 10.1007/s00382-015-2814-8. URL https://doi.org/10.1007/s00382-015-2814-8.

Christina Karamperidou, Malte F. Stuecker, Axel Timmermann, Kyung-Sook Yun, Sun-Seon Lee, Fei-Fei Jin, Agus Santoso, Michael J. McPhaden, and Wenju Cai. ENSO in a Changing Climate. In *El Niño Southern Oscillation in a Changing Climate*, pages 471–484. American Geophysical Union (AGU), 2020. ISBN 978-1-119-54816-4. doi: 10.1002/9781119548164.ch21. URL https://agupubs.onlinelibrary.wiley.com/doi/abs/10.1002/9781119548164.ch21.

Richard A. Keen. The Role of Cross-Equatorial Tropical Cyclone Pairs in the Southern Oscillation. *Monthly Weather Review*, 110(10):1405–1416, October 1982. ISSN 1520-0493, 0027-0644. doi: 10.1175/1520-0493(1982)110⟨1405:TROCET⟩2.

0.CO;2. URL https://journals.ametsoc.org/view/journals/mwre/110/10/1520-0493_1982_110_1405_trocet_2_0_co_2.xml. Publisher: American Meteorological Society Section: Monthly Weather Review.

William S. Kessler. EOF Representations of the Madden–Julian Oscillation and Its Connection with ENSO. *Journal of Climate*, 14(13):3055–3061, July 2001. ISSN 0894-8755, 1520-0442. doi: 10.1175/1520-0442(2001)014⟨3055:EROTMJ⟩2.0.CO;2. URL https://journals.ametsoc.org/view/journals/clim/14/13/1520-0442_2001_014_3055_erotmj_2.0.co_2.xml. Publisher: American Meteorological Society Section: Journal of Climate.

Daniel Keyser, Brian D. Schmidt, and Dean G. Duffy. A Technique for Representing Three-Dimensional Vertical Circulations in Baroclinic Disturbances. *Monthly Weather Review*, 117(11):2463–2494, 1989. doi: 10.1175/1520-0493(1989)117⟨2463:ATFRTD⟩2.0.CO;2. URL https://doi.org/10.1175/1520-0493(1989)117<2463:ATFRTD>2.0.CO;2. _eprint: https://doi.org/10.1175/1520-0493(1989)117<2463:ATFRTD>2.0.CO;2.

George N. Kiladis, Matthew C. Wheeler, Patrick T. Haertel, Katherine H. Straub, and Paul E. Roundy. Convectively coupled equatorial waves. *Reviews of Geophysics*, 47(2), 2009. ISSN 1944-9208. doi: 10.1029/2008RG000266. URL https://onlinelibrary.wiley.com/doi/abs/10.1029/2008RG000266.

Seon Tae Kim, Wenju Cai, Fei-Fei Jin, and Jin-Yi Yu. ENSO stability in coupled climate models and its association with mean state. *Clim Dyn*, 42(11):3313–3321, June 2014. ISSN 1432-0894. doi: 10.1007/s00382-013-1833-6. URL https://doi.org/10.1007/s00382-013-1833-6.

Akio Kitoh. ENSO modulation by mountain uplift. *Clim Dyn*, 28(7):781–796, June

2007. ISSN 1432-0894. doi: 10.1007/s00382-006-0209-6. URL https://doi.org/10.1007/s00382-006-0209-6.

Tsubasa Kohyama, Dennis L. Hartmann, and David S. Battisti. La Niña–like Mean-State Response to Global Warming and Potential Oceanic Roles. *Journal of Climate*, 30(11):4207–4225, June 2017. ISSN 0894-8755, 1520-0442. doi: 10.1175/JCLI-D-16-0441.1. URL https://journals.ametsoc.org/view/journals/clim/30/11/jcli-d-16-0441.1.xml.

Yu Kosaka and Shang-Ping Xie. Recent global-warming hiatus tied to equatorial Pacific surface cooling. *Nature*, 501(7467):403–407, September 2013. ISSN 0028-0836, 1476-4687. doi: 10.1038/nature12534. URL http://www.nature.com/articles/nature12534.

Christian Kummerow, William Barnes, Toshiaki Kozu, James Shiue, and Joanne Simpson. The Tropical Rainfall Measuring Mission (TRMM) Sensor Package. *Journal of Atmospheric and Oceanic Technology*, 15(3): 809–817, 1998. doi: 10.1175/1520-0426(1998)015⟨0809:TTRMMT⟩2.0.CO;2. URL https://doi.org/10.1175/1520-0426(1998)015<0809:TTRMMT>2.0.CO;2. _eprint: https://doi.org/10.1175/1520-0426(1998)015<0809:TTRMMT>2.0.CO;2.

Daniel Leathers, Brent Yarnal, and Michael Palecki. The Pacific/North American Teleconnection Pattern and United States Climate. Part I: Regional Temperature and Precipitation Associations. *Journal of Climate*, 4:517–528, 1991. doi: 10.1175/1520-0442(1991)004⟨0517:TPATPA⟩2.0.CO;2.

Jung-Eun Lee, Benjamin R. Lintner, C. Kevin Boyce, and Peter J. Lawrence. Land use change exacerbates tropical South American drought by sea surface temperature variability. *Geophysical Research Letters*, 38 (19), 2011. ISSN 1944-8007. doi: 10.1029/2011GL049066. URL

https://onlinelibrary.wiley.com/doi/abs/10.1029/2011GL049066. _eprint: https://onlinelibrary.wiley.com/doi/pdf/10.1029/2011GL049066.

Jung-Eun Lee. Understanding Neogene Oxygen Isotopes in the Southern Great Plains Using Isotope-Enabled General Circulation Model Simulations. *J. Geophys. Res. Atmos.*, 124(5):2452–2464, March 2019. ISSN 2169-897X, 2169-8996. doi: 10.1029/2018JD028894. URL https://onlinelibrary.wiley.com/doi/abs/10.1029/2018JD028894.

Patrick Lehodey, Arnaud Bertrand, Alistair J. Hobday, Hidetada Kiyofuji, Sam McClatchie, Christophe E. Menkès, Graham Pilling, Jeffrey Polovina, and Desiree Tommasi. ENSO Impact on Marine Fisheries and Ecosystems. In *El Niño Southern Oscillation in a Changing Climate*, pages 429–451. American Geophysical Union (AGU), 2020. ISBN 978-1-119-54816-4. doi: 10.1002/9781119548164.ch19. URL https://agupubs.onlinelibrary.wiley.com/doi/abs/10.1002/9781119548164.ch19.

Aaron Levine, Fei Fei Jin, and Michael J. McPhaden. Extreme Noise–Extreme El Niño: How State-Dependent Noise Forcing Creates El Niño–La Niña Asymmetry. *Journal of Climate*, 29(15):5483–5499, August 2016. ISSN 0894-8755, 1520-0442. doi: 10.1175/JCLI-D-16-0091.1. URL https://journals.ametsoc.org/view/journals/clim/29/15/jcli-d-16-0091.1.xml.

Gen Li and Shang-Ping Xie. Tropical Biases in CMIP5 Multimodel Ensemble: The Excessive Equatorial Pacific Cold Tongue and Double ITCZ Problems*. *J. Climate*, 27(4):1765–1780, February 2014. ISSN 0894-8755, 1520-0442. doi: 10.1175/JCLI-D-13-00337.1. URL http://journals.ametsoc.org/doi/abs/10.1175/JCLI-D-13-00337.1.

Jia-Lin Lin. The Double-ITCZ Problem in IPCC AR4 Coupled GCMs:

Ocean–Atmosphere Feedback Analysis. *Journal of Climate*, 20(18):4497–4525, September 2007. ISSN 0894-8755, 1520-0442. doi: 10.1175/JCLI4272.1. URL https://journals.ametsoc.org/view/journals/clim/20/18/jcli4272.1.xml.

Shang-Min Long, Shang-Ping Xie, Xiao-Tong Zheng, and Qinyu Liu. Fast and Slow Responses to Global Warming: Sea Surface Temperature and Precipitation Patterns. *Journal of Climate*, 27(1):285–299, January 2014. ISSN 0894-8755, 1520-0442. doi: 10.1175/JCLI-D-13-00297.1. URL https://journals.ametsoc.org/view/journals/clim/27/1/jcli-d-13-00297.1.xml. Publisher: American Meteorological Society Section: Journal of Climate.

Roland A Madden and Paul R Julian. Detection of a 40–50 day oscillation in the zonal wind in the tropical Pacific. *Journal of Atmospheric Sciences*, 28(5):702–708, 1971.

Elizabeth A. Maroon, Dargan M. W. Frierson, and David S. Battisti. The Tropical Precipitation Response to Andes Topography and Ocean Heat Fluxes in an Aquaplanet Model. *J. Climate*, 28(1):381–398, January 2015. ISSN 0894-8755, 1520-0442. doi: 10.1175/JCLI-D-14-00188.1. URL http://journals.ametsoc.org/doi/10.1175/JCLI-D-14-00188.1.

J. Marshall, A. Donohoe, D. Ferreira, and D. McGee. The ocean's role in setting the mean position of the Inter-Tropical Convergence Zone. *Clim Dyn*, 42(7-8):1967–1979, April 2014. ISSN 0930-7575, 1432-0894. doi: 10.1007/s00382-013-1767-z. URL http://link.springer.com/10.1007/s00382-013-1767-z.

Valérie Masson-Delmotte, Panmao Zhai, Anna Pirani, Sarah L. Connors, Clotilde Péan, Sophie Berger, Nada Caud, Yang Chen, Leah Goldfarb, Melissa I. Gomis, Mengtian Huang, Katherine Leitzell, Elisabeth Lonnoy, J. B. Robin Matthews,

Thomas K. Maycock, Tim Waterfield, Özge Yelekçi, Rong Yu, and Botao Zhou, editors. *Climate Change 2021: The Physical Science Basis. Contribution of Working Group I to the Sixth Assessment Report of the Intergovernmental Panel on Climate Change*. Cambridge University Press, Cambridge, United Kingdom and New York, NY, USA, 2021. doi: 10.1017/9781009157896.

M. J. McPhaden, T. Lee, and D. McClurg. El Niño and its relationship to changing background conditions in the tropical Pacific Ocean. *Geophysical Research Letters*, 38(15), 2011. ISSN 1944-8007. doi: 10.1029/2011GL048275. URL https://agupubs.onlinelibrary.wiley.com/doi/abs/10.1029/2011GL048275.

Michael J. McPhaden. Mixed Layer Temperature Balance on Intraseasonal Timescales in the Equatorial Pacific Ocean. *Journal of Climate*, 15(18):2632–2647, September 2002. ISSN 0894-8755, 1520-0442. doi: 10.1175/1520-0442(2002)015⟨2632:MLTBOI⟩2.0.CO;2. URL https://journals.ametsoc.org/view/journals/clim/15/18/1520-0442_2002_015_2632_mltboi_2.0.co_2.xml. Publisher: American Meteorological Society Section: Journal of Climate.

Michael J. McPhaden, Tong Lee, Severine Fournier, and Magdalena A. Balmaseda. ENSO Observations. In *El Niño Southern Oscillation in a Changing Climate*, pages 39–63. American Geophysical Union (AGU), 2020. ISBN 978-1-119-54816-4. doi: 10.1002/9781119548164.ch3. URL https://agupubs.onlinelibrary.wiley.com/doi/abs/10.1002/9781119548164.ch3.

C.R. Mechoso, A.W. Robertson, N. Barth, M.K. Davey, P. Delecluse, P.R. Gent, S. Ineson, B. Kirtman, M. Latif, H. Le Treut, T. Nagai, J.D. Neelin, S.G.H. Philander, J. Polcher, P.S. Schopf, T. Stockdale, M.J. Suarez, L. Terray, O. Thual, and J.J. Tribbia. The Seasonal Cycle over the Tropical Pacific in Coupled Ocean–Atmosphere General Circulation Models. *Monthly Weather Review*, 123

(9):2825–2838, 1995. doi: 10.1175/1520-0493(1995)123⟨2825:TSCOTT⟩2.0.CO;2. URL https://doi.org/10.1175/1520-0493(1995)123<2825:TSCOTT>2.0.CO;2.

Eduardo Gomez Molina and Adrienne V. Little. Geoecology of the Andes: The Natural Science Basis for Research Planning. *Mountain Research and Development*, 1(2):115–144, 1981. ISSN 0276-4741. doi: 10.2307/3673119. URL https://www.jstor.org/stable/3673119. Publisher: International Mountain Society.

Tessa L. Montini, Charles Jones, and Leila M. V. Carvalho. The South American Low-Level Jet: A New Climatology, Variability, and Changes. *Journal of Geophysical Research: Atmospheres*, 124(3):1200–1218, 2019. ISSN 2169-8996. doi: 10.1029/2018JD029634. URL https://onlinelibrary.wiley.com/doi/abs/10.1029/2018JD029634. _eprint: https://onlinelibrary.wiley.com/doi/pdf/10.1029/2018JD029634.

Zachary Naiman, Paul J. Goodman, John P. Krasting, Sergey L. Malyshev, Joellen L. Russell, Ronald J. Stouffer, and Andrew T. Wittenberg. Impact of Mountains on Tropical Circulation in Two Earth System Models. *Journal of Climate*, 30(11):4149–4163, June 2017. ISSN 0894-8755, 1520-0442. doi: 10.1175/JCLI-D-16-0512.1. URL https://journals.ametsoc.org/view/journals/clim/30/11/jcli-d-16-0512.1.xml.

Richard B Neale, Jadwiga H Richter, and Markus Jochum. The impact of convection on ENSO: From a delayed oscillator to a series of events. *Journal of climate*, 21 (22):5904–5924, 2008. doi: 10.1175/2008JCLI2244.1.

Richard B. Neale, Jadwiga Richter, Sungsu Park, Peter H. Lauritzen, Stephen J. Vavrus, Philip J. Rasch, and Minghua Zhang. The Mean Climate of the Community Atmosphere Model (CAM4) in Forced SST and Fully Coupled Experiments. *J. Climate*, 26(14):5150–5168, July 2013. ISSN 0894-8755, 1520-0442. doi:

10.1175/JCLI-D-12-00236.1. URL http://journals.ametsoc.org/doi/abs/10.1175/JCLI-D-12-00236.1.

J. D. Neelin. *Climate change and climate modeling*. Cambridge University Press, Cambridge, UK, 2011. Backup Publisher: Cambridge University Press.

N. Nicholls. The El Niño / Southern Oscillation and Australian Vegetation. *Vegetatio*, 91(1/2):23–36, 1991. ISSN 0042-3106. URL https://www.jstor.org/stable/20038710.

Paul A. O'Gorman and Tapio Schneider. The physical basis for increases in precipitation extremes in simulations of 21st-century climate change. *Proceedings of the National Academy of Sciences*, 106(35):14773–14777, September 2009. doi: 10.1073/pnas.0907610106. URL https://www.pnas.org/doi/10.1073/pnas.0907610106. Publisher: Proceedings of the National Academy of Sciences.

Boutheina Oueslati and Gilles Bellon. The double ITCZ bias in CMIP5 models: interaction between SST, large-scale circulation and precipitation. *Clim Dyn*, 44 (3):585–607, February 2015. ISSN 1432-0894. doi: 10.1007/s00382-015-2468-6. URL https://doi.org/10.1007/s00382-015-2468-6.

Hamid A. Pahlavan, John M. Wallace, Qiang Fu, and George N. Kiladis. Revisiting the Quasi-Biennial Oscillation as Seen in ERA5. Part II: Evaluation of Waves and Wave Forcing. *Journal of the Atmospheric Sciences*, 78(3):693–707, March 2021. ISSN 0022-4928, 1520-0469. doi: 10.1175/JAS-D-20-0249.1. URL https://journals.ametsoc.org/view/journals/atsc/78/3/JAS-D-20-0249.1.xml.

Hyo-Seok Park, John C. H. Chiang, and Simona Bordoni. The Mechanical Impact of the Tibetan Plateau on the Seasonal Evolution of the South Asian Monsoon. *Journal of Climate*, 25(7):2394–2407, April 2012. ISSN 0894-8755, 1520-0442. doi: 10.1175/JCLI-D-11-00281.1. URL https://journals.ametsoc.org/view/

journals/clim/25/7/jcli-d-11-00281.1.xml. Publisher: American Meteorological Society Section: Journal of Climate.

S. G. H. Philander, D. Gu, G. Lambert, T. Li, D. Halpern, N-C. Lau, and R. C. Pacanowski. Why the ITCZ Is Mostly North of the Equator. *Journal of Climate*, 9 (12):2958–2972, 1996. doi: 10.1175/1520-0442(1996)009⟨2958:WTIIMN⟩2.0.CO;2. URL https://doi.org/10.1175/1520-0442(1996)009<2958:WTIIMN>2.0.CO;2.

Yann Y. Planton, Eric Guilyardi, Andrew T. Wittenberg, Jiwoo Lee, Peter J. Gleckler, Tobias Bayr, Shayne McGregor, Michael J. McPhaden, Scott Power, Romain Roehrig, Jérôme Vialard, and Aurore Voldoire. Evaluating Climate Models with the CLIVAR 2020 ENSO Metrics Package. *Bulletin of the American Meteorological Society*, 102(2):E193–E217, February 2021. ISSN 0003-0007, 1520-0477. doi: 10.1175/BAMS-D-19-0337.1. URL https://journals.ametsoc.org/view/journals/bams/102/2/BAMS-D-19-0337.1.xml.

K. M. M. Prabhu. *Window Functions and Their Applications in Signal Processing*. Taylor & Francis, 2014. ISBN 978-1-4665-1584-0. doi: 10.1201/9781315216386. URL https://library.oapen.org/handle/20.500.12657/41686.

B. Praveen Kumar, J. Vialard, M. Lengaigne, V. S. N. Murty, and M. J. McPhaden. TropFlux: air-sea fluxes for the global tropical oceans—description and evaluation. *Clim Dyn*, 38(7):1521–1543, April 2012. ISSN 1432-0894. doi: 10.1007/s00382-011-1115-0. URL https://doi.org/10.1007/s00382-011-1115-0.

B. Praveen Kumar, J. Vialard, M. Lengaigne, V. S. N. Murty, M. J. McPhaden, M. F. Cronin, F. Pinsard, and K. Gopala Reddy. TropFlux wind stresses over the tropical oceans: evaluation and comparison with other products. *Clim Dyn*, 40(7): 2049–2071, April 2013. ISSN 1432-0894. doi: 10.1007/s00382-012-1455-4. URL https://doi.org/10.1007/s00382-012-1455-4.

María del Rosario Prieto. ENSO signals in South America: rains and floods in the Paraná River region during colonial times. *Climatic Change*, 83(1):39–54, July 2007. ISSN 1573-1480. doi: 10.1007/s10584-006-9188-1. URL https://doi.org/10.1007/s10584-006-9188-1.

Tomas Pucik, Pieter Groenemeijer, and Ivan Tsonevsky. Vertical wind shear and convective storms. (879), January 2021. doi: 10.21957/z0b3t5mrv. URL https://www.ecmwf.int/node/19905. Publisher: ECMWF.

Kristen L. Rasmussen, Manuel D. Zuluaga, and Robert A. Houze Jr. Severe convection and lightning in subtropical South America. *Geophysical Research Letters*, 41(20):7359–7366, 2014. ISSN 1944-8007. doi: 10.1002/2014GL061767. URL https://onlinelibrary.wiley.com/doi/abs/10.1002/2014GL061767. _eprint: https://onlinelibrary.wiley.com/doi/pdf/10.1002/2014GL061767.

N. A. Rayner, D. E. Parker, E. B. Horton, C. K. Folland, L. V. Alexander, D. P. Rowell, E. C. Kent, and A. Kaplan. Global analyses of sea surface temperature, sea ice, and night marine air temperature since the late nineteenth century. *Journal of Geophysical Research: Atmospheres*, 108(D14), 2003. ISSN 2156-2202. doi: https://doi.org/10.1029/2002JD002670. URL https://agupubs.onlinelibrary.wiley.com/doi/abs/10.1029/2002JD002670.

P. Renteln. *Manifolds, Tensors, and Forms: An Introduction for Mathematicians and Physicists*. Cambridge University Press, 2013. ISBN 978-1-107-65969-8. URL https://books.google.com/books?id=uJWGAgAAQBAJ.

Juan A. Rivera and Gabriel Arnould. Evaluation of the ability of CMIP6 models to simulate precipitation over Southwestern South America: Climatic features and long-term trends (1901–2014). *Atmospheric Research*, 241:104953, Septem-

ber 2020. ISSN 0169-8095. doi: 10.1016/j.atmosres.2020.104953. URL https://www.sciencedirect.com/science/article/pii/S0169809519317259.

Keith B. Rodgers, Petra Friederichs, and Mojib Latif. Tropical Pacific Decadal Variability and Its Relation to Decadal Modulations of ENSO. *Journal of Climate*, 17(19):3761–3774, October 2004. ISSN 0894-8755, 1520-0442. doi: 10.1175/1520-0442(2004)017⟨3761:TPDVAI⟩2.0.CO;2. URL https://journals.ametsoc.org/view/journals/clim/17/19/1520-0442_2004_017_3761_tpdvai_2.0.co_2.xml.

M. J. Rodwell and B. J. Hoskins. Subtropical Anticyclones and Summer Monsoons. *Journal of Climate*, 14(15):3192–3211, August 2001. ISSN 0894-8755, 1520-0442. doi: 10.1175/1520-0442(2001)014⟨3192:SAASM⟩2.0.CO;2. URL https://journals.ametsoc.org/view/journals/clim/14/15/1520-0442_2001_014_3192_saasm_2.0.co_2.xml. Publisher: American Meteorological Society Section: Journal of Climate.

Tapio Schneider, Colleen M. Kaul, and Kyle G. Pressel. Possible climate transitions from breakup of stratocumulus decks under greenhouse warming. *Nat. Geosci.*, 12(3):163–167, March 2019. ISSN 1752-0894, 1752-0908. doi: 10.1038/s41561-019-0310-1. URL http://www.nature.com/articles/s41561-019-0310-1.

Russ S. Schumacher. Sensitivity of Precipitation Accumulation in Elevated Convective Systems to Small Changes in Low-Level Moisture. *Journal of the Atmospheric Sciences*, 72(6):2507–2524, June 2015. ISSN 0022-4928, 1520-0469. doi: 10.1175/JAS-D-14-0389.1. URL https://journals.ametsoc.org/view/journals/atsc/72/6/jas-d-14-0389.1.xml. Publisher: American Meteorological Society Section: Journal of the Atmospheric Sciences.

R. Justin Small, Julio Bacmeister, David Bailey, Allison Baker, Stuart Bishop, Frank Bryan, Julie Caron, John Dennis, Peter Gent, Hsiao-ming Hsu, Markus Jochum, David Lawrence, Ernesto Muñoz, Pedro diNezio, Tim Scheitlin, Robert Tomas, Joseph Tribbia, Yu-heng Tseng, and Mariana Vertenstein. A new synoptic scale resolving global climate simulation using the Community Earth System Model. *Journal of Advances in Modeling Earth Systems*, 6(4):1065–1094, 2014. doi: 10.1002/2014MS000363. URL `https://agupubs.onlinelibrary.wiley.com/doi/abs/10.1002/2014MS000363`. _eprint: https://agupubs.onlinelibrary.wiley.com/doi/pdf/10.1002/2014MS000363.

Ken Takahashi and David S. Battisti. Processes Controlling the Mean Tropical Pacific Precipitation Pattern. Part I: The Andes and the Eastern Pacific ITCZ. *Journal of Climate*, 20(14):3434–3451, July 2007a. ISSN 1520-0442. doi: 10.1175/jcli4198.1. URL `http://dx.doi.org/10.1175/JCLI4198.1`. Publisher: American Meteorological Society.

Ken Takahashi and David S. Battisti. Processes Controlling the Mean Tropical Pacific Precipitation Pattern. Part II: The SPCZ and the Southeast Pacific Dry Zone. *Journal of Climate*, 20(23):5696–5706, December 2007b. ISSN 0894-8755, 1520-0442. doi: 10.1175/2007JCLI1656.1. URL `https://journals.ametsoc.org/view/journals/clim/20/23/2007jcli1656.1.xml`.

Mateusz Taszarek, John T. Allen, Mattia Marchio, and Harold E. Brooks. Global climatology and trends in convective environments from ERA5 and rawinsonde data. *npj Clim Atmos Sci*, 4(1):1–11, June 2021. ISSN 2397-3722. doi: 10.1038/s41612-021-00190-x. URL `https://www.nature.com/articles/s41612-021-00190-x`. Number: 1 Publisher: Nature Publishing Group.

Karl E. Taylor, Ronald J. Stouffer, and Gerald A. Meehl. An Overview of CMIP5 and the Experiment Design. *Bull. Amer. Meteor. Soc.*, 93(4):485–498, April 2012.

ISSN 0003-0007, 1520-0477. doi: 10.1175/BAMS-D-11-00094.1. URL http://journals.ametsoc.org/doi/abs/10.1175/BAMS-D-11-00094.1.

Paul C. F. van der Vaart, Henk A. Dijkstra, and Fei Fei Jin. The Pacific Cold Tongue and the ENSO Mode: A Unified Theory within the Zebiak–Cane Model. *Journal of the Atmospheric Sciences*, 57(7):967–988, April 2000. ISSN 0022-4928, 1520-0469. doi: 10.1175/1520-0469(2000)057⟨0967:TPCTAT⟩2.0.CO;2. URL https://journals.ametsoc.org/view/journals/atsc/57/7/1520-0469_2000_057_0967_tpctat_2.0.co_2.xml. Publisher: American Meteorological Society Section: Journal of the Atmospheric Sciences.

Geoffrey K. Vallis. *Essentials of Atmospheric and Oceanic Dynamics*. Cambridge University Press, 2019. doi: 10.1017/9781107588431.

Rudi J. van der Ent, Hubert H. G. Savenije, Bettina Schaefli, and Susan C. Steele-Dunne. Origin and fate of atmospheric moisture over continents. *Water Resources Research*, 46(9), 2010. ISSN 1944-7973. doi: 10.1029/2010WR009127. URL https://onlinelibrary.wiley.com/doi/abs/10.1029/2010WR009127. _eprint: https://onlinelibrary.wiley.com/doi/pdf/10.1029/2010WR009127.

Sarah Verbickas. Westerly wind bursts in the tropical Pacific. *Weather*, 53(9): 282–284, 1998. ISSN 1477-8696. doi: 10.1002/j.1477-8696.1998.tb06401.x. URL https://onlinelibrary.wiley.com/doi/abs/10.1002/j.1477-8696.1998.tb06401.x. _eprint: https://onlinelibrary.wiley.com/doi/pdf/10.1002/j.1477-8696.1998.tb06401.x.

Chunzai Wang, Liping Zhang, Sang-Ki Lee, Lixin Wu, and Carlos R. Mechoso. A global perspective on CMIP5 climate model biases. *Nature Clim Change*, 4(3):201–205, March 2014. ISSN 1758-678X, 1758-6798. doi: 10.1038/nclimate2118. URL http://www.nature.com/articles/nclimate2118.

Hui Wang and Rong Fu. Influence of Cross-Andes Flow on the South American Low-Level Jet. *Journal of Climate*, 17(6):1247–1262, March 2004. ISSN 0894-8755, 1520-0442. doi: 10.1175/1520-0442(2004)017⟨1247:IOCFOT⟩2.0.CO;2. URL https://journals.ametsoc.org/view/journals/clim/17/6/1520-0442_2004_017_1247_iocfot_2.0.co_2.xml. Publisher: American Meteorological Society Section: Journal of Climate.

Yuqing Wang, Shang-Ping Xie, Haiming Xu, and Bin Wang. Regional Model Simulations of Marine Boundary Layer Clouds over the Southeast Pacific off South America. Part I: Control Experiment. *Monthly Weather Review*, 132(1):274–296, 2004. doi: 10.1175/1520-0493(2004)132⟨0274:RMSOMB⟩2.0.CO;2. URL https://doi.org/10.1175/1520-0493(2004)132<0274:RMSOMB>2.0.CO;2.

C. Wengel, M. Latif, W. Park, J. Harlaß, and T. Bayr. Seasonal ENSO phase locking in the Kiel Climate Model: The importance of the equatorial cold sea surface temperature bias. *Clim Dyn*, 50(3):901–919, February 2018. ISSN 1432-0894. doi: 10.1007/s00382-017-3648-3. URL https://doi.org/10.1007/s00382-017-3648-3.

Matthew Wheeler and George N. Kiladis. Convectively Coupled Equatorial Waves: Analysis of Clouds and Temperature in the Wavenumber–Frequency Domain. *Journal of the Atmospheric Sciences*, 56(3):374–399, February 1999. ISSN 0022-4928, 1520-0469. doi: 10.1175/1520-0469(1999)056⟨0374:CCEWAO⟩2.0.CO;2. URL https://journals.ametsoc.org/view/journals/atsc/56/3/1520-0469_1999_056_0374_ccewao_2.0.co_2.xml.

K. D. Williams, A. Bodas-Salcedo, M. Déqué, S. Fermepin, B. Medeiros, M. Watanabe, C. Jakob, S. A. Klein, C. A. Senior, and D. L. Williamson. The Transpose-AMIP II Experiment and Its Application to the Understanding of Southern Ocean Cloud Biases in Climate Models. *J. Climate*, 26(10):3258–3274, May 2013. ISSN

0894-8755, 1520-0442. doi: 10.1175/JCLI-D-12-00429.1. URL http://journals.ametsoc.org/doi/abs/10.1175/JCLI-D-12-00429.1.

Robert C. J. Wills and Tapio Schneider. Mechanisms Setting the Strength of Orographic Rossby Waves across a Wide Range of Climates in a Moist Idealized GCM. *Journal of Climate*, 31(18):7679–7700, September 2018. ISSN 0894-8755, 1520-0442. doi: 10.1175/JCLI-D-17-0700.1. URL https://journals.ametsoc.org/view/journals/clim/31/18/jcli-d-17-0700.1.xml. Publisher: American Meteorological Society Section: Journal of Climate.

Andrew T. Wittenberg, Gabriel A. Vecchi, Thomas L. Delworth, Anthony Rosati, Whit G. Anderson, William F. Cooke, Seth Underwood, Fanrong Zeng, Stephen M. Griffies, and Sulagna Ray. Improved Simulations of Tropical Pacific Annual-Mean Climate in the GFDL FLOR and HiFLOR Coupled GCMs. *Journal of Advances in Modeling Earth Systems*, 10(12):3176–3220, 2018. ISSN 1942-2466. doi: 10.1029/2018MS001372. URL https://agupubs.onlinelibrary.wiley.com/doi/abs/10.1029/2018MS001372.

Alexandra Witze. Argentina's mega-storms attract army of meteorologists. *Nature*, 563(7730):166–166, November 2018. doi: 10.1038/d41586-018-07268-2. URL https://www.nature.com/articles/d41586-018-07268-2. Bandiera_abtest: a Cg_type: News Number: 7730 Publisher: Nature Publishing Group Subject_term: Atmospheric science, Climate sciences.

Robert Wood. Stratocumulus Clouds. *Monthly Weather Review*, 140(8):2373–2423, August 2012. ISSN 1520-0493, 0027-0644. doi: 10.1175/MWR-D-11-00121.1. URL https://journals.ametsoc.org/view/journals/mwre/140/8/mwr-d-11-00121.1.xml. Publisher: American Meteorological Society Section: Monthly Weather Review.

M. Wu and J.-E. Lee. Thresholds for Atmospheric Convection in Amazonian Rainforests. *Geophysical Research Letters*, 46(16):10024–10033, 2019. ISSN 1944-8007. doi: 10.1029/2019GL082909. URL https://onlinelibrary.wiley.com/doi/abs/10.1029/2019GL082909. _eprint: https://onlinelibrary.wiley.com/doi/pdf/10.1029/2019GL082909.

Klaus Wyrtki. El Niño—The Dynamic Response of the Equatorial Pacific Oceanto Atmospheric Forcing. *Journal of Physical Oceanography*, 5(4):572–584, October 1975. ISSN 0022-3670, 1520-0485. doi: 10.1175/1520-0485(1975)005⟨0572:ENTDRO⟩2.0.CO;2. URL https://journals.ametsoc.org/view/journals/phoc/5/4/1520-0485_1975_005_0572_entdro_2_0_co_2.xml. Publisher: American Meteorological Society Section: Journal of Physical Oceanography.

Klaus Wyrtki. Water displacements in the Pacific and the genesis of El Nino cycles. *Journal of Geophysical Research: Oceans*, 90(C4):7129–7132, 1985. ISSN 2156-2202. doi: https://doi.org/10.1029/JC090iC04p07129. URL https://agupubs.onlinelibrary.wiley.com/doi/abs/10.1029/JC090iC04p07129.

Baoqiang Xiang, Ming Zhao, Isaac M. Held, and Jean-Christophe Golaz. Predicting the severity of spurious "double ITCZ" problem in CMIP5 coupled models from AMIP simulations. *Geophys. Res. Lett.*, 44(3):1520–1527, February 2017. ISSN 0094-8276, 1944-8007. doi: 10.1002/2016GL071992. URL https://onlinelibrary.wiley.com/doi/abs/10.1002/2016GL071992.

Pingping Xie, Robert Joyce, Shaorong Wu, S.-H. Yoo, Yelena Yarosh, Fengying Sun, and Robert Lin. NOAA Climate Data Record (CDR) of CPC Morphing Technique (CMORPH) High Resolution Global Precipitation Estimates, Version 1, 2020. URL https://doi.org/10.5065/0EFN-KZ90. Place: Boulder CO.

Shang-Ping Xie. Ocean–Atmosphere Interaction in the Making of the Walker Circulation and Equatorial Cold Tongue. *JOURNAL OF CLIMATE*, 11:13, 1998.

Shang-Ping. Xie and S. George H. Philander. A coupled ocean-atmosphere model of relevance to the ITCZ in the eastern Pacific. *Tellus A*, 46(4):340–350, 1994a. ISSN 1600-0870. doi: 10.1034/j.1600-0870.1994.t01-1-00001.x. URL https://onlinelibrary.wiley.com/doi/abs/10.1034/j.1600-0870.1994.t01-1-00001.x. _eprint: https://onlinelibrary.wiley.com/doi/pdf/10.1034/j.1600-0870.1994.t01-1-00001.x.

Shang-Ping Xie, Toru Miyama, Yuqing Wang, Haiming Xu, Simon P. de Szoeke, R. Justin O. Small, Kelvin J. Richards, Takashi Mochizuki, and Toshiyuki Awaji. A Regional Ocean–Atmosphere Model for Eastern Pacific Climate: Toward Reducing Tropical Biases*. *J. Climate*, 20(8):1504–1522, April 2007. ISSN 0894-8755, 1520-0442. doi: 10.1175/JCLI4080.1. URL http://journals.ametsoc.org/doi/abs/10.1175/JCLI4080.1.

Shang-Ping. Xie and S.G.H. Philander. A coupled ocean-atmosphere model of relevance to the ITCZ in the eastern Pacific. *Tellus A*, 46(4):340–350, 1994b. ISSN 1600-0870. doi: 10.1034/j.1600-0870.1994.t01-1-00001.x. URL https://doi.org/10.1034/j.1600-0870.1994.t01-1-00001.x.

Haiming Xu, Yuqing Wang, and Shang-Ping Xie. Effects of the Andes on Eastern Pacific Climate: A Regional Atmospheric Model Study. *JOURNAL OF CLIMATE*, 17:14, 2004.

Weixuan Xu and Jung-Eun Lee. The Andes and the Southeast Pacific Cold Tongue Simulation. *Journal of Climate*, 34(1):415–425, January 2021. ISSN 0894-8755, 1520-0442. doi: 10.1175/JCLI-D-19-0901.1. URL https://journals.ametsoc.org/view/journals/clim/34/1/JCLI-D-19-0901.1.xml.

Weixuan Xu, Jung-Eun Lee, Baylor Fox-Kemper, Yann Planton, and Michael J. McPhaden. The Andes Affect ENSO Statistics. *Journal of Climate*, 35 (21):3471–3485, October 2022. ISSN 0894-8755, 1520-0442. doi: 10.1175/JCLI-D-21-0866.1. URL https://journals.ametsoc.org/view/journals/clim/35/21/JCLI-D-21-0866.1.xml. Publisher: American Meteorological Society Section: Journal of Climate.

Sang-Wook Yeh, Wenju Cai, Seung-Ki Min, Michael J. McPhaden, Dietmar Dommenget, Boris Dewitte, Matthew Collins, Karumuri Ashok, Soon-Il An, Bo-Young Yim, and Jong-Seong Kug. ENSO Atmospheric Teleconnections and Their Response to Greenhouse Gas Forcing. *Rev. Geophys.*, 56(1):185–206, March 2018. ISSN 87551209. doi: 10.1002/2017RG000568. URL http://doi.wiley.com/10.1002/2017RG000568.

B. Yu, F. W. Zwiers, G. J. Boer, and M. F. Ting. Structure and variances of equatorial zonal circulation in a multimodel ensemble. *Climate Dynamics*, 39(9-10):2403–2419, May 2012. ISSN 1432-0894. doi: 10.1007/s00382-012-1372-6. URL http://dx.doi.org/10.1007/s00382-012-1372-6. Publisher: Springer Science and Business Media LLC.

Tao Zhang and De-Zheng Sun. ENSO Asymmetry in CMIP5 Models. *Journal of Climate*, 27(11):4070–4093, June 2014. ISSN 0894-8755, 1520-0442. doi: 10.1175/JCLI-D-13-00454.1. URL https://journals.ametsoc.org/view/journals/clim/27/11/jcli-d-13-00454.1.xml.

Bowen Zhao and Alexey Fedorov. The Effects of Background Zonal and Meridional Winds on ENSO in a Coupled GCM. *Journal of Climate*, 33(6):2075–2091, February 2020. ISSN 0894-8755, 1520-0442. doi: 10.1175/JCLI-D-18-0822.1. URL https://journals.ametsoc.org/view/journals/clim/33/6/jcli-d-18-0822.1.xml.

Zaichun Zhu, Shilong Piao, Ranga B. Myneni, Mengtian Huang, Zhenzhong Zeng, Josep G. Canadell, Philippe Ciais, Stephen Sitch, Pierre Friedlingstein, Almut Arneth, Chunxiang Cao, Lei Cheng, Etsushi Kato, Charles Koven, Yue Li, Xu Lian, Yongwen Liu, Ronggao Liu, Jiafu Mao, Yaozhong Pan, Shushi Peng, Josep Peñuelas, Benjamin Poulter, Thomas A. M. Pugh, Benjamin D. Stocker, Nicolas Viovy, Xuhui Wang, Yingping Wang, Zhiqiang Xiao, Hui Yang, Sönke Zaehle, and Ning Zeng. Greening of the Earth and its drivers. *Nature Clim Change*, 6 (8):791–795, August 2016. ISSN 1758-6798. doi: 10.1038/nclimate3004. URL `https://www.nature.com/articles/nclimate3004`. Number: 8 Publisher: Nature Publishing Group.

Ziyan Zhu, Christopher Li, and J. B. Marston. Topology of rotating stratified fluids with and without background shear flow. Technical Report arXiv:2112.04691, arXiv, December 2021. URL `http://arxiv.org/abs/2112.04691`.

Marcia T. Zilli, Leila M. V. Carvalho, Brant Liebmann, and Maria A. Silva Dias. A comprehensive analysis of trends in extreme precipitation over southeastern coast of Brazil. *International Journal of Climatology*, 37(5):2269–2279, 2017. ISSN 1097-0088. doi: 10.1002/joc.4840. URL `https://onlinelibrary.wiley.com/doi/abs/10.1002/joc.4840`. _eprint: https://onlinelibrary.wiley.com/doi/pdf/10.1002/joc.4840.

E. J. Zipser, Daniel J. Cecil, Chuntao Liu, Stephen W. Nesbitt, and David P. Yorty. WHERE ARE THE MOST INTENSE THUNDERSTORMS ON EARTH? *Bulletin of the American Meteorological Society*, 87(8):1057–1072, August 2006. ISSN 0003-0007, 1520-0477. doi: 10.1175/BAMS-87-8-1057. URL `https://journals.ametsoc.org/view/journals/bams/87/8/bams-87-8-1057.xml`. Publisher: American Meteorological Society Section: Bulletin of the American Meteorological Society.